Institute of Thermal Engineering

TU Graz
Graz University of Technology

Mario Blehrmühlhuber, BSc

CFD Simulation of Hydrodynamics in Fluidized Beds

MASTER´S THESIS

to achieve the university degree of

Diplom-Ingenieur

Master´s degree programme: Mechanical Engineering

submitted to

Graz University of Technology

Supervisor

Univ.-Prof. Dipl.-Ing. Dr.techn. Robert Scharler
Institute of Thermal Engineering

Graz, December 2018

Affidavit

I declare that I have authored this thesis independently, that I have not used other than the declared sources/resources, and that I have explicitly indicated all material which has been quoted either literally or by content from the sources used. The text document uploaded to TUGRAZonline is identical to the present master‘s thesis.

_____	_____
Date	Signature

Kurzfassung

Titel: CFD Simulation der Hydrodynamik in Wirbelschichten
Autor: Mario Blehrmühlhuber

1. Stichwort: Wirbelschicht
2. Stichwort: Mehrphasenströmung
3. Stichwort: Kaltsimulation

Eine sauberere und effizientere Möglichkeit Biomasse zu verwerten, ist die Verbrennung oder Vergasung in Wirbelschichten. Um diesen Prozess zu optimieren, können CFD-Modelle eingesetzt werden. In dieser Arbeit werden Mehrphasenmodelle untersucht, um Erfahrungen und Richtlinien für ein zukünftiges CFD-Modell zu sammeln. Ziel ist es, die individuellen Stärken und Schwächen jedes Modells zu ermitteln. Darüber hinaus sollen Empfehlungen zur Modellierung von Wirbelschichten gegeben werden. Kaltsimulationen wurden durchgeführt, um die Hydrodynamik von Wirbelschichten zu verstehen und die verschiedenen kommerziell verfügbaren Mehrphasenmodelle bewerten zu können.
Die in ANSYS® Fluent verfügbaren Modelle Euler Granular Model und das Dense Discrete Phase Model (DDPM) wurden getestet. DDPM verwendet einen Eulerischen Ansatz und einen Lagrangian Ansatz für die diskrete Phase (Hybrid Modell aus Discrete Phase Model und Euler Granular). Der Fokus lag auf den DDPM Modellen. Wichtige Teilmodelle wurden ebenfalls untersucht. Speziell die in ANSYS® Fluent implementierten Drag-Laws, sowie die Möglichkeiten zur Modellierung von Partikelgrößenverteilung (PSD) wurden betrachtet. Des Weiteren sind die Partikel-Partikel Interaktionsmodelle „Kinetic Theory of Granular Flow“ (KTGF) und die Discrete Elements Methods (DEM) evaluiert worden. Das KTGF approximiert die vorkommenden Partikelkollisionen. Im Gegensatz dazu berechnet das DEM jede einzelne Kollision. Die Kalibrierung und Einstellung der zahlreichen Modellparameter erfolgte durch experimentelle Daten. Für die Bewertung der verschiedenen Modellansätze sind öffentlich zugängliche Daten verwendet worden (bereitgestellt vom National Energy Technology Laboratory – NETL). Gestartet wurde mit der NETL I Challenge, einer kleinen stationären Wirbelschicht mit einheitlicher Partikelgröße. Anschließend wurden die NETL III Challenges untersucht, die industriell relevante Probleme darstellen (hohe Anzahl von Partikeln mit PSD).
Es konnte gezeigt werden, dass das DDPM-DEM Modell am flexibelsten und genauesten ist. Die detaillierte Auflösung der Partikelwechselwirkungen ist jedoch für industrielle Anwendungen zu aufwändig. Das rechnerisch weniger anspruchsvolle DDPM-KTGF Modell ist hingegen sehr empfindlich gegenüber seinen Parametern. Für die Genauigkeit ausschlaggebend sind vor allem der Volumenanteil der granularen Phase, die rechnerische Auflösung der Partikelkollisionen und die gewählten Randbedingungen an den Wänden. Unter der minimalen Fluidisierungsgeschwindigkeit U_{mf} versagten die DDPM-KTGF Modelle, daher sind sie für Festbetten nicht geeignet. Mit sorgfältig gewählten Einstellungen waren die KTGF Modelle jedoch in der Lage, gute Ergebnisse für die gemittelten Partikelgeschwindigkeiten zu liefern (Gasgeschwindigkeiten über U_{mf}). Das zuverlässigste Drag-Law war jenes von Gidaspow (Gasgeschwindigkeiten > U_{mf}). Die Vorhersage der Bettausdehnung und des Druckabfalls mit den Standard Drag-Laws wurde aber in beinahe allen Fällen überschätzt.
Basierend auf den Erkenntnissen dieser Arbeit, wird zukünftig eine alternative Drag-Law getestet. Darauf aufbauend wird ein CFD-Modell für einen gesamten Biomassevergasungsprozess in einer Wirbelschicht erstellt.

Abstract

Title: CFD simulation of hydrodynamics in fluidized beds
Author: Mario Blehrmühlhuber

1st keyword: Fluidized bed
2nd keyword: Multiphase flow
3rd keyword: Cold Flow-simulation

In the search for cleaner biomass conversion routes, one approach is the gasification of solid fuels in fluidized beds. To gain a better insight in the underlying processes, as well as for developing and improving occurring processes inside fluidized beds, CFD is commonly used. In this work, multiphase models for fluidized beds are studied in order to gain experience and to create guidelines for a future comprehensive CFD model for fluidized beds. The primary objective is to determine the individual strengths and weaknesses of each model approach. Furthermore, recommendations for modeling fluidized beds should be given. On that account, cold flow simulations were performed to understand the hydrodynamics of fluidized beds as well as to rate different commercially available multiphase models.
The in ANSYS® Fluent implemented Euler Granular model and the Dense Discrete Phase Model (DDPM) were tested. DDPM is using an Eulerian approach and additionally a Lagrangian approach for the solid phase (hybrid model of Discrete Phase Model and Euler Granular model). This work focused on the DDPM approach. Besides the multiphase models, important sub-models were studied. Variations of the ANSYS® Fluent built-in drag laws as well as of the particle size distribution (PSD) were done. The particle interaction models “Kinetic Theory of Granular Flow” (KTGF) and the Discrete Elements Methods (DEM) were tested. The KTGF model is approximating the particle collisions. The DEM is directly resolving all particle collisions. Due to the variety of model settings, experimental data was used to calibrate and adjust the parameters. Data provided by the National Energy Technology Laboratory (NETL) was used to assess the different model approaches. First, the NETL I challenge (small-scale and steady fluidized bed with a uniform particle size) was calculated. Afterwards, the NETL III challenges, which are representing industrial relevant problems, were calculated (high number of particles with a PSD).
It was shown that the DDPM-DEM model was the best and most flexible approach. However, the detailed resolution of the inter-particle interactions is still too costly for industrial applications. Whereas the numerically less demanding DDPM-KTGF is sensitive to its parameters. Crucial for the calculations are, in particular, the particle volume fraction, the resolution of the collisions and the boundary conditions at the walls. DDPM-KTGF models in combination with standard drag laws were failing below the minimum fluidization velocity U_{mf}. Therefore, DDPM KTGF cannot be used for packed beds. Nevertheless, DDPM-KTGF models with carefully selected settings were yielding competitive results for the averaged particle velocities (gas velocity higher than U_{mf}). Best drag law was Gidaspow drag law (for velocities significantly higher than U_{mf}). However, especially the bed expansion and the pressure drop were over-predicted for nearly every case.
Based on the findings of this work, an alternative drag model will be tested in the future. Furthermore, a comprehensive CFD model for biomass gasification processes in fluidized beds will be prepared.

Preface

This work evolved between February and December 2018 at the Institute of Thermal Engineering of the University of Technology Graz and was funded by the European Horizon 2020 BRISK2 (Biofuel Research Infrastructure for Sharing Knowledge) project. During my work on the Institute of Thermal Engineering, I was able to gain detailed knowledge about the modeling approaches of fluidized beds reactors as well as in handling commercial CFD-codes.

I would thank the entire working group of “Sustainable, clean and bioenergy systems” of the Institute of Thermal Engineering, especially Univ.-Prof. Dipl.-Ing. Dr.techn. Robert Scharler for the allocation and final assessment of this work and the providing of the required resources. I would also like to thank my supervisor, Dipl.-Ing. Lukas von Berg for the correction of this thesis and the helpful instructions.

Many thanks to my friends, my study colleagues, and to my colleagues at the Department of Thermal Engineering who were always there when a question arose, or there was a need for coffee.

Greatest thanks to my family who were patiently supporting me in my study and just made this work possible with their financial support and the motivational words.

Thank you all.

Mario Blehrmühlhuber

Graz, 12/19/2018

Table of Contents

1 Introduction

1.1 Motivation

In the search for more efficient biomass conversion technologies with higher valuable products, one approach is the gasification of solid fuels. The obtained product gas can be used for combustion in gas engines or turbines, for fuel cells or as synthesis gas for the production of fuels and chemicals. The use of gasified biomass allows a better control of the processes as well as a better emission behavior. For this biomass conversion route, fluidized beds can be used [1]. To get a better insight, as well as for developing and improving occurring processes inside fluidized beds, CFD modeling is a commonly used tool in the bioenergy sector. CFD can observe all bed parts at every operation point for any parameter. Weaknesses or improvement potentials can be identified more easily. Improvements can lead to better efficiency and lower emissions. Therefore, a comprehensive CFD model of the biomass conversion in fluidized beds is desired by industry and research institutes. The Institute of Thermal Engineering at the University of Technology Graz is currently developing a detailed model for fluidized bed reactors, which is a part of the European Horizon 2020 BRISK2 (Biofuel Research Infrastructure for Sharing Knowledge) project. In this thesis, the hydrodynamics of fluidized beds are studied in order to gain experience and to create guidelines for the future development of the comprehensive CFD-model.

1.2 Objectives

The in ANSYS® Fluent built-in multiphase models and sub-models (drag laws, particle interactions and particle size distribution models) were tested. The work focused on the DDPM model, since it is in advantage when considering different particle types and size classes (compared to Euler Granular model), including chemical reactions. The particle interaction approaches KTGF and DEM were compared for DDPM. Furthermore, Euler Granular models were set up to compare KTGF for different multiphase models. Due to a large number of model parameters, experimental data (provided by the National Energy Technology Laboratory) was used to validate and adapt these parameters. After literature research, the following research questions were defined, investigated and discussed within this work:

- **Q1** Which multiphase models available in the commercial CFD code ANSYS® Fluent are suitable to simulate biomass fluidized beds?
- **Q2** How important are particle interactions and how can these interactions be modeled?
- **Q3** How can the influence of the particle size distributions (PSD) be included in the models?
- **Q4** Are the drag laws available in ANSYS® Fluent able to predict the fluidized bed behavior?
- **Q5** For which bed regimes, bed types and bed sizes are these models suitable?

Chapter 2 is introducing the fundamentals of fluidized beds. In chapter 3, multiphase models are discussed (**Q1**, **Q2**, **Q4**). Chapter 4 deals with the modeling of a lab-scaled fluidized bed (**Q1**, **Q2**, **Q4**). In chapter 5, the handling of industrial-scale bubbling and circulating fluidized beds are investigated (**Q2**-**Q5**). Finally, in chapter 6, the results will be summarized, and the research questions will be discussed.

2 Fundamentals of fluidized beds

2.1 Fluidized bed regimes

A gas stream of low velocity through an agglomeration of a granular phase (the bed) will slowly flow through the void spaces between the particles [1]. The solid phase is unmoved (fixed bed), as shown in Figure 2-1 (a). With increasing gas velocity, the granular material starts to move. Since the movement prevents densest particle packing, the bed is expanding. The pressure drop through any section of the bed is proportional increasing with the gas velocity. When the gas velocity is further increased, a point will be reached in which the particles are losing the direct contact with each other. At this so-called minimum fluidization velocity U_{mf}, the frictional force between gas and particles is equal to the bed weight [1]. The granular matter is transformed into a fluid-like state through suspension in the gas phase. In this state, the bed is called a fluidized bed (FB). An example for a fluidized bed can be seen in Figure 2-1 (b). A characteristic of fluidized beds is that the pressure drop through any section of the bed is about the same as the weight of the gas and the solid phase in this section. At a still higher gas velocity, the bed is continuously expanding. For certain gas-particle combinations (see chapter 2.4) the suspension can form a bubbling behavior. The flow is determined by bubble forming, bubble coalescence and bubble break-ups. A typical example for a bubbling fluidized bed is presented in Figure 2-1 (c). A further increase of the gas velocity (exceeding of the particle terminal velocity U_t for smallest particles) is leading to turbulent fluidization – shown in Figure 2-1 (d). Beginning with the turbulent fluidization no distinctive upper bed surface is recognizable anymore. Finally, when the gas velocity is higher than U_t (for all particles), the bed is operating in the pneumatic transport regime (also called pneumatic conveying regime) – see Figure 2-1 (e) [1]. Without recirculation or newly fed particles, all bed material will be entrained over time. Circulating fluidized beds (CFB) are operating in the pneumatic transport region – also see chapter 2.6 [1–3].

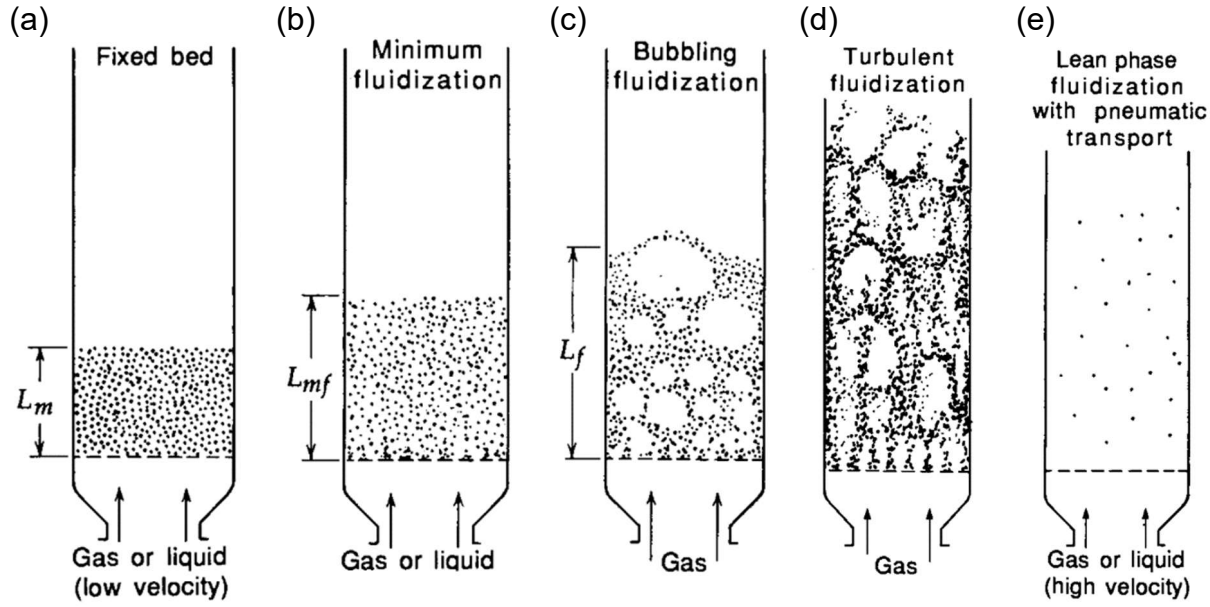

Figure 2-1: Stages of fluidization [1].

2.2 Advantages and disadvantages of fluidized beds

The fluidized suspension allows continuous and relatively easy controllable processes [1]. Further advantages of fluidized beds are the high gas-particle contact surface and the excellent mixing. For chemical processes, the equally distributed and the relatively constant temperature, as well as the high particle surface, are advantageous. The isothermal behavior originates in the excellent mixing and the amount of thermal energy stored in the bed material. The temperature in a fluidized bed is rather constant and resists rapid temperature changes. That and the advantage of the high heat and mass transfer rates made fluidized beds to an often used process in the thermal engineering sector [1,2,4].
Although fluidized beds have excellent mixing behavior, the residence time is not necessarily the same for all particles [1]. That is particularly true for CFB's, where particles can stay in the bed region for a while or may directly be entrained to the recirculation facilities. For chemical processes at high-temperature, undesired sinter effects between the particles can occur. The change of particle size and shape can significantly influence the bed behavior. The handling of fine particles is difficult since this particle class is often resulting in an erratic plug flow (chapter 2.4). Furthermore, crumble solids can be pulverized. The smallest particles are then entrained with the gas, which may require filtering of the product gas. A problem, which is shared by all fluidized beds, is the abrasion due to particle friction and particle collisions. Erosion of pipes and the bed walls shortens the operating lifetime of the plant. Another disadvantage is the power consumption because of the provision of the continuous gas stream. The gas stream has to overcome the pressure drop in fluidized beds. For deep beds, power consumption can be as high that the FB cannot be operated economically [1].
Since the advantages outweigh the disadvantages, fluidized beds were developed for various industrial processes. The first field of application was the coal gasification, which was used to obtain syngas for chemical processes. Nowadays fluidized beds are used for a broad range of applications. They are used for biomass gasification and combustion (e.g., inside dual fluidized beds, see Kraft [3] and chapter 2.6) as well as for waste incineration. In chemical process engineering, FB's are mainly used for fluid catalytic cracking (FCC) and synthesis reactions (e.g., Fischer-Tropsch synthesis and Sohio process). In the metallurgic and plastic industry, FB's are used for drying, coating, and solidification of granular materials [1,3].

2.3 Pressure drop diagram

The pressure drop over the bed Δp_{bed} is used to distinguish between the fixed bed, the fluidized bed, and the pneumatic transport regime [1]. The pressure drop is measured for increasing superficial gas velocity U_0. The pressure drop versus superficial gas velocity diagram is also called fluidization curve. The fluidization curve presented in Figure 2-2 is an idealized one. Because of the unsteady nature of fluidized beds, the values are strongly fluctuating over time. However, if the values are averaged over a sufficient long period, statistically constant values are obtained (also compare with chapter 4.4.1) [1,2].

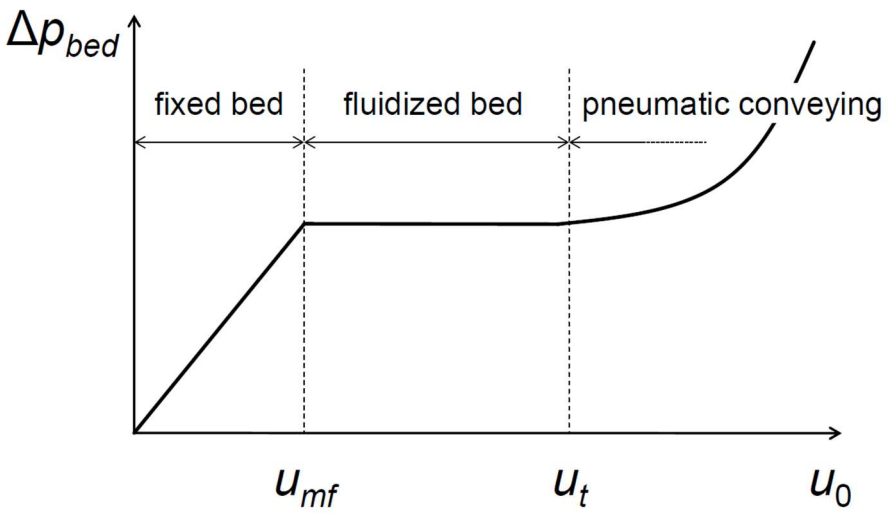

Figure 2-2: Pressure drop across bed – fluidization curve [3].

In the fixed bed regime, the pressure drop is proportional to the gas velocity. The pressure drop is increasing until the minimum fluidization velocity U_{mf} is reached [1]. Beginning with U_{mf} the pressure drop is (statistically) constant across the bed. The bed is called fluidized. After reaching the terminal particle velocity U_t the pressure drop is increasing again. The bed is now operating in the pneumatic conveying region. The width of the fluidized bed range as well as the transition region around U_{mf} can vary, depending on the used particle class. A fluidization curve for a real fluidized bed is shown in Figure 5-4 (chapter 5.1.2) [1,2].

2.4 Particle classification

For classifying the different fluidization types, Geldart [5] performed detailed investigations. One of his key findings was that the fluidization behavior is mainly determined by the particle diameter and the density difference between gas and particles. Geldart is classifying the particles into four groups. The Geldart classification is shown in Figure 2-3 [1,5].

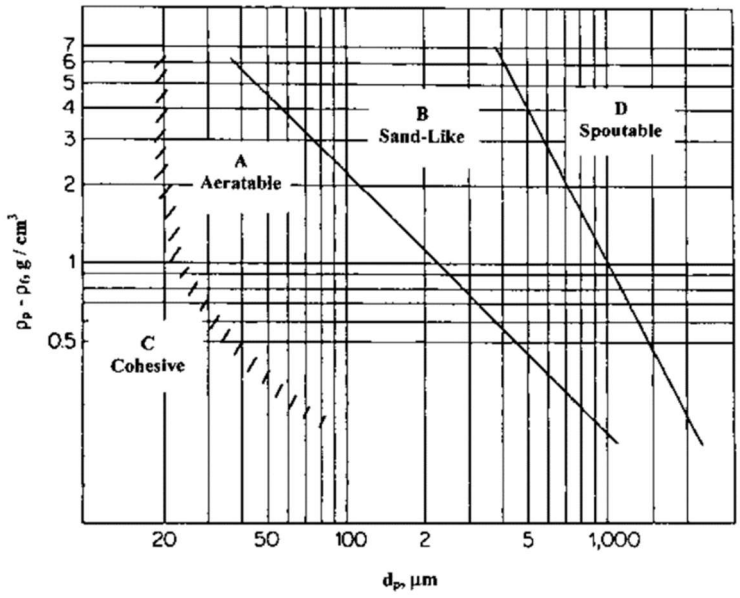

Figure 2-3: Particle classification according to Geldart [6].

The first group, the Geldart A particles consist of small-sized and/or light weighted (ϱ_s < 1.4 g/cm^3) particles [5]. Group A particles are characterized by a homogeneous bed expansion before the bed is transforming into a bubbling bed at higher velocities. Usually, the bubbles are relatively small. Beds of this class are used for circulating fluidized beds as well as for pneumatic transport. Especially for fluid catalytic cracking (FCC) applications, Geldart A particles are often used. Particles in the mean size range (40 µm < d_s < 500 µm) and in the mean density range (1.4 g/cm^3 < ϱ_s < 4 g/cm^3) are in group B. Group B particles are forming bubbles right after reaching the minimum fluidization velocity. The bed is barely expanding. The early and extensive formation of bubbles ensures excellent mixing. Because of these reasons Geldart B particles are the most commonly used particle class in fluidization engineering. Geldart's group C particles are representing cohesive particles or very fine powders. The fluidization of group C particles is difficult because of the high inter-particle forces. Beds with group C particles are preferable forming channeling flows. Because of these reasons, group C particles have just a minor role in industrial applications. The particles in Geldart group D are big and/or very dense. Geldart D particles can show spouting, bubbling or channeling behavior. A usual field of application is the food industry (e.g., coffee beans). A schematic overview of the particle influence on the bed behavior is given in Figure 2-4 [1,2,5].

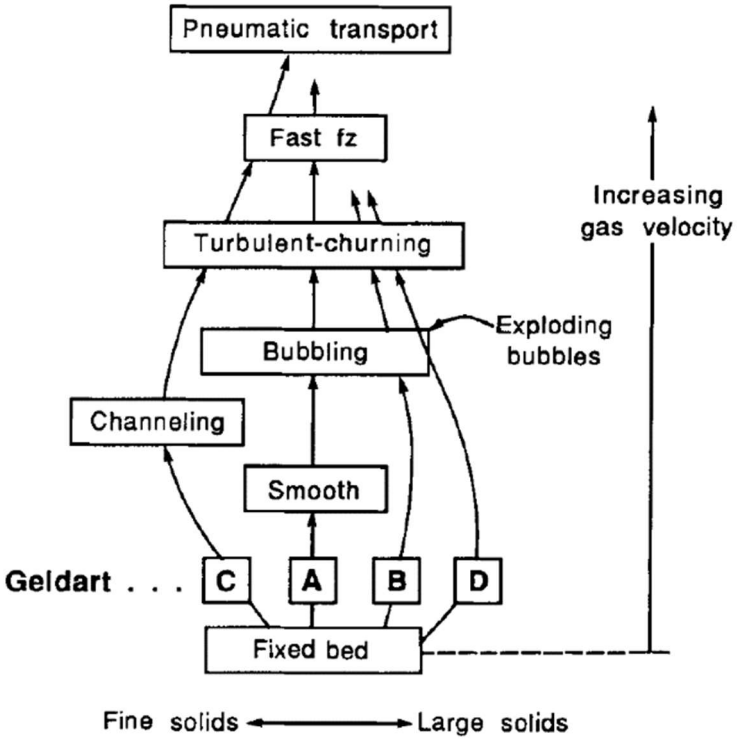

Figure 2-4: Schematics of the bed behavior [1].

2.5 Characteristic values

2.5.1 Volume fraction

One of the most important parameters for fluidized beds is the volume fraction α_s – see Equation (2.1). The volume fraction determines the porosity of the bed. Furthermore, it determines if the suspension is mainly influenced by particle friction or by particle collisions (compare chapter 3.4.3 and chapter 3.6) [2].

$$\alpha_s = \frac{V_s}{V} \tag{2.1}$$

2.5.2 Minimum fluidization velocity

Kunii and Levenspiel [1] are using the pressure drop over the bed as a determination criterion for the minimum fluidization velocity U_{mf}. The minimum fluidization velocity is reached as soon as the pressure drop over a certain bed section equals the particle weight in that section divided by the cross-sectional area of the bed. They proposed an estimation for U_{mf} – Equation (2.2). The left side of the equation is the non-dimensional Archimedes number Ar. The particle volume fraction at fluidization α_{mf} is estimated or obtained by experiments. The sphericity ϕ_s accounts for non-spherical particles [1,6].

$$\frac{d_s^3\ \varrho_g(\varrho_s - \varrho_g)g}{\mu^2} = \frac{1.75}{\alpha_{mf}^3 \phi_s}\left(\frac{d_s U_{mf}\ \varrho_g}{\mu}\right)^2 + \frac{150(1-\alpha_{mf})}{\alpha_{mf}^3 \phi_s^2}\left(\frac{d_s U_{mf}\ \varrho_g}{\mu}\right) \tag{2.2}$$

2.5.3 Terminal velocity

The terminal velocity U_t is the final free-fall velocity of a particle. U_t is representing the upper limit for fluidized beds. In beds with gas velocities higher than U_t bed material is entrained. Terminal velocity is reached when buoyancy and drag force (chapter 3.6) are equal to the particle weight. Kunii and Levenspiel [1] provided an estimation for the terminal velocity of a single particle – shown in Equation (2.3). The expression C_D is the empirically determined drag coefficient (compare with chapter 3.6) [1,2,6].

$$U_t = \sqrt{\frac{4}{3}\frac{d_s\ (\varrho_s - \varrho_g)g}{\varrho_g\ C_D}} \tag{2.3}$$

2.5.4 Sauter mean diameter

A fluidized bed usually contains particles of various sizes. The particle size distribution (PSD) can be represented by the Sauter mean diameter d_{32} – Equation (2.4). It relates the total particle volume to the total particle surface. The term n_i represents the particle number in size class i. The Sauter mean diameter takes smaller particles more into account than bigger ones, because it is most sensitive to the presence of small particles [7]. This behavior is advantageous since the smaller particles have a significantly higher influence on the fluidization [2].

$$d_{32} = \frac{\sum n_i\ d_{si}^3}{\sum n_i\ d_{si}^2} \tag{2.4}$$

2.6 Fluidized bed layouts for biomass gasification

For biomass gasification, the feedstock is mixed with the bed material. In contrast to a fixed bed reactor, no distinctive temperature and reaction zones can be recognized [1]. For an ideal fluidized bed, all gasification reactions are happening at the same time in the whole bed region. The constant temperature, as well as the easy controllable processes, are the advantages of fluidized beds. A drawback is that a lot of pulverized char and ash can be entrained, which is lessening the product gas quality. In Figure 2-5 the most commonly used fluidized bed types for biomass gasification are presented [4].
Figure 2-5 (a) shows the conventional fluidized bed which is operating below the terminal velocity. Therefore, no bed material is entrained. However, since the pyrolysis products (char and ash) are friable, fines are carried in the product gas [4]. In Figure 2-5 (b) a circulating fluidized bed (CFB) is shown. A CFB is operating with gas velocities higher than the terminal velocity. The entrained solids are recirculated by cyclones and fed back to the bed. The suspension in a CFB is more dilute and expanded over the whole facility. If necessary, the product gas quality can be improved by using multiple serial connected cyclones for separating the fine ash and char particles from the gas [1,4].
One big disadvantage of conventional gasification is the fluidizing gas. If air is used, the product gas is diluted with nitrogen, which is decreasing the calorific value. A possibility would be to use pure oxygen or an oxygen-steam mixture as fluidization agent [3]. However, to provide the facility with enough oxygen is expensive. As an alternative, the dual fluidized bed (DFB) was developed. Figure 2-5 (c) shows a DFB in the style of the Güssing reactor [8]. In the Güssing reactor, the heat generation and the gasification of the biomass are separated. The bed material is heated up in the combustion zone by char burn-out. In the combustor, air is used as a fluidization agent. In a cyclone, the flue gas is separated from the bed material. The circulating hot bed material is heating the gasification zone. In the gasifier, steam is used as a fluidization agent to produce a nitrogen-free product gas [1,3,4].

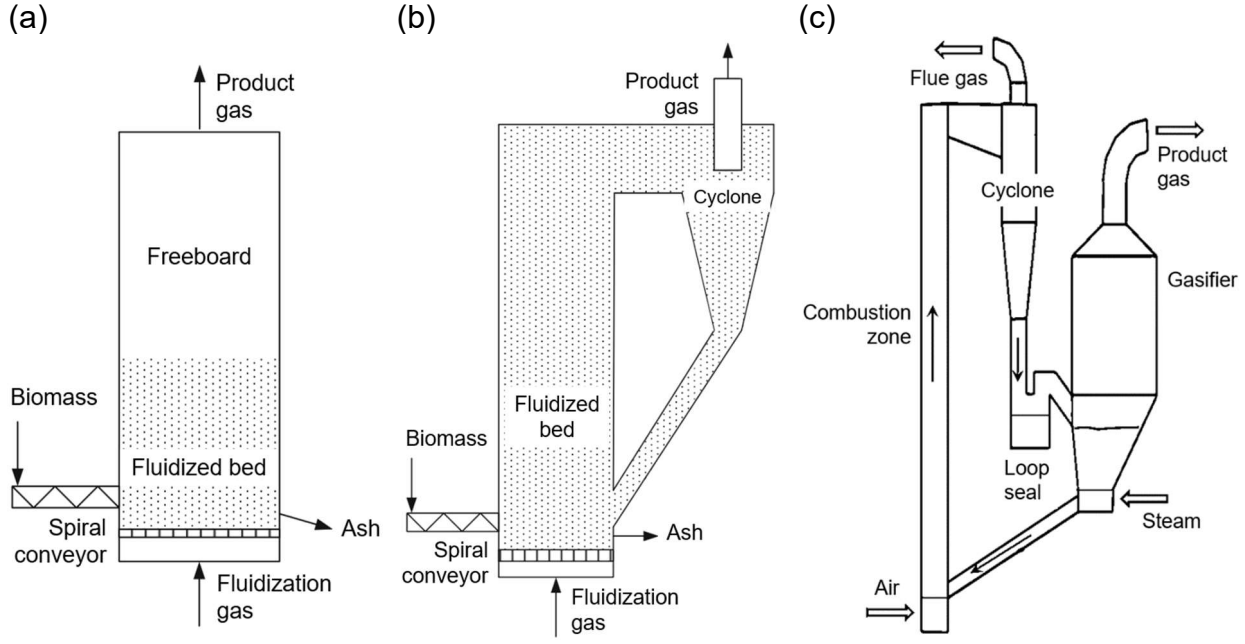

Figure 2-5: Layouts for fluidized beds used in biomass gasification [4], (a) fluidized bed gasifier, (b) circulating fluidized bed gasifier, (c) dual fluidized bed gasifier – type Güssing.

3 Modeling of fluidized beds

For modeling particle-gas flows, two basic strategies for the handling of the solid phase are possible. The granular phase can either be considered as an additional continuous phase, which is mixed with the actual continuous gas phase. Treating the solid phases as fluid is called the Eulerian-Eulerian approach, or also called the Two-Fluid Model (TFM) [9]. The other possibility is the decoupling of the solid phase from the conventional Eulerian approach. The continuous phase is treated and calculated for each cell using the Eulerian approach and the granular phase is tracked by using a Lagrangian approach. The particle paths are tracked through the flow field over several cells. This is called the Euler-Lagrangian approach. Both approaches are shown in Figure 3-1 [9–12].

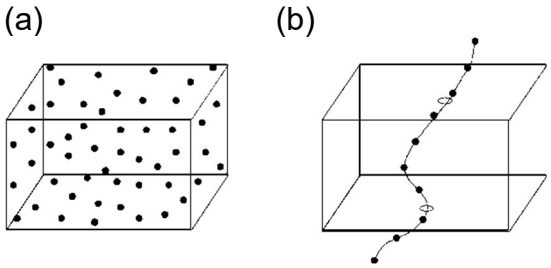

Figure 3-1: Approaches for multiphase flows [11], (a) Eulerian approach, (b) Lagrangian approach.

Independent of the used multiphase-model, interactions between the phases can be included. Interactions between granular and continuous phases are defined by drag laws. Details about the drag laws are provided in chapter 3.6 [9–12].
Collisions between particles of the same (or different) phase can be modeled by using particle interaction models [10]. The used particle interaction models are introduced in chapter 3.4 and chapter 3.5. The available granular multiphase-models in ANSYS® Fluent are shown in Figure 3-2 [13]. The choice of the multiphase-model, the used drag law, and the particle interaction approach is influenced by the solid volume fraction, the particle shape, the particle size distribution, the particle amount and by the superficial gas velocity [9,10,12].

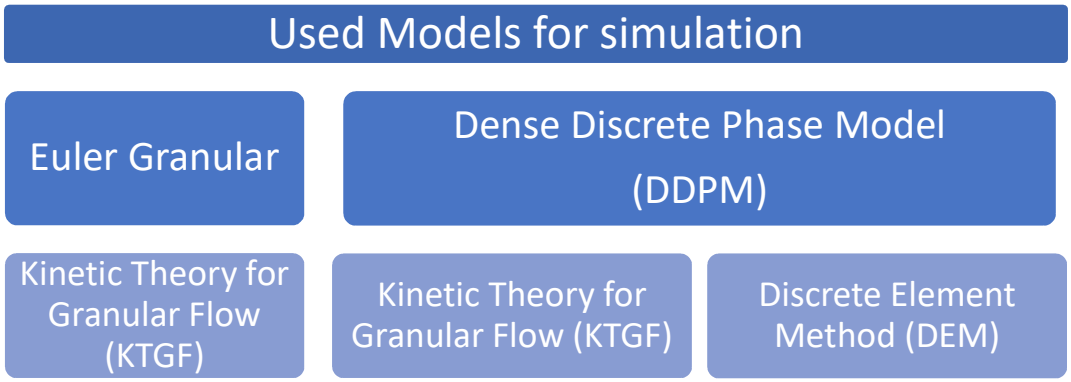

Figure 3-2: Multiphase models for FB's in ANSYS® Fluent [12].

In the following equations, variables for the continuous phases (or primary phase) are subscripted with g (gas), and the granular phase variables are subscripted with s (solid).Variables with the subscripts p and q can either refer to a fluid or a solid phase.

3.1 Euler Granular

The Euler Granular model is a Two-Fluid model (Euler-Euler approach) [9]. Occurring phases are considered as each other interpenetrating continua. These phases are mixed, and there is no difference in handling the discrete phase and the continuous phase. The most commonly used approach was derived by Ishii and Hibiki [14]. For each phase, the governing averaged equations are set up including the regarding volume fraction of the phase (α_i). In addition, the Euler-Euler formulation is assuming that a single pressure is shared by all phases. Equation (3.1) shows the continuity equation for phase q [10,14,15].

$$\frac{\partial}{\partial t}(\alpha_q \varrho_q) + \nabla\left(\alpha_q \varrho_q \vec{v}_q\right) = 0 \tag{3.1}$$

Equation (3.2) shows the momentum equation for a solid phase respectively. The solids stress tensor $\bar{\bar{\tau}}_s$ is including the particle interactions and is derived by the Kinetic Theory for Granular Flow (compare chapter 3.4). The term ∇p_s represents the solids pressure (chapter 3.4.3). For considering interactions between continuous and granular phases, the momentum exchange coefficient K_{qs} is included in the conservative equations. The set of equations is closed by drag laws to obtain the exchange coefficient (more details in chapter 3.6). In $\vec{F}_{other}$ additional models can be included (e.g., lift forces, virtual mass forces) [9,10,12,15].

$$\begin{aligned} &\frac{\partial}{\partial t}(\alpha_s \varrho_s \vec{v}_s) + \nabla(\alpha_s \varrho_s \vec{v}_s \vec{v}_s) = \\ &-\alpha_s \nabla p - \nabla p_s + \nabla \bar{\bar{\tau}}_s + \alpha_s \varrho_s \vec{g} + \sum K_{qs}\left(\vec{v}_q - \vec{v}_s\right) + \vec{F}_{other} \end{aligned} \tag{3.2}$$

The transport equations have to be solved for all phases. Different particle sizes are considered as different phases even when the granular substance is the same. Every additional included particle size class is adding four new conservative equations (3 x momentum, 1 x volume fraction). Reactive systems require even more equations per size class due to species transport (for each scalar). Since the bed material in fluidized beds is seldom uniform in size, including a realistic particle size distribution for an Euler-Granular model is resulting in demanding calculations. However, the advantage of the Euler Granular model is that it can handle very complex flows for uniform particle diameters (e.g., by using the Sauter mean diameter), since no additional equations are required in that case [9,10,15].

3.2 Discrete Phase Model

The Discrete Phase Model (DPM) was developed to overcome the primary disadvantage of the TFM – the inefficient handling of polydisperse systems. The DPM is an Euler-Lagrangian model, which is directly assigning a diameter for each particle. That allows defining several particle diameters for the same granular phase without adding any conservative equations. The calculation of polydisperse systems with DPM is far more efficient. A drawback of DPM is that particle interactions are not included. For dilute flows, these interactions are often neglected (one-way coupling). In literature, different definitions for dilute flows exist. The limit varies between α_s < 0.0001 and α_s < 0.1 [15]. Therefore, DPM cannot be used in fluidized beds. Hence, the Dense Discrete Phase model (DDPM) was developed [10,12,15].

3.3 Dense Discrete Phase Model

The standard DPM is designed for solid volume fractions below α_s < 0.1. For applications with higher volume fractions, the DPM is not suitable (e.g., for fluidized beds) [15]. The main reason for this limitation is the neglecting of the inter-particle forces. For very dense flows, these interactions are having a significant influence on the flow behavior. Modified equations were introduced to account for these interactions [15]. To be able to handle higher particle loadings, the volume fraction of the solids are included. The modified DPM model is called Dense Discrete Phase Model (DDPM). The DDPM is using an Euler-Lagrangian approach for solving the gas-particle flow. For each phase (primary and secondary), the conservative equations are set-up in the Eulerian framework. Additionally, Newton's 2nd law of motion is applied for the solid phases in the Lagrangian framework [15]. Therefore, the DDPM is called a hybrid model, which is combining the advantages of the Euler Granular (including of particle interactions) and the DPM (easy including of different particle size classes) approach [16]. Equation (3.3) and Equation (3.4) are showing the continuity equation and the momentum equation (standard form) for the continuous phase respectively. K_{sg} in Equation (3.4) is the momentum exchange coefficient between the phases due to the drag force [10,15]. In the case that the influence of the dispersed phase on the primary phase cannot be neglected (common for DDPM), an additional source term $\vec{S}_{mom}$ can be included on the right side of the equation to account for these effects (two-way coupling) [10,13,15,17–19].

$$\frac{\partial(\alpha_g \varrho_g)}{\partial t} + \nabla\left(\alpha_g \varrho_g \vec{v}_g\right) = 0 \tag{3.3}$$

$$\begin{aligned} &\frac{\partial}{\partial t}\left(\alpha_g \varrho_g \vec{v}_g\right) + \nabla\left(\alpha_g \varrho_g \vec{v}_g \vec{v}_g\right) = \\ &-\alpha_g \nabla \mathrm{p} + \nabla\left(\alpha_g \bar{\bar{\tau}}\right) + \alpha_g \varrho_g \vec{g} + \alpha_g \varrho_g \sum \vec{F}_{other} + \sum K_{sg}\left(\vec{v}_s - \vec{v}_g\right) + \vec{S}_{mom} \end{aligned} \tag{3.4}$$

The equation of motion for the particles is defined in the Lagrangian approach, see Equation (3.5). The particle trajectories are obtained by stepwise integration of Equation (3.5). The particle velocity is already obtained by Newton's 2nd law for each trajectory point – Equation (3.6). In addition, the solution for the solid volume fraction is directly taken from the Lagrangian approach [10]. Thus, only the conservative equations for the non-discrete phases have to be calculated. The values obtained from the Lagrangian approach have to be averaged for each cell before they can be used in the Eulerian framework (all particles inside the cells are used for averaging). If the particles are large in relation to cell size, one particle could span over multiple cells, making it difficult to associate the particles to a particular cell. Furthermore, the averaging becomes more reliable with a higher particle number in the actual cell. For these reasons, it is important that the cells are big enough for a sufficient number of particles. ANSYS® recommends that the minimum cell volume should be at least equal to the volume of 5-10 packed particles [10,12,13,15].

$$\frac{d\vec{v}_s}{dt} = F_{drag}\left(\overrightarrow{v_g} - \overrightarrow{v_s}\right) + \frac{\vec{g}\left(\varrho_s - \varrho_g\right)}{\varrho_s} + \vec{f}_{coll} + \vec{f}_{s,other} \tag{3.5}$$

$$\frac{d\vec{x}}{dt} = \vec{v}_s \tag{3.6}$$

F_{drag} is the coefficient of proportionality which accounts for the interphase momentum exchange (also see chapter 3.6) [15]. The term $\vec{f}_{coll}$ is considering the previous mentioned particle interactions. These interactions can be considered either by the Kinetic Theory of Granular Flow (KTGF) or by direct resolving of the interaction with the Discrete Element Method (DEM). When particle-particle interactions are included in the calculation, the flow is called four-way coupled [10]. These approaches will be explained in the following chapters. In $\vec{f}_{s,other}$ additional acceleration forces can be included. Examples for additional models are the Saffman lift force [20], the virtual mass force [21] or the Brownian force [22]. The advantage of the DDPM model is the better representation of the particle behavior. In addition, particle size distributions can easily be included. Furthermore, the direct calculation of the particle velocities and the volume fractions in the Lagrangian framework requires fewer conservative equations for multiple particle diameter sizes than the Euler Granular model [10,15,17].

3.4 Kinetic Theory of Granular Flow

The particle-particle interactions considered in $\vec{f}_{coll}$ are highly dissipative [9]. The non-conservative behavior is caused by the inelastic deformation and the friction between individual particles. The particle movements are determined by the kinetic transport between collisions and the energy transport during collisions [23]. With increasing particle loading and higher particle velocities, collisions are more likely (indicated in Figure 3-3). The dissipation is increasing due to more particle interactions. These particle interactions are approximated by the Kinetic Theory of Granular Flow (KTGF) [10].

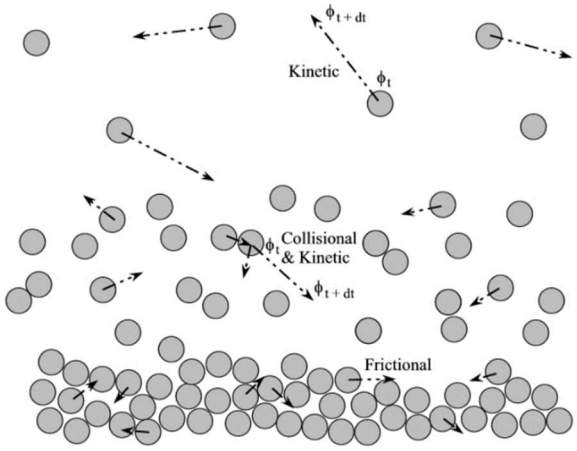

Figure 3-3: Transport mechanism for fluid-particle systems [24].

The main idea of the KTGF is, to model the mechanical energy of the granular phase as velocity fluctuations around a mean particle velocity [10]. That kinetic energy is then dissipated. Therefore, instead of resolving all particle collisions, the interactions are averaged for the particle gas flow. The particle forces are obtained by the solids stress tensor $\bar{\bar{\tau}}_s$ as defined in Equation (3.7) [10,15,23,25,26].

$$\vec{f}_{coll} = -\frac{1}{\varrho_s} \nabla \bar{\bar{\tau}}_s \tag{3.7}$$

Multiphase models using the KTGF approach are relatively fast due to the approximated interactions [27]. An issue of KTGF is the changing correlation between solid stress tensor and the dimensionless shear rate $\gamma°$ for different particle volume fractions – shown in Figure 3-4 [9]. Therefore, KTGF has problems when simulating applications with strongly different and/or changing solid volume fractions (Compare with chapter 3.4.1). Especially for applications with long frictional particle contacts in combination with high particle loadings, the KTGF model is not the best choice [27].

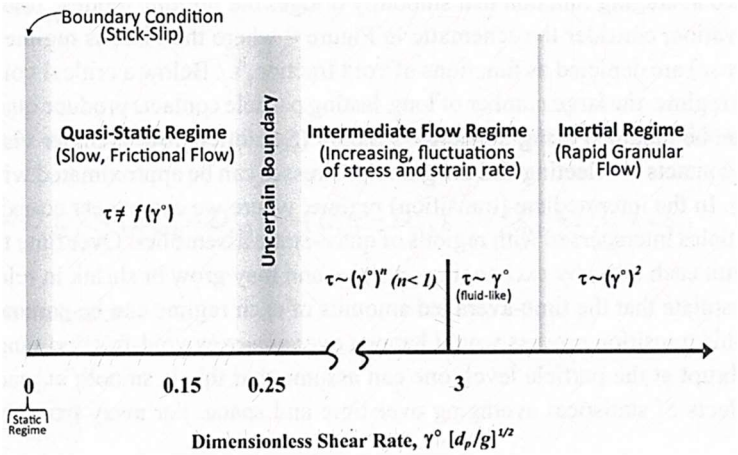

Figure 3-4: Regime map of the rheology of granular materials [27].

For very dilute regimes, the KTGF approach as suggested by Lun et al. [28] is working well. For the transition zone between dilute and dense flow and near-wall regions, the model by Johnson and Jackson [29] can be included to improve predictions. The Johnson and Jackson [29] approach is introduced in chapter 3.7. In their model, a slip-wall boundary condition for the solid phase is added. For very dense flows the frictional effects are dominating, an additional model, e.g., by Schaeffer [30] can improve the results. The transition zones between the regimes are not clearly defined. In Pannala et al. [27] an overview of the different regimes and models can be found [27].

3.4.1 Granular temperature

The granular temperature Θ_s is a measurement for the random particle fluctuations and is a representation of the kinetic particle energy [23]. It is assumed that the fluctuations are the same in all directions. In Equation (3.8), the formal definition of the granular temperature is shown. The expression v_s' specifies the random velocity fluctuations of the particles [23].

$$\Theta_s = \frac{v_s' \, v_s'}{3} \tag{3.8}$$

In Equation (3.9) the basic form of the transport equation for the granular temperature, as derived by Ding and Gidaspow [23], is shown. The term $\bar{\bar{\tau}}_s : \nabla \vec{v}_s$ represents the energy production by the solid stress tensor $\bar{\bar{\tau}}_s$, which consists of the deformation work and the energy transfer of the particles. The energy dissipation is considered by the term $k_\Theta \nabla \Theta_s$. Inelastic collisions are considered by γ_{Θ_s}. The term Φ_{sg} is considering the transfer of the fluctuating energy between the phases [31,32].

$$\frac{3}{2}\left[\frac{\partial}{\partial t}(\alpha_s \varrho_s \Theta_s) + \nabla(\alpha_s \varrho_s \vec{v}_s \Theta_s)\right] = \bar{\bar{\tau}}_s : \nabla \vec{v}_s + \nabla(k_\Theta \nabla \Theta_s) - \gamma_{\Theta_s} + \Phi_{sg} \tag{3.9}$$

Based on the granular temperature transport equation, different approaches for calculating the granular temperature are available. The first possibility is to solve the partial differential equation of the granular temperature transport. Another approach is the DPM-averaged granular temperature, which is only available for DDPM models [10]. Furthermore, for very dense packed beds, where the random fluctuations are small, a constant value for the granular temperature can be set [10]. For the calculations in this work, the algebraic approach for the granular temperature was used. The advantage is that no additional transport equation is needed since the convective and the diffusive terms in Equation (3.9) are neglected. That simplification can be done since the production and the dissipation of the granular energy are in equilibrium for fluidized beds [10]. The resulting algebraic formulation is shown in Equation (3.10). The transfer of the fluctuating energy Φ_{sg} is calculated by the granular temperature and the momentum interphase exchange coefficient K_{sg}, as shown in Equation (3.11) [31,32].

$$0 = \bar{\bar{\tau}}_s : \nabla \vec{v}_s - \gamma_{\Theta_s} + \Phi_{gs} \tag{3.10}$$

$$\Phi_{sg} = -3K_{sg}\Theta_s \tag{3.11}$$

3.4.2 Solids stress tensor

The solid stress tensor $\bar{\bar{\tau}}_s$ consists of a collisional part and a kinetic part of the particle interactions – see Equation (3.12) [23,25]. The kinetic stress τ^k is due to the kinetic transport between collisions. The collisional stress τ^c is caused by particle collisions [10].

$$\bar{\bar{\tau}}_s = \tau^k + \tau^c \tag{3.12}$$

Instead of calculating these stresses, the solid stress tensor is defined by the granular viscosity μ_s and the bulk viscosity λ_s [25]. These terms will be explained in the next chapters. The relation is shown in Equation (3.13) and depends on the granular viscosity μ_s, the bulk viscosity λ_s and the volume fraction of the solids phase α_s. These parameters will be explained in more detail in the following chapters. The unit tensor $\bar{\bar{I}}$ is necessary to obtain a tensor from the scalars in the second term [15,23,25].

$$\bar{\bar{\tau}}_s = \alpha_s \mu_s \left(\nabla \vec{v}_s + \nabla \vec{v}_s^{\,T}\right) + \alpha_s \left(\lambda_s - \frac{2}{3}\mu_s\right) \nabla \vec{v}_s \bar{\bar{I}} \tag{3.13}$$

3.4.3 Granular viscosity

The granular viscosity is the shear viscosity of the suspension due to the kinetic motion ($\mu_{s,kin}$) and the particle interactions ($\mu_{s,coll}, \mu_{s,fr}$) – see Equation (3.14) [12]. The particle interactions are separated into a collisional part $\mu_{s,coll}$ and a frictional part $\mu_{s,fr}$ [10]. The granular viscosity is equivalent to the molecular viscosity of a fluid. It is used to get the viscosity for the whole suspension including the solids. For calculating the granular viscosity, the granular temperature Θ_s is necessary. The granular temperature is a measurement for the random particle fluctuations and is a representation of the kinetic particle energy. The definition of the granular temperature can be found in Equation (3.9) (chapter 3.4.1) [23,25].

$$\mu_s = \mu_{s,coll} + \mu_{s,kin} + \mu_{s,fr} \tag{3.14}$$

Collisional viscosity

The collisional viscosity $\mu_{s,coll}$ describes the shear viscosity due to the particle collisions. It is representing the energy transport by particle collisions [25]. Inside ANSYS® Fluent the approach by Gidaspow [25] is used. For obtaining $\mu_{s,coll}$ the particle interactions are modeled according to Equation (3.15). The fluctuating energy is represented by the granular temperature Θ_s (definition in chapter 3.4.1). Collisions between particles are included by using the coefficient of restitution η_{ss}. To account for dense particle-gas flows, a radial distribution function $g_{0,ss}$ (chapter 3.4.5) is included in the equation [23,25,28,32].

$$\mu_{s,coll} = \frac{4}{5}\,\alpha_s \varrho_s d_s g_{0,ss}\,(1+\eta_{ss})\left(\frac{\Theta_s}{\pi}\right)^{1/2} \qquad (3.15)$$

Kinetic viscosity

The kinetic viscosity is representing the energy of the free particle movement (also see Figure 3-3). ANSYS® Fluent provides two models for the kinetic contribution of the granular viscosity. Models derived by Syamlal and O'Brien [32] and by Gidaspow [25] are available. Both approaches have a similar structure. For the calculation, the granular temperature Θ_s, the radial distribution function $g_{0,ss}$ (see chapter 3.4.5) and the particle-particle restitution coefficient η_{ss} is needed. In Equation (3.16) the approach by Gidaspow [25] is shown respectively [12,13].

$$\mu_{s,kin} = \frac{10 d_s \varrho_s \sqrt{\Theta_s \pi}}{96\,\alpha_s(1+\eta_{ss})\,g_{0,ss}}\left[1+\frac{4}{5}g_{0,ss}\,\alpha_s(1+\eta_{ss})\right]^2 \alpha_s \qquad (3.16)$$

Frictional viscosity

The frictional viscosity $\mu_{s,fr}$ contribution of the granular viscosity is important when the packing limit is reached [10]. In that case, the particles are not colliding anymore, and the particle interactions are reduced to frictional contacts. Frictional models are deactivated by default in ANSYS® Fluent. In Equation (3.17) the expression by Schaeffer [30] is shown. Solids pressure p_s and the internal friction angle φ are needed for the calculation. The expression I_{2D} is the second invariant of the deviatoric stress tensor [10].

$$\mu_{s,fr} = \frac{p_s \sin\varphi}{2\sqrt{I_{2D}}} \qquad (3.17)$$

3.4.4 Solids pressure

The solids pressure p_s is an additional term in the momentum Equation (3.2) to account for particle volume fractions below the packing limit [10]. Similarly to the granular viscosity, the solids pressure is parted into a kinetic and a collisional part [10]. The kinetic contribution is calculated by the granular temperature and the particle fraction. The collisional contribution is proportional to the repulsive particle contact force [23]. For all calculations in this work, the approach by Lun et al. [28] was used for the solids pressure [10,12].

3.4.5 Radial distribution function

The radial distribution function $g_{0,ss}$ acts as a correction factor for increasing particle volume fractions. It is modifying the probability of collisions between particles in denser regions [28]. It can be seen as a non-dimensional distance between particles. The general form of the radial distribution function is shown in Equation (3.18). In the equation, s is the distance between particles and d_s is the particle diameter. Therefore, the radial distribution describes the transition between compressible flow (particle volume fraction below the packing limit) to incompressible flow (particle volume fraction near or equal the packing limit) [10,28]. For all calculations in this work, the approach by Lun et al. [28] was used for the radial distribution function [10,12].

$$g_{0,ss} = \frac{s + d_s}{s} \tag{3.18}$$

3.4.6 Bulk viscosity

The bulk viscosity describes the resistance of the particle agglomeration against expansion and compression inside the suspension [28]. By default, the bulk viscosity is set to zero. The bulk viscosity model by Lun et al. [28] – shown in Equation (3.19) – was used in this work [10].

$$\lambda_s = \frac{4}{3}\alpha_s^2 \varrho_s d_s g_{0,ss} \left(1 + \eta_{ss}\right) \left(\frac{\Theta_s}{\pi}\right)^{1/2} \tag{3.19}$$

3.5 Discrete Element Method

Another possibility to account for the particle-particle interactions in $\vec{f}_{coll}$ is the Discrete Element Method (DEM), which was first introduced by Cundall and Strack [33]. The DEM approach is calculating all inter-particle collisions [10]. The particles are tracked with a very small time step in order to dissolve all collisions (contact time between particles is very short). In case of a collision, an overlap of the colliding particles is allowed (soft-sphere approach – see Figure 3-5). That overlap δ is considered as a deformation. Different models exist to obtain the contact force from the particle deformation [10,33].

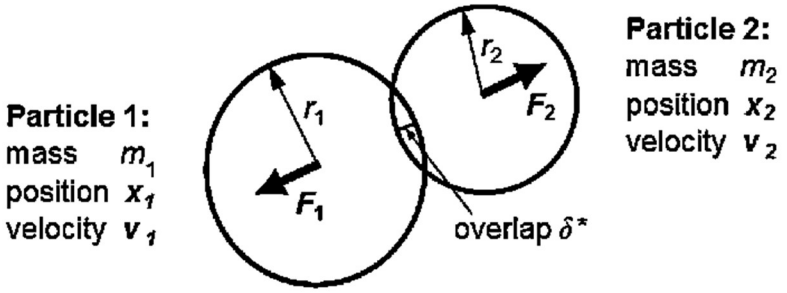

Figure 3-5: DEM - soft sphere approach [10].

One commonly used model is the spring-dashpot law based on the work by Cundall and Strack [33] and by Tsuji et al. [34]. The spring dash-pot law defines a linear relationship between the deformation and the contact force. The calculation of the force acting from particle j on particle i is presented in Equation (3.20). For calculations, the spring-dashpot constant K and the coefficient of restitution η_{ss} are required. Furthermore a damping coefficient γ and a unit vector $\vec{e}_{ij}$ (vector between particles i and j) are necessary [33,35].

$$\vec{F}_i = \left(K\delta + \gamma\left(\vec{v}_{ij} \cdot \vec{e}_{ij}\right)\right)\vec{e}_{ij} \qquad (3.20)$$

The governing equations behind the DEM models are far simpler than the ones for the KTGF approach. However, because of the small time steps and the need to resolve all particle contacts, the DEM approach is far more numerically demanding than the KTGF approach [12]. Ergo, the DEM approach is rarely used for industrial scaled applications, which can include billions of particles. The advantage is the potentially much better prediction of the solid-gas flow [9,36].
In the ANSYS® Theory Guide [10] and ANSYS® User´s Guide [13], equations for the estimation of the particle time step are given. These set of equations – shown in Equations (3.21) to (3.24) – are requiring the coefficient of restitution η_{ss} and the spring-dashpot coefficient K. First a reduced mass m_{12} is calculated to account for the mass ratio between the colliding particles ($\mathrm{m}_1, \mathrm{m}_2$ are the masses of the collision partners). Using the coefficient of restitution, the loss factor f_{loss} is calculated, which accounts for the energy loss due to non-ideal elastic collisions [10,12].

$$\mathrm{m}_{12} = \frac{\mathrm{m}_1\,\mathrm{m}_2}{\mathrm{m}_1 + \mathrm{m}_2} \qquad (3.21)$$

$$\mathrm{f}_{loss} = \sqrt{\pi^2 + ln(\eta_{ss})^2} \qquad (3.22)$$

These values are used to calculate the collision timescale t_{coll}. Finally, for ensuring a sufficient resolution of the collisions, the particle time step $\Delta\mathrm{t}_p$ (ANSYS® specifies a valid range for $\Delta\mathrm{t}_p$) is calculated according to Equation (3.24) [10,12].

$$\mathrm{t}_{coll} = \mathrm{f}_{loss}\sqrt{\frac{\mathrm{m}_{12}}{K}} \qquad (3.23)$$

$$\Delta\mathrm{t}_p = {}^{\mathrm{t}_{coll}}/_{50} \quad or\ up\ to \quad \Delta\mathrm{t}_p = {}^{\mathrm{t}_{coll}}/_{5} \qquad (3.24)$$

3.6 Drag laws

The drag law couples the equations of the continuous phase and the dispersed phase with each other. For coupling the conservative Equations (3.2) and (3.4), the momentum interphase exchange coefficient K_{sg} is used [23]. For the force balance in the Lagrangian formulation (chapter 3.3) the coefficient of proportionality F_{drag} is used [15]. The relation between K_{sg} and F_{drag} is shown in Equation (3.25) [10,15].

$$F_{drag} = \frac{K_{sg}}{\varrho_s \alpha_s} \qquad (3.25)$$

The choice of the drag law is significantly influencing the accuracy of the results [9]. To obtain the drag force, a drag coefficient C_D is used. Since the drag coefficient is dependent on the relative particle Reynolds number Re_s (or Re_p) and the particle volume fraction α_s, many different approaches were developed, mainly based on experiments with uniform sized spheres [9]. The relation between drag coefficient and Re_s is not constant (see Figure 3-6). The picture shows how the relation of the drag coefficient is changing with Re (for a single sphere) [37].

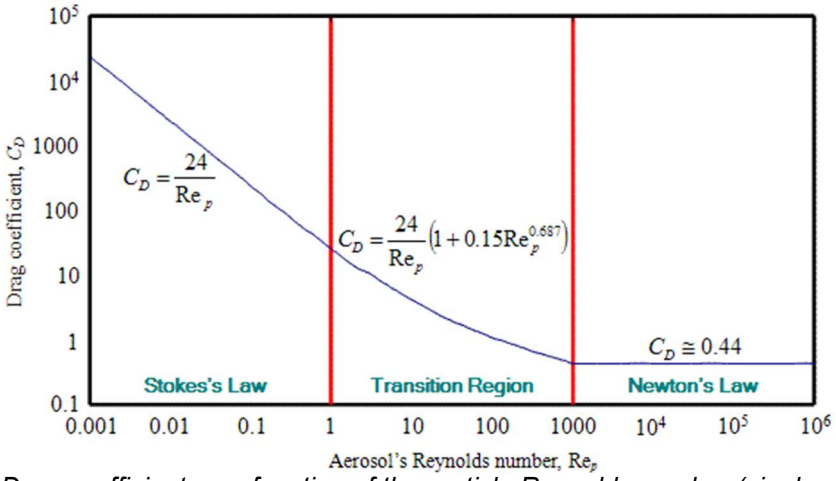

Figure 3-6: Drag coefficient as a function of the particle Reynolds number (single sphere) [37].

For low Re_s the viscous effects are dominating (Stokes law region, linear function) [9]. However, for increasing Re_s, inertial effects are getting more important and the relation is getting non-linear (transition region) – also compare with Sommerfeld et al. [9]. Hence, the particle Reynolds number Re_s is used as a determiner for the drag law. The definition of Re_s can be found in Equation (3.26) [9,10].

$$Re_s = \frac{\varrho_g \, d_s \left|\overrightarrow{v_s} - \overrightarrow{v_g}\right|}{\mu_g} \tag{3.26}$$

Furthermore, neighboring particles are disturbing the ideal flow stream passing a particle [9]. Consequently, an increasing particle volume fraction is resulting in a higher drag force. Therefore, α_s is included in the drag law. For non-spherical particles, a correction term ϕ (sphericity) can be included. However, this drag law modification is just reliable for nearly spherical particles. For particles with other shapes, specific drag laws have to be used (also the effect of the particle rotation may have a significant influence) [9,10]. Generally, the momentum exchange coefficient K_{sg} is calculated by a drag function c which is dependent on the drag coefficient C_D. The basic form is shown in Equation (3.27) [15]. The correlation between c and C_D, is defined by the drag law [12,15,23].

$$K_{sg} = \frac{18\alpha_s \mu_g c(C_D)}{d_s^2} \tag{3.27}$$

For simulations of dense fluidized beds, commonly used drag laws are the approaches by Gidaspow et al. [25,38,39], Wen and Yu [39] and by Syamlal and O'Brien [26]. Besides the particle Reynolds number, these models are also accounting for the dense particle volume fraction in fluidized beds. Furthermore, these models are recommended by ANSYS® and are implemented in ANSYS® Fluent [10].

3.6.1 Drag law by Wen and Yu

The drag model derived by Wen and Yu [39] is an extension of the basic drag law for the flow past a sphere. It adds a correction term to account for the effects of surrounding particles [36]. It is based on experiments with homogenous particle structures. Hence, it is optimized for more dilute flows (solid phase volume fraction is significantly lower than of the fluid phase – e.g., for conveying transport regime, also see chapter 2.1) [13]. Consequently, the Wen-Yu drag law is not the best choice for very dense fluidized beds close to packing limit [10]. The correlation for the momentum exchange coefficient is shown in Equation (3.28). In Equation (3.29) the expression of the drag coefficient C_D is given. For the drag law, the relative particle Reynolds number Re_s is required, its definition is shown in Equation (3.26) [10,36].

$$K_{sg} = \frac{3}{4}\, C_D \frac{\alpha_s\, \alpha_g\, \varrho_g \left|\overrightarrow{v_g} - \overrightarrow{v_s}\right|}{d_s}\, \alpha_g^{-2.65} \tag{3.28}$$

$$C_D = \frac{24}{Re_s}\left(1 + 0.15\, {Re_s}^{0.687}\right) \tag{3.29}$$

3.6.2 Drag law by Gidaspow

The drag law derived by Gidaspow et al. [25] is a combination of the Wen-Yu [39] model and the Ergun [38] equation. Depending on the actual particle volume fraction, the model is using either the Wen-Yu or the Ergun approach. With the combination of the models, the Wen-Yu restriction to dilute flows is bypassed. For dilute flows (α_g > 0.8), the Wen-Yu model is used. The correlation is shown in Equation (3.30) and is the same as shown in Equation (3.28). In denser regions (α_g ≤ 0.8), the approach by Ergun is applied. The Ergun equation is shown in Equation (3.31). The definition of the drag coefficient C_D is determined by the relative particle Reynolds number Re_s. The relations for C_D are given in Equation (3.32). For fluidized beds, ANSYS® recommends the Gidaspow drag law [10,12,36].

$\alpha_g > 0.8$ $$K_{sg} = \tfrac{3}{4}\, C_D \frac{\alpha_s\, \alpha_g\, \varrho_g \left|\overrightarrow{v_s} - \overrightarrow{v_g}\right|}{d_s}\, \alpha_g^{-2.65} \tag{3.30}$$

$\alpha_g \leq 0.8$ $$K_{sg} = 150\, \frac{\alpha_s^2\, \mu_g}{\alpha_g\, {d_s}^2} + 1.75\, \frac{\alpha_s\, \varrho_g \left|\overrightarrow{v_s} - \overrightarrow{v_g}\right|}{d_s} \tag{3.31}$$

$$C_D = \begin{cases} \dfrac{24}{Re_s}\left(1 + 0.15\, {Re_s}^{0.687}\right), & Re_s < 1{,}000 \\ 0.44\ , & Re_s \geq 1{,}000 \end{cases} \tag{3.32}$$

Since the Gidaspow is offering a specific set of equations for dilute and dense regions, as well as it is considering the particle volume fraction and the particle Reynolds number it is the preferred drag law for fluidized beds [10,13].

3.6.3 Drag law by Syamlal and O'Brien

The approach by Syamlal and O'Brien [26] is based on the terminal particle velocity U_t. The drag function is based on the formulation derived by DallaValle [40]. The calculation of the momentum exchange coefficient K_{sg} is presented in Equation (3.33). Depending on the particle volume fraction, two different formulations of the terminal velocity are provided. As shown in Equation (3.35), α_g is influencing the non-dimensional coefficients A and B [10,26].

$$K_{sg} = \frac{3}{4} C_D \frac{\alpha_s \alpha_g \varrho_g \left|\overrightarrow{v_s} - \overrightarrow{v_g}\right|}{d_s U_t^2} \tag{3.33}$$

$$C_D = \left(0.63 + \frac{4.8}{\sqrt{Re_s / U_t}}\right)^2 \tag{3.34}$$

$$U_t = \frac{1}{2}\left(A - 0.06\, Re_s + \sqrt{(0.06\, Re_s)^2 + 0.12\, Re_s\,(2\,B - A) + A^2}\right)$$
$$A = \alpha_g{}^{4.14}, \qquad B = \begin{cases} 0.8\,\alpha_g^{1.28}, & \alpha_g \le 0.85 \\ \alpha_g^{2.65}, & \alpha_g > 0.85 \end{cases} \tag{3.35}$$

3.7 Johnson and Jackson wall boundary condition

Johnson and Jackson [29] developed a wall boundary condition (BC) for the solid phase. The Johnson and Jackson approach can improve the prediction of the particle behavior next to the wall for DDPM-KTGF calculations. Johnson and Jackson are adding heuristic friction by adding a boundary at which some particles collide and the rest slide [41]. The most important parameter is the specularity coefficient φ. It is the average fraction of the relative tangential momentum transfer due to particle-wall collisions [42]. The sliding particles are considered with Coulomb friction [41]. The specularity coefficient is ranging from φ = 0 (free-slip BC) for a perfect specular collision, to φ = 1 (no-slip wall BC) for a perfect diffusive collision [43]. When using values between φ = 0 and φ = 1 the BC is called to be a partial-slip BC. For a perfect specular particle collision, the angle of incidence is the same as the angle of reflection. In contrast to that, a perfect diffusive collision is reflecting the particle in random directions. The reasons for diffusive collisions are the roughness of wall and particle surface. Therefore, the specularity coefficient is not the same as the wall/particle coefficient of restitution η_{ws}. The coefficient of restitution is representing the ratio between incidence velocity and reflection velocity (η_{ws} = 0 represents a perfectly inelastic collision, and η_{ws} = 1 is representing a perfect elastic collision) [29,43]. In ANSYS® Fluent, the specularity coefficient is included in the shear force $\vec{\tau}_s$ for the solid phase wall BC (for the granular temperature), see Equation (3.36) [10]. $\vec{U}_s$ is the particle velocity parallel to the wall and $\alpha_{s,max}$ the maximum packing for the particles [10]. The Johnson and Jackson approach is not necessary for DDPM-DEM calculations since sliding is defined in the DEM panel with friction coefficients [10].

$$\vec{\tau}_s = -\frac{\pi}{6}\sqrt{3}\varphi \frac{\alpha_s}{\alpha_{s,max}} \varrho_s g_0 \sqrt{\Theta_s}\vec{U}_s \tag{3.36}$$

4 Simulation of NETL SSCP challenge I

In CFD, the validation against experimental data is essential. Furthermore, CFD challenges were introduced to benchmark state-of-the-art multiphase models and to establish the predictive capability of simulations [44,45]. The reason behind blind tests is to get to know how sensitive models are, and how reliable the prediction is when no experimental data is available from the very beginning [45].
In a CFD challenge, a problem is stated which should be solved [44]. Usually, after a given due date, the simulation results are collected, and the experimental data will be published [46]. The chosen challenges (Table 4-1) were published by the Departments of Energy's (DOE) National Energy Technology Laboratory (NETL). The problem description, as well as the released experimental data, can be found on the NETL homepage [47].

Table 4-1: Simulated challenges [46].

Challenge	Type of problem
NETL challenge I	non-reacting, bubbling fluidized bed with uniform particles
NETL challenge III	non-reacting, bubbling and circulating fluidized beds with particle size distribution

4.1 Problem description

A laboratory-sized fluidized bed was simulated to get experience in multiphase modeling. This challenge was chosen because of the small dimensions and the uniform size of the particles [45]. Under this frame conditions, all multiphase models have acceptable calculation times [47].

4.1.1 Geometry

The NETL challenge SSCP I (released in 2013) describes a rectangular and non-reacting bubbling fluidized bed. The dimensions of the bed are shown in Table 4-2. Because of the relatively small depth of 0.075 m, the challenge providers were calling NETL I a pseudo-2-dimensional bed [45]. The bed height ensures that the pressure drop between outlet and atmosphere can be neglected [45]. In Figure 4-1, the geometry used for simulations and the experimental facility can be seen. The squares are indicating the measurement volumes (also see chapter 4.2) [45].

Table 4-2: Dimensions for the rectangular fluidized bed [45].

Dimension		
Height (H)	(m)	1.22
Width (W)	(m)	0.23
Depth (D)	(m)	0.075

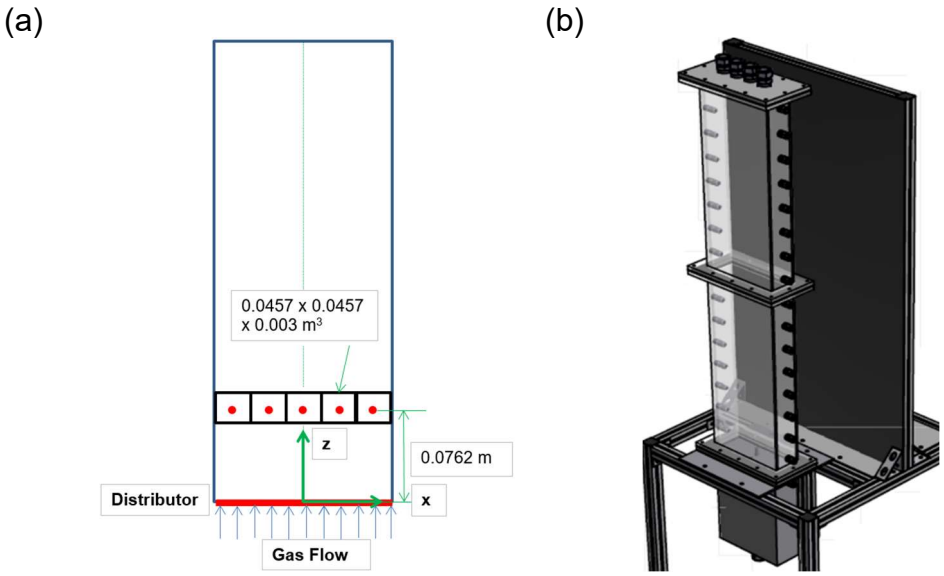

Figure 4-1: Schematics of the SSCP challenge.
(a) geometry used for simulations, (b) experimental facility [47].

For the experiment, a plenum chamber was used. The air entered the bed through a plate with circular holes. For simulations, the plenum chamber and the distributor plate were neglected. For calculations without the plenum chamber, NETL provides the pressure drop across the distributor (measured without particles) [45,47].
The experimental data is provided for three different superficial gas velocities which are representing 2, 3 and 4-times the minimum fluidization velocity (U_{mf} = 1.05 m/s). With these velocities, the bed is operating in the fluidized regime [45–47]. The initial particle inventory was constant for all cases. Case I was investigated in detail. Afterwards, only selected settings for case II and case III were tested [45].

Table 4-3: NETL I variations [47].

Case	Total bed weight (kg)	Superficial gas velocity (m/s)	Pressure drop across distributor (kPa)
Case I	1.8998	2.19	1.86
Case II	1.8998	3.28	4.21
Case III	1.8998	4.38	7.52

4.1.2 Particle properties

The particles are uniform sized nylon beads. The sphericity is high so that they can be considered as spheres. The diameter of the nylon beads is about d_s ~ 3 mm, and the particle density is ϱ_s = 1,131 kg/m^3. Following Geldart´s [5] classification, the particles are Geldart D particles (see chapter 2.4). This particle class represents large and/or very dense particles. Depending on the type of gas distributor, the bed can show spouting or bubbling behavior. During the experiment, nearly no particles were lost [2,5]. The particle amount was low enough to allow application of a DDPM-DEM approach with acceptable calculation times [47], and the total initial particle load was m_s = 1.8998 kg. The specific particle properties are listed in Table 4-4 [45,47]. The initial particle amount was calculated to 93,285 particles, which represents the full resolution of the particle number in the DDPM models [45].

Table 4-4: Particle properties of the nylon beads [45].

	dimension	value	uncertainty (± %)
Minimum fluidization velocity	(m/s)	1.05	
Void fraction (fluffed)	(-)	0.420	5
Void fraction (packed)	(-)	0.4	5
Bulk density (fluffed)	(kg/m^3)	635.8	1
Bulk density (packed)	(kg/m^3)	667	1
Particle density	(kg/m^3)	1,131	3.5
Particle size (Sauter mean)	(µm)	3,256	
Sphericity	(-)	0.94	
Particle-wall coefficient of restitution (normal)	(-)	0.92	
Particle-wall velocity ratio (tangential)	(-)	0.65	
Particle-particle coefficient of restitution (normal)	(-)	0.84	
Particle-wall coefficient of friction (rolling)	(-)	0.037	
Particle-wall coefficient of friction (sliding)	(-)	0.35	

4.2 Provided data

For validation of the multiphase models, four measured variables were used: Mean pressure drop across the bed, mean vertical particle velocity, mean horizontal particle velocity and the mean granular temperature [47].

4.2.1 Mean pressure drop across the bed

The pressure drop was measured between several sections. The first section includes the distributor and the plenum chamber [47]. These parts were not included in the model, to keep calculation time low. Therefore no values for the pressure drop in that section were obtained. The second section is inside the bed region between z = 0.0413 m and z = 0.3048 m [45,47]. The area-weighted-average of static pressure was used for the evaluation of the simulation results. These values were then again averaged throughout 10 seconds [47].

4.2.2 Particle velocity

For the particle velocity measurements, a High-speed Particle Image Velocimetry (HsPIV) was used [48,49]. The particle velocity is available for five points at the same height (z = 0.0762 m) in the bed [45]. The velocity was separately analyzed for vertical and horizontal velocity components (see Figure 4-1). Velocity components in the bed depth direction are neglected. These velocities are the average of the five subsections shown in Figure 4-1 and Figure 4-2. The observed volumes are equal in size (0.0457 x 0.0457 x 0.003 m^3) and are reaching over the full bed width [45]. Because of the restrictions of the used measurement method, just particles right next to the wall were tracked [45]. Therefore, the measurement depth was just about one particle diameter (d_s ~ 3 mm). The measurement sections will be referred to as volume 1 to volume 5 from left to right [45].

To support modelers, NETL was averaging the velocity in two different manners [45]. The data is available for Eulerian as well as for the Lagrangian approach. For the Eulerian particle statistics, the velocities of all particles inside the measurement volume are averaged [45]. These values were again averaged over time. For obtaining the averaged Lagrangian particle velocities, the velocities of all particles moving through the observed volumes were summed up and were used to create a velocity distribution over a specified period. Then the distribution was averaged [45,47]. The challenge providers (Gopalan et al. [45]) are stating: *"The calculated Lagrangian particle velocity was not in true sense a "Lagrangian"* i.e*., statistics obtained by following a single particle for a long period of time.*" The denotation was just used by the authors to prevent confusion with the first measurement method [45].

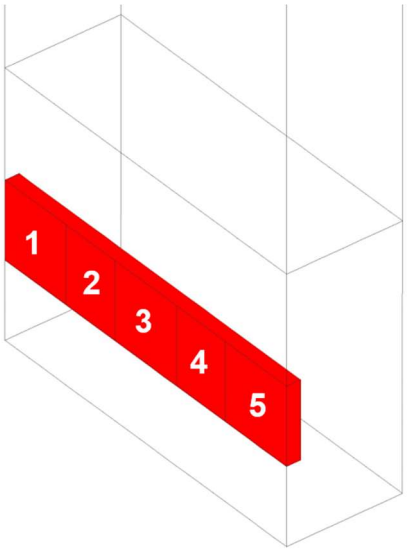

Figure 4-2: Measurement volumes.

The simulation results of Euler-Granular models were validated against the Eulerian particle velocity. A mass-averaged volume integral was used for velocity averaging. Simulations using DDPM were compared with the Lagrangian velocity statistics [45,47]. Velocities were averaged for at least ten seconds.

4.2.3 Granular temperature

Since the granular temperature is dependent on the instantaneous velocity components of the particles (compare chapter 3.4), the values for the granular temperature were collected for the same sections as for the particle velocity [45].
According to Gopalan and Shaffer [48], deriving of the granular temperature from experimental data should be done carefully. In their opinion, most measurement devices are not able to capture the individual particle velocities with the necessary precision, and the granular temperature is often derived from fluctuations of averaged particle velocities. However, by definition, the granular temperature describes the relative motion of particles at an averaged velocity [48,50,51]. Therefore, for comparing the granular temperature, it should be checked which velocities were used in the experiments and which in the calculations [47,52].

4.3 Models and settings

The goal was to find the strengths and weaknesses of each multiphase model. Furthermore, evaluations of associated sub-models were done. Since the NETL challenge I is a small-scale problem, all in chapter 2 introduced models were able to calculate the problem in an acceptable time [47].
The same mesh, the same initial particle mass and the same initial parcel amount (the parcel concept will be explained in chapter 4.3.1) were used for the different multiphase models. Common settings for all calculations, as well as the recommended settings, are introduced in chapter 4.3.1. The model variations are described in chapter 4.3.2.

4.3.1 Basic settings

Calculations were done in 2D and 3D. 2D models were used for first evaluations. Gravity was considered for all calculations. Each multiphase model was first set-up with recommended settings [12]. The realizable k-ε model with enhanced wall treatment was used as turbulence model. Because of the discrete character of the particles, the dispersed turbulence multiphase model was chosen. The influence of the used turbulence model is discussed in chapter 4.4.4.

Transient settings

In fluidized beds, the particle velocities and the pressure drop are statistically constant [1,2]. Instantaneous values can be strongly fluctuating from the mean value. The averaging should be long enough to overcome the influence of these oscillations (compare with chapter 4.4.1). Because of these reasons, all calculations were done in transient mode. Calculations lasted long enough to ensure stable fluidization (after about 2.5 seconds). Afterwards, the averaging of the values of interest was started and conducted for at least ten seconds [53].
For the particle tracking within the Lagrangian frame, very small time steps are needed [12,13,17]. For calculations, a time step of Δt = 0.001 s was chosen to ensure a low CFL number (according to Courant et al. [54]) for all cases. The CFL number is 0.438 for case III. For comparison, the simulations using the Euler Granular approach were executed with the same time step size. A DDPM-DEM calculation requires a still lower particle time step to resolve the particle collisions (details see chapter 3.5). The coefficient of restitution for the used particles was measured by Gopalan et al. [45] and is given as η = 0.84, and the spring-dashpot coefficient was estimated to K = 100 N/m using ANSYS® Fluent guidelines (compare with equations given in chapter 3.5). Following the guidance, the particle time step should be between $\Delta t_{p\,min}$ = 0.00002 s and $\Delta t_{p\,max}$ = 0.0002 s. The bigger step size $\Delta t_{p\,max}$ was chosen to keep the computational effort low. In Chapter 4.4.5 a variation of K, which leads to a smaller time step, is investigated [10,12,13].

Initial particle loading

The multiphase model set-up was done by using ANSYS® [10,12,13,17] recommendations. DDPM particles are clustered to parcels to reduce computational effort. These particle agglomerations are representing the properties of all the containing particles. ANSYS® recommends that the cell size should be sufficiently big enough for 5-10 parcels (considered with packing limit) when using DDPM calculations. Therefore, the choice of parcel diameter and amount is directly influencing the minimal cell size of the mesh (see chapter 4.3.2).

Inside Fluent, different definitions are available for the parcel calculation (standard parcels, parcels with const. diameter, parcels with const. mass). With these options, it can be ensured that the parcel size is small enough (compare with chapter 3.3). The particle size of d_s ~ 3 mm is already quite big. Hence, the parcel diameter was set to the particle diameter. In other words, every parcel is representing a single particle [10,13]. For inserting parcels, a tool called injection must be defined in Fluent. This tool feeds the flow field with a continuous parcel stream or with an initial number of parcels. In case of a fluidized bed, the best options are the volume injection and the file injection [13].
The volume injection option is a beta-feature (in ANSYS® Fluent Releases 17, 18.2, 19), which is filling a defined fluid zone with particles. The problem is that the particles are randomly inserted into the flow field. In areas near the wall or in denser regions particles can overlap – see Figure 4-3 (c). This overlapping can lead to a non-negligible mass defect. The error of the total initial solid inventory varied between 5-12 %. It was not possible to reproduce a flow field initialization with the same properties when using volume injection. When testing volume injections with different loads, the influence of initial mass defect was much higher than the influence of the used drag law. Therefore, the volume injection is not suitable for comparing drag laws with each other [12,13].

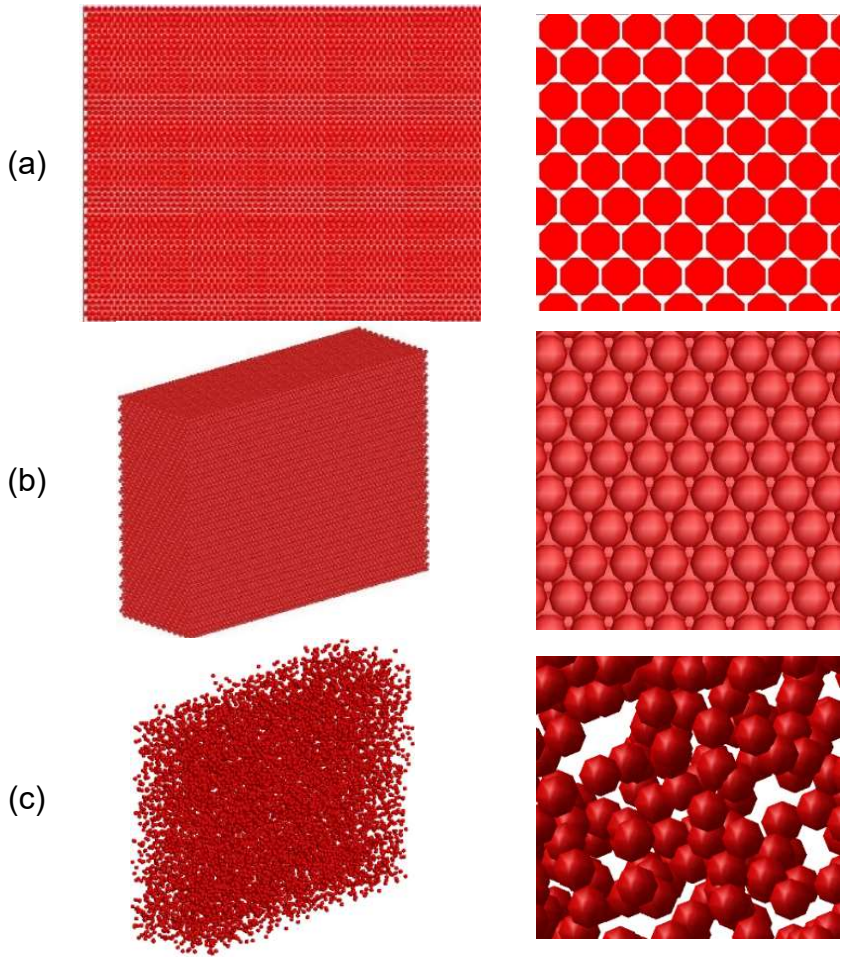

Figure 4-3: Initial particle loading for different injection methods (DDPM). (a) file injection 2D, (b) file injection 3D and (c) volume injection 3D.

Because of these reasons, the file injection was used for the following simulations. File injection uses a predefined file which contains all information about all parcels [13]. A script was developed which can create such an injection-file. It generates an injection-file for a predefined cuboid bed, with a defined packing limit for uniform sized spherical particles.

With this method, it was possible to create a reproducible initial particle loading. In Figure 4-3, the initial state of the static bed for different injection methods is shown. For 2D simulations, Fluent uses a virtual thickness of the flow field. The virtual thickness was set to one particle diameter. The corresponding number of parcels in that 2D slice is 4,060. For the Euler Granular model, no individual particle tracking exists. To set up the initial conditions of the particles, the volume fraction (α_i) of the solid phase is directly patched into the bed zone. Patching has to be done manually after flow field initialization, and before the start of the calculation Figure 4-4 shows the initial particle loading for an Euler Granular model. A summary of the initial particle loads can be found in Table 4-6 [12,13].

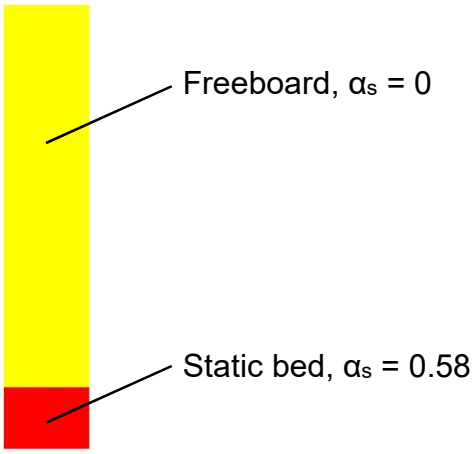

Figure 4-4: Initial particle volume fraction (-) for Euler Granular models.

Material properties

The fluidizing media used for the experiments was air. Standard air with the following modified values was used to conduct the simulations. The air density was calculated with the ideal gas law to ϱ_{air} = 1.204 kg/m^3, the dynamic viscosity was calculated by Sutherland´s law: μ_{air} = 1.821E-05 kg/(ms) [55]. For each case, the volumetric gas flow in standard liter per minutes (SLPM) was given. In ANSYS® Fluent, a mass-flow inlet boundary was used. The converted values can be found in Table 4-3 [52]. Data of single particles were provided by NETL. The particles are uniform in size and shape. The properties were already described in chapter 4.1. According to the ANSYS® guidelines, the particle time step was calculated to Δt_p = 0.0002 s (compare with chapter 4.3.1 and chapter 3.5) [12].

Table 4-5: Gas flow rates [47].

Case	Superficial gas velocity (m/s)	Volumetric gas flow (SLPM)	Mass flow rate (kg/s)
Case I	2.19	2,286.1	0.45458
Case II	3.28	3,429.1	0.06819
Case III	4.38	4,572.2	0.09092

4.3.2 Mesh and numerical settings

Discrete multiphase models have some specific requirements on the mesh. In contrast to a single-phase fluid simulation, a minimum cell size is necessary. According to ANSYS® recommendations, one cell should be large enough for 5-10 packed parcels [12]. In addition, it would be beneficial if the cells are similar in size and shape. The parcel diameter was set equal to the particle diameter [47].
Using the initial bed mass, the particle density, the packing limit ($\alpha_{s\,packed}$ = 0.63) and the guideline to have at least five parcels in a cell, the minimal necessary cell volume was calculated to $V_{cell,min}$ = 1.43E-07 m^3. Therewith, the minimal cell size length was estimated. The calculated minimal cell size would be about 0.005 m when using cubic mesh cells. To avoid being too close to this minimum requirement, the minimum cell length was set to 0.01 m. To ensure to have cells with about the same size and shape a hexahedron mesh was created. For this simple and rectangular shape, a mesh with 23x8x121 (WxDxH) cells was obtained (22,264 cells in total). Figure 4-5 shows a detail of the bed bottom [12,47,52].

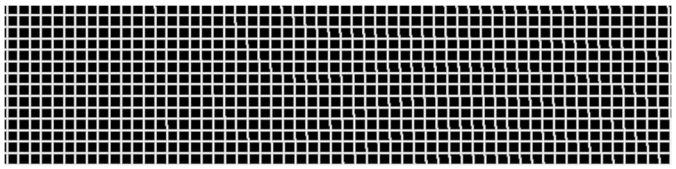

Figure 4-5: Hexahedron mesh used for simulation.

For the pressure-velocity coupling, the Phase Coupled SIMPLE option was set. As spatial discretization Green-Gauss Node Based is used for the gradient option. The momentum was solved with second-order upwind schemes. The transient formulation was a second order implicit discretization. Other values were solved with first order upwind discretization schemes to enhance convergence behavior [10,12,13,17].

4.3.3 Variations

The main task for the NETL I challenge was to compare the different available multiphase models in ANSYS® Fluent. For DDPM, both approaches for particle interaction treatments were used. Using the same basic settings (mesh, time steps), an Euler Granular model was set up.
Essential sub-models (drag law, granular viscosity) were varied for case I and validated with the experimental data. The most reliable settings were used to calculate cases II and III, to validate the results with each other. Afterwards, different investigations were executed. First, investigations on the turbulence model (see chapter 4.4.4) were done. For DEM, the most important parameters (restitution coefficient and spring-dashpot coefficient) were assessed (chapter 4.4.5). Moreover, studies for calculation accelerations were done (chapter 4.4.9). Besides these quantitative validations, the bubble formation behavior and preferred particle paths were qualitatively compared and classified by guidelines found in literature (chapter 4.4.2 and chapter 4.4.3).
Figure 4-6 shows an overview of all calculated variations. The columns are indicating the actual case and the multiphase model. The lines are categorizing the main settings and sub-models. In total, more than 73 simulations in about 55 variants were executed. Because of the high number of variations, just selected model combinations will be presented in the next chapters.

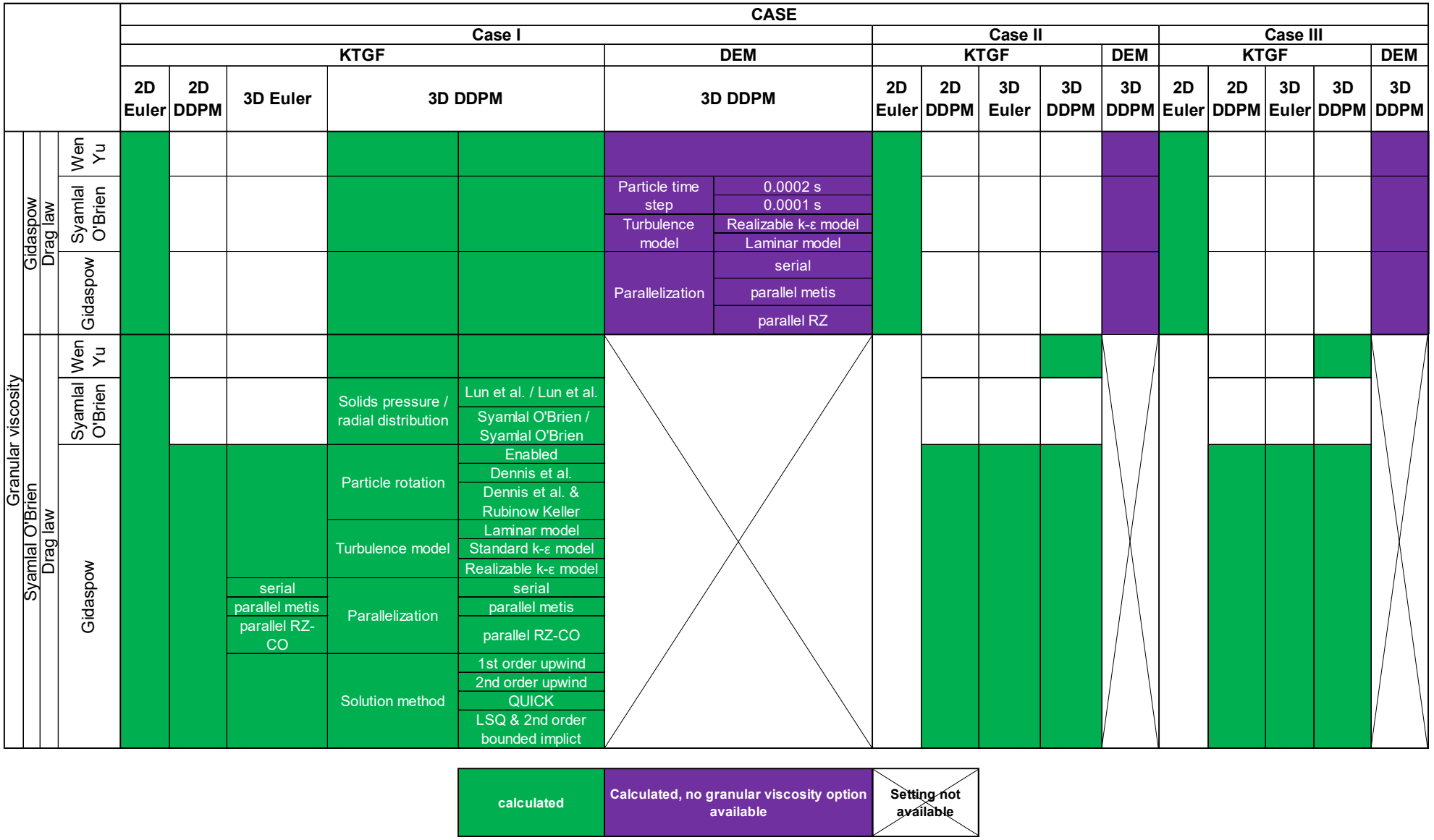

Figure 4-6: Overview of all calculated NETL-I variations.

4.4 Results

Table 4-6 shows a summary of the key parameters of spatial and temporal discretization, as well as the initial particle loading. Since the Euler Granular model offers no individual particle properties, the equivalent particle mass for the initial solid mass is given. The calculation times are also listed. On the bottom of the table, the calculation time per cell, per particle, per simulated time, as well as the calculation time for all of these values, can be found. These values are the average for all calculated cases. The calculation time is the total time including the time needed for creating reports, saving and plotting of the results. In chapter 4.4.9 more detailed investigations were done for a test case. As expected, the DDPM-DEM method is the most demanding one. Since all particle interactions are resolved with a low particle time step, the calculation takes significantly longer. DDPM-DEM was in average 4.4 times slower than DDPM-KTGF. That indicates that DEM is still too costly for industrial scale fluidized bed calculations (also see chapter 3.5 and chapter 4.4.9).

Table 4-6: Bed initialization and calculation times.

Dimension		2D		3D		
Model		Euler Granular	DDPM KTGF	Euler Granular	DDPM KTGF	DDPM DEM
Cell size	(m)	0.01	0.01	0.01	0.01	0.01
Cell amount	(-)	2,806	2,806	22,264	22,264	22,264
Particle number	(-)	-	4,060	-	93,285	93,285
Particle mass	(kg)	0.0827	0.0827	1.9	1.9	1.9
Fluid time step	(s)	0.001	0.001	0.001	0.001	0.001
Particle time step	(s)	-	-	-	-	0.0002
Simulated time	(s)	12.5	12.5	12.5	12.5	12.5
Calculation time	(h)	3-5	7-11	4-6	6-8	17-45
Calc. time/cell	(s)	5.13	11.55	0.81	1.13	5.01
Calc. time/parcel	(s)	3.55	7.98	0.19	0.27	1.2
Calc. time/real time	(min/s)	19.2	43.2	24	33.6	148.8
Calc. time/(cell, particle, real time)	(ms/s)	0.1	0.23	0.00097	0.00097	0.0043

3D simulations done with the Euler Granular model were about 1.4 times faster than the ones using the DDPM-KTGF models. The reason is the uniform particle size, which requires only one set of conservative equations for the solid phase. Although a DDPM-KTGF is not solving any conservative equation for the solid phase, it is calculating all particle tracks, which is slowing down the calculation, using the same grid and time step size. Therefore, the advantage of the DDPM does not come into effect for uniform particles (see chapter 3.3). However, for models, which should include a particle size distribution, the DDPM is the better choice (compare with chapter 5.1.3). In the following charts, the used multiphase model and the drag law were varied. If no further information of the used granular viscosity model is given, the granular viscosity model by Syamlal O'Brien was used (reference model).

4.4.1 Transient behavior

One possibility to define the minimum fluidization velocity is the pressure drop. If the fluidization velocity is increased until a constant pressure drop is obtained, the fluidized regime is reached (also see chapter 2.1 and chapter 2.3). As shown in Figure 4-7 the values are only statistically constant. A constant pressure drop (dashed red line) is only obtained when averaging over time. The instantaneous pressure drop over the bed is strongly fluctuating from the mean value, because of the highly transient mechanisms caused by bubble formation and turbulence. To obtain reliable results, first the calculations must run for a sufficient long time-span until full fluidization is reached and well established. Afterwards, averaging until the mean pressure drop is converged, is necessary [1,2]. Cloete et al. [53] suggest to simulate 20-times the period the gas needs to pass through the bed at superficial gas velocity, to ensure a pseudo-steady state and a meaningful time-averaging. For the NETL I challenge between 5.6 s (Case III) to 11.14 s (Case I) real time would be necessary (simulated real time in this work: 12.5 s).

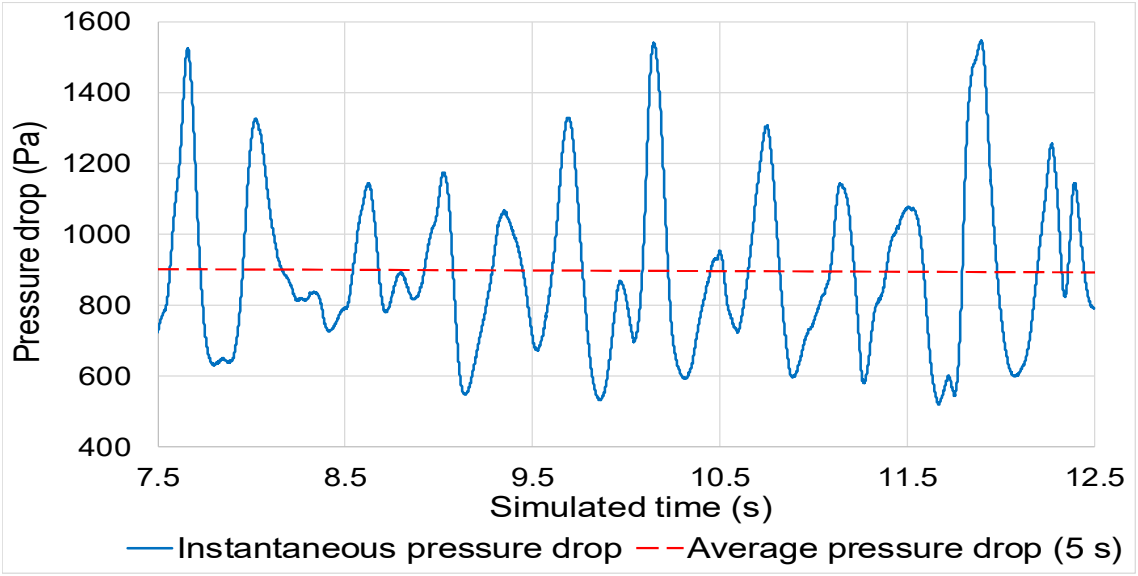

Figure 4-7: Pressure drop across the bed, DDPM-KTGF case I.

4.4.2 Gas and particle motion

The overall particle motion in the fluidized bed is not random. Depending on the diameter, density, size distribution, and shape of the particles different bubble and particle paths can arise. In addition, the superficial gas velocity and the expanded bed height to bed diameter/width ratio (also called bed aspect ratio) influences the bed behavior [1,2,56]. The characteristic particle flow for a circular bubbling fluidized bed with a porous plate distributor and Geldart B or D particles is presented in Figure 4-8 (a). In Figure 4-8 (b), the results from a DDPM-DEM simulation (case I) can be seen. The vector plot shows the average particle velocity magnitude (color and length of the vectors) in the symmetry plane. In the middle of the bed, the particles are moving upwards. During the uprising movement, the particles are turning towards the walls. Deflected there, the particle down-flow is then concentrated along the walls. Because of the particle circulation and the dense situation at the walls, 2D models are just hardly able to predict good quantitative results. Koralkar and Bose [36] are stating that, although the individual quantitative results are poor for 2D models, 2D is able generate reliable initial results. Since the computation time for 3D DDPM is much higher than for 2D models, it is worth first to estimate results with a 2D model.

(a) (b)

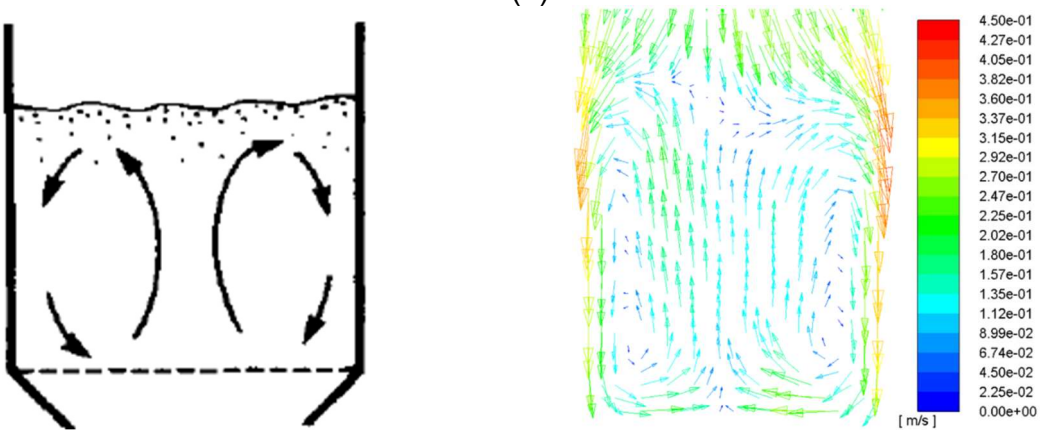

Figure 4-8: Solids movement in bubbling beds
(a) particle circulation for a bed with aspect ratio ~1 and high gas velocity [1],
*(b) vector plot of **average particle velocity magnitude (m/s)** - DDPM-DEM case I.*

The gas phase has a preferred ascending behavior. Figure 4-9 (a) shows the bubble and particle paths in a shallow circular bed as described by Kunii and Levenspiel [1]. Figure 4-9 (b) shows a contour plot of the averaged particle volume fraction in the bed (DDPM-DEM case I). Verdugo [56] investigated the preferential bubble paths and came to the following conclusions: gas bubbles at the bottom of the bed, where they are originating, are relatively evenly distributed over the full bed width. Therefore, the average volume fraction right above the distributor plate is relatively constant – green ellipse in Figure 4-9 (b). Above that, two symmetrical preferential bubble paths are formed. For wide and shallow beds, more parallel bubble paths can arise. The bubbles are moving to the bed center with increasing bed height. This area with high average gas volume fraction is indicated with blue arrows – see Figure 4-9 (b). The highest average gas phase concentration is at the meeting point of these two bubble paths, right below the upper bed surface. Bubbles of both paths are colliding there, and bigger bubbles develop through coalescence [1,2,56]. These pictures show that the gas and particle motion of circular fluidized beds is similar to the behavior of rectangular pseudo-2D-beds (better optical investigable).

(a) (b)

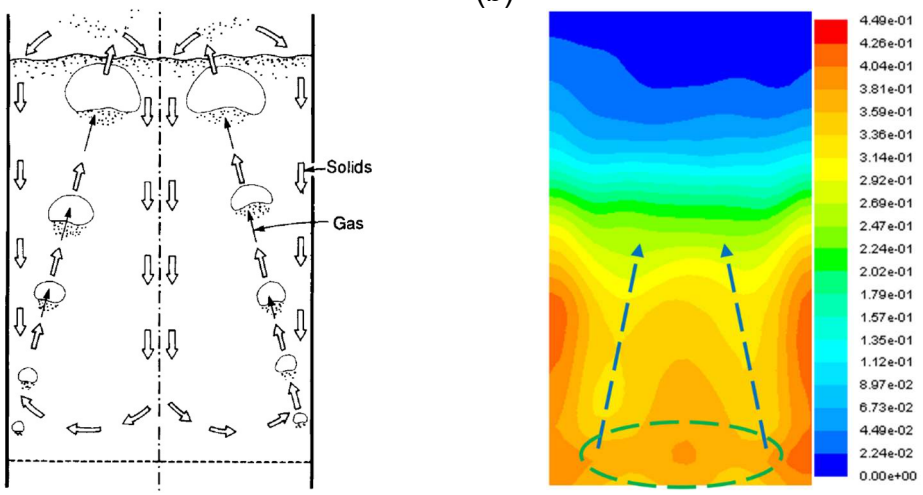

Figure 4-9: Bubbling bed behavior
(a) preferential particle and bubble paths [1],
*(b) **averaged particle volume fraction (-)** DDPM-DEM case I.*

4.4.3 Bubble formation

Since the NETL I is using Geldart D particles, bubbling behavior can be expected in the bed [1,5,47]. With increasing superficial gas velocity, the bubbling bed turns into a slug flow. At the bed bottom, small bubbles are formed [56]. During ascending, the bubbles are growing because of coalescence effects, so fewer but bigger bubbles can be found with increasing bed height. At the upper bed surface, the bubbles are released into the freeboard [2,56].
Bubbling forming behavior was investigated in detail by Agrawal et al. [57]. Using a DEM model and using different drag laws, they were calculating two different bubbling beds. Their research led to the conclusion that the prediction of the bubble formation is primarily influenced by the drag law. When using the drag laws by Syamlal O'Brien or Gidaspow for 1.25 times the minimum fluidization velocity U_{mf}, no bubbles were formed.
With increasing velocity (at around two times U_{mf}), these drag laws were qualitatively reproducing the bubble behavior. In the NETL I challenge the lowest gas velocity is about two times U_{mf}. According to Agrawal's [57] work, the predictions should be adequate enough for a qualitative analysis [57].
The DDPM-DEM model is able to predict the real bubble behavior. The series of contour plots in Figure 4-10 shows the current gas volume fraction in the bed for case I (about two times the minimum fluidization velocity). The bed is already recognizably expanded, and the upper bed surface has a continuous, well-defined border to the free flow field.

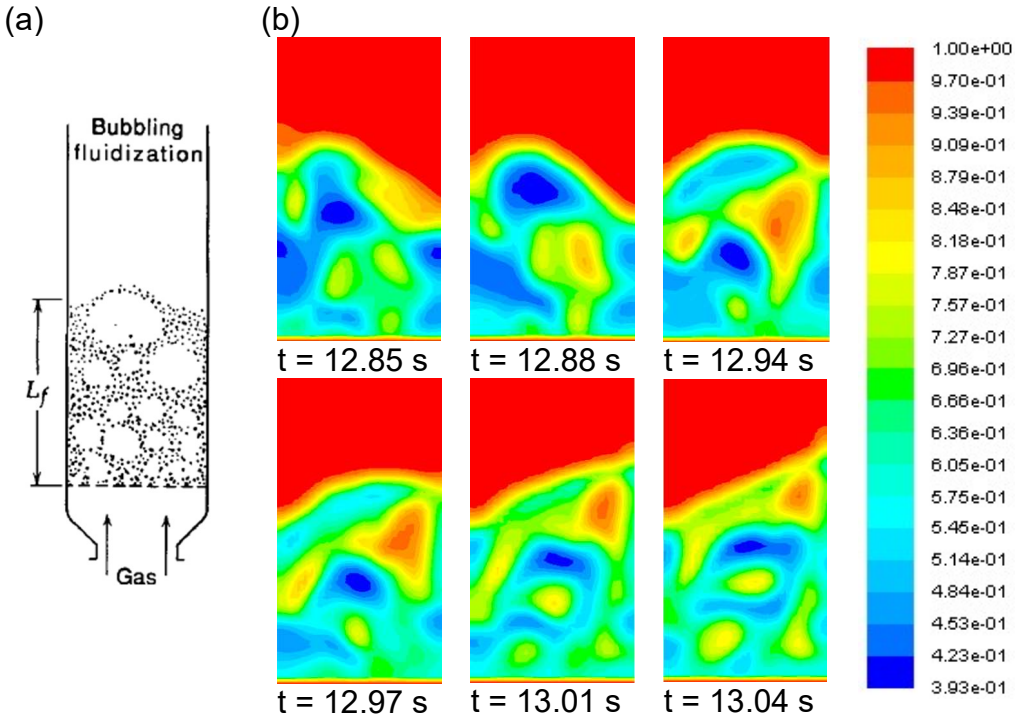

Figure 4-10: Bubble forming case I,
(a) bubbling fluidization [1], (b) DDPM-DEM contour plots of ***gas volume fraction (-)*** *in symmetry plane for different time steps*

With increasing superficial gas velocity (case II), the bubbles are getting significantly bigger at the top of the bed (see Figure 4-11). In literature, this behavior is called slug flow or slugging. Bubbles near to the top are reaching over the full bed width. The fluidized bed is expanded largely. Due to the slug break up which throws solids into the freeboard, the upper bed surface is not smooth anymore [1,2]. Lungu et al. [58]) are classifying case II already into a transition region between slugging and turbulent fluidization (compare with FB classifications in Figure 2-1). The obtained bed expansion is, qualitative compared, very similar to the results of the DEM modelers Elghannay and Tafti [59].

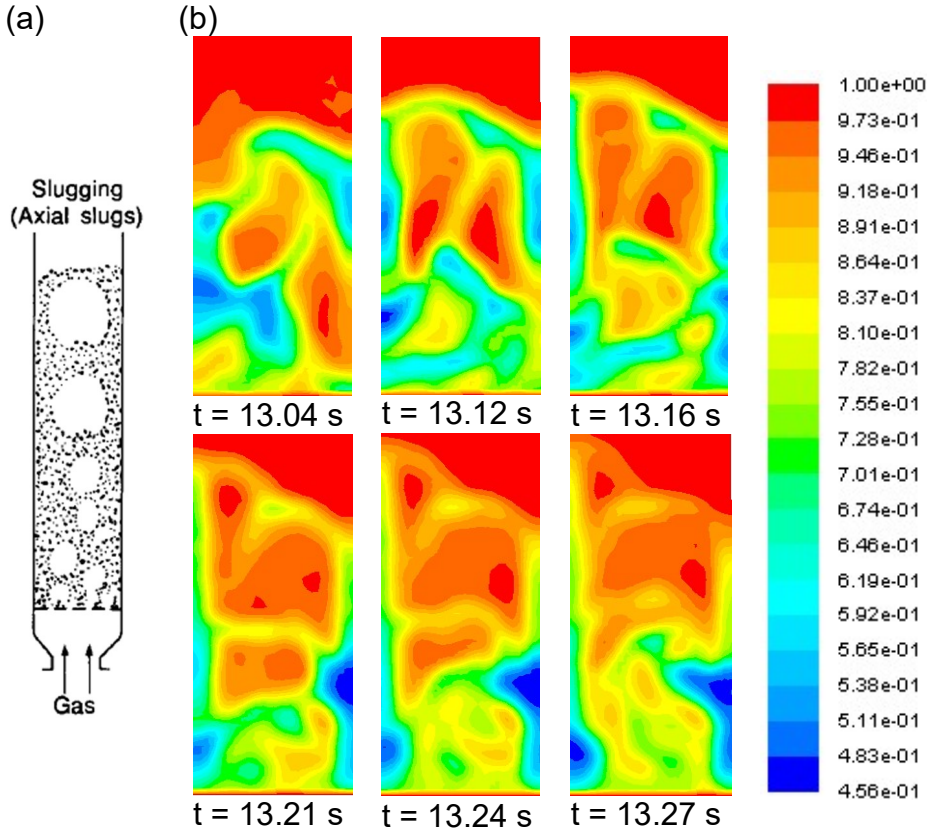

Figure 4-11: Bubble forming case II,
*(a) slug flow [1], (b) DDPM-DEM contour plots of **gas volume fraction (-)** in symmetry plane for different time steps*

With a further increase of the gas velocity (case III), some gas bubbles are reaching over the full bed height. The fourth contour plot in Figure 4-12 shows a temporary gas stream reaching from the bottom of the bed up to the top. This stream should not be confused with a standing jet, which can occur when using single orifices gas distributors. The bubbling flow cannot be clearly defined; its bubble appearance is a mix of slug flow, wall slugs, and flat slugs. The big bursting slugs are entraining many particles to the freeboard, so the fluffed bed height is strongly fluctuating. Therefore, no clearly defined upper bed surface exists [1]. The slugging behavior is caused by stretching of bubbles due the high gas velocity is similarly described by Ayeni et al. [60].

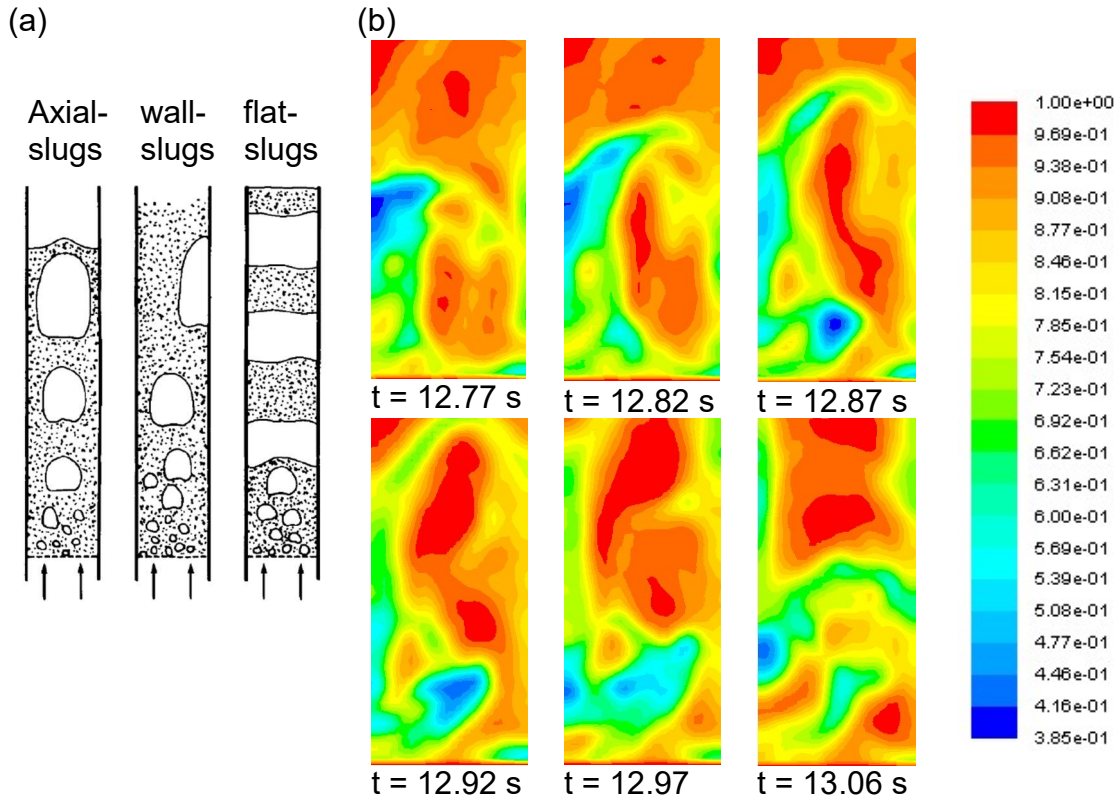

Figure 4-12: Bubble forming case III,
(a) *slug flow [1], (b) DDPM-DEM contour plots of* ***gas volume fraction (-)*** *in symmetry plane for different time steps*

4.4.4 Turbulence model

The Reynolds number is for every case in the turbulent region. Consequently, the need for a turbulence model was assumed. The Reynolds numbers for the whole bed (cross-sectional area of the bed and the superficial gas velocity) as well as for a single particle are summed up in Table 4-7. For the simulations, the Realizable k-ε model was used. The enhanced wall treatment was used for the near wall region. The dispersed multiphase model was chosen to account for the discrete phase [10,13].

Table 4-7: Reynolds number for full bed section.

	Reynolds number for the whole bed (-)	Reynolds number for a single particle (-)
Case I	16,650	480
Case II	25,000	720
Case III	33,300	960

There were several reasons for determining the influence of the turbulence. First, it is necessary to evaluate if there is a significant influence of turbulence on the particles, or if the particle motion and behavior is primarily defined by the collisional interactions and the drag. Another reason is to find the effects on the continuous phase itself. For future projects, which include also chemical reactions (see chapter 1.2), the fluid behavior is of big interest. NETL provided no data about the continuous phase. Therefore, just the simulation results were compared, without validation to experimental results [47].

In literature, different opinions about turbulence modeling in fluidized beds exist. Some authors claim that the turbulence influence is low compared to the influence of particle collisions (for DDPM models of FB's). For example, Li and Dietiker [61] state that, if the primary concern is about the particle motion, the turbulence model can be neglected. Lungu et al. [58] asserted that for the NETL I challenge the turbulence model is not affecting the results very much. On that account, they were using a laminar model to speed up calculations. Other modelers used an LES (Kraft [3] and Panday et al. [44]) approach, the Standard k-ε model and the RNG k-ε model (Panday et al. [44]).
In the following, a Realizable k-ε model is compared with a laminar approach. For comparison case III (highest superficial gas velocity and therefore highest Reynolds number) were chosen. A DDPM-DEM model was used for comparison [62,63].
As shown in Figure 4-13 and Figure 4-14, the effect of the turbulence model on the mean particle velocities is just marginal. Both approaches are yielding very similar results inside the bed. Next to the wall, the deviation between the models is slightly higher but still acceptable.

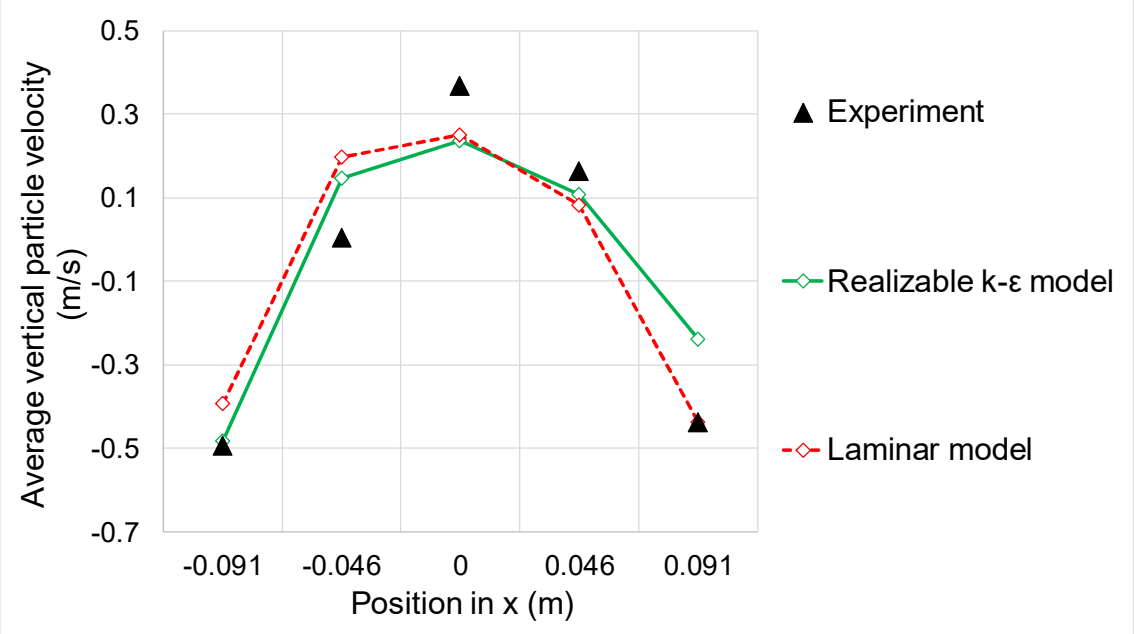

Figure 4-13: Averaged vertical particle velocity, case III.

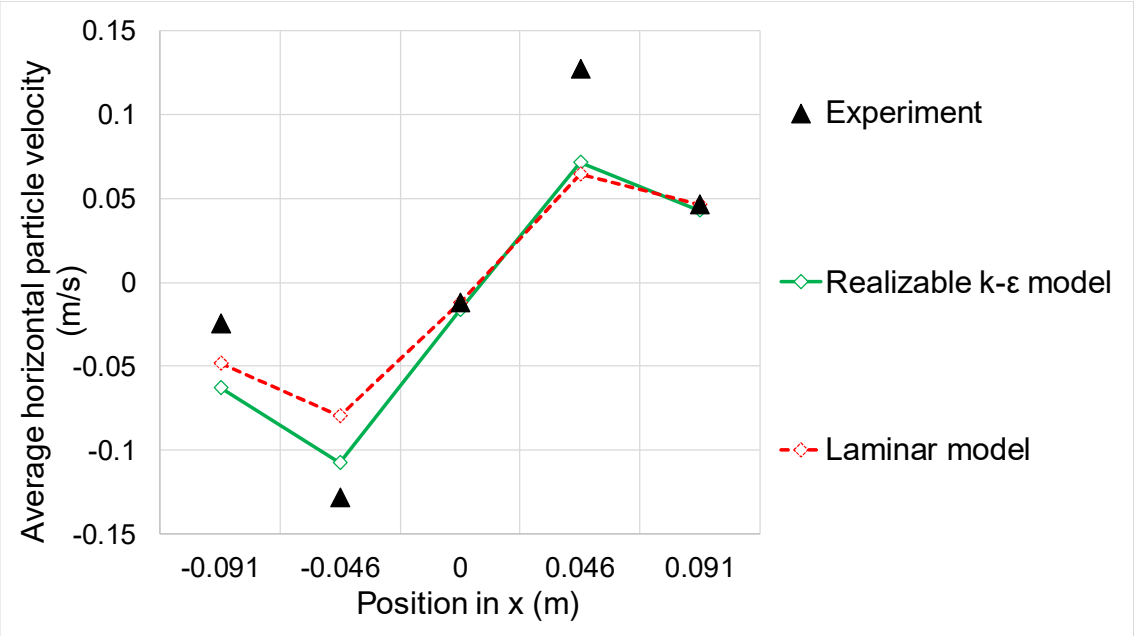

Figure 4-14: Averaged horizontal particle velocity, case III.

When analyzing the fluid flow in the primary flow direction, no significant deviations between the models were recognizable (Figure 4-15). The laminar model is predicting higher values for the vertical fluid velocity. This can be explained with the different handling of the near wall region (for the realizable k-ε model an enhanced wall treatment was used) [64]. However, the qualitative trend is the same for both approaches.

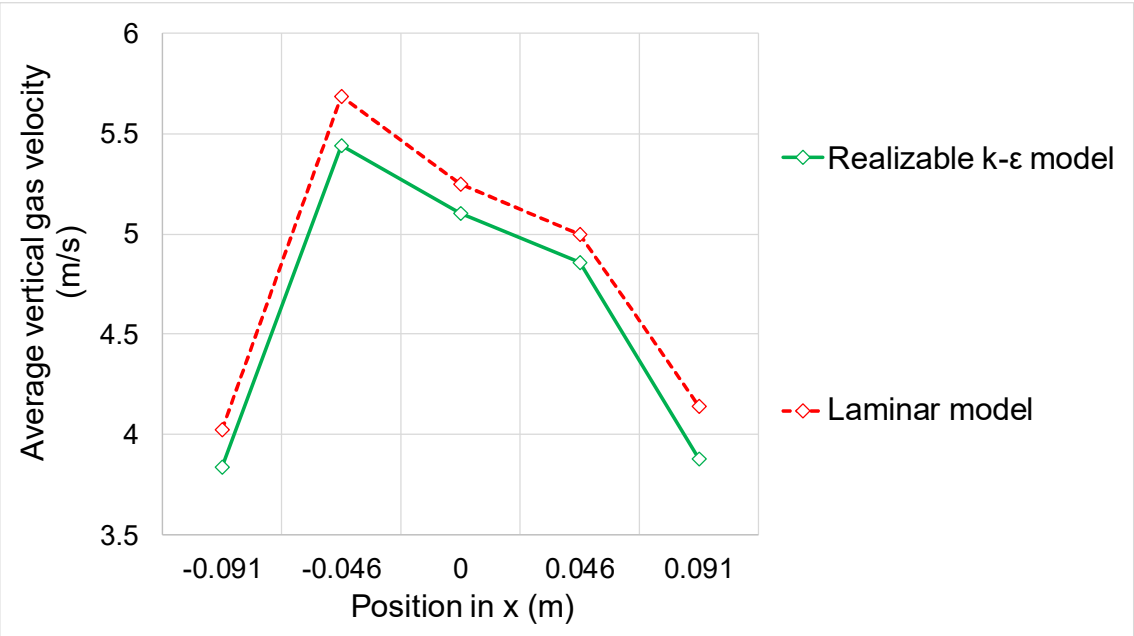

Figure 4-15: Averaged vertical fluid velocity, case III.

The deviation for the horizontal fluid velocity component is higher (Figure 4-16). Since a laminar approach is not considering the turbulent eddies, it is not surprising that the horizontal velocity profile of the fluid is less distinctive for the laminar calculation. Because less of the fluid is transported in the horizontal direction without the turbulent eddies. The realizable k-ε model is considering the swirls in the continuous phase. Therefore, higher horizontal fluid velocities are observed.

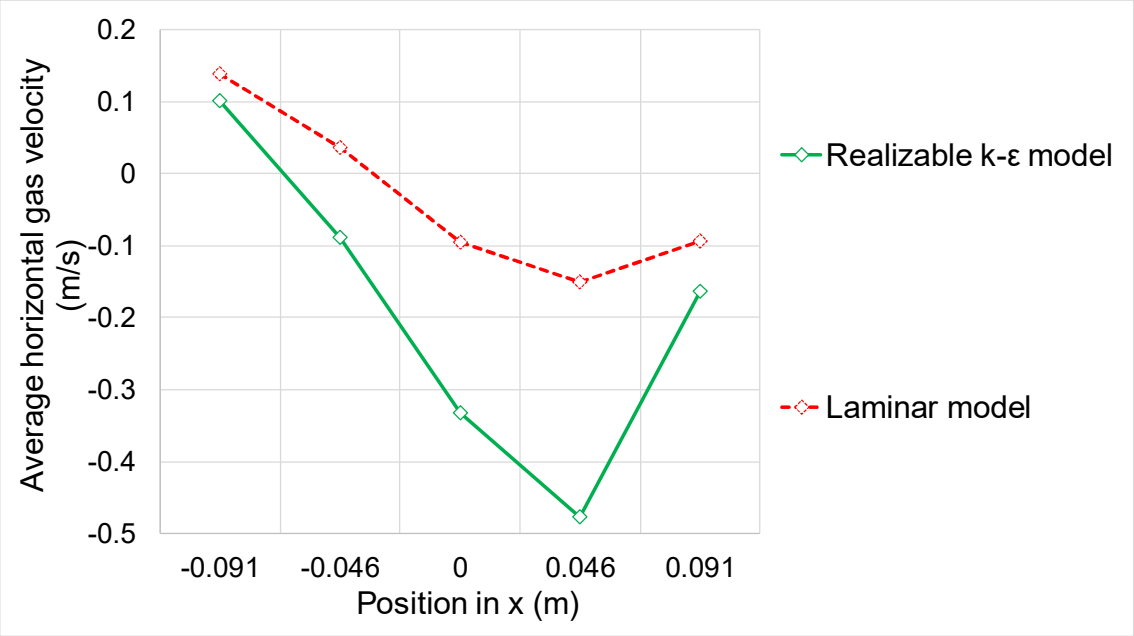

Figure 4-16: Averaged horizontal fluid velocity, case III.

As stated by Li and Dietiker [61] and Lungu and Wang [58], the influence of the turbulence model on the discrete phase can be neglected for small-scale problems. Or in other words, the particle behavior was not influenced by the turbulence model. However, for the fluid flow pattern itself, the choice of the turbulence model can indeed affect the results in a significant way (Figure 4-16). Especially the reaction rate is strongly influenced by gas velocity, gas residence time, turbulent mixing and the eddy dissipation. Furthermore, some reaction models require a turbulence model. For example the EDC model (eddy dissipation concept model) needs k and ε [10]. Therefore, a turbulence model is mandatory for reactive fluidized bed simulations.

4.4.5 DEM settings

For the DEM approach, the particle interaction force is calculated by the particle deformation (also compare with chapter 3.5 and chapter 4.3.1). To be able to obtain the deformation, a small time step is needed. This so-called particle time step is significantly influencing the necessary calculation time. For estimating the particle time step, ANSYS® provides recommendations. The calculation of the necessary particle time step size is explained in chapter 3.5. Simulations were calculated using a particle time step of Δt_p = 0.0002 s. The fluid time step was Δt = 0.001 s. Using a spring-dashpot coefficient of K = 100 N/m, the ANSYS® recommendation for the particle time step is between $\Delta t_{p\,min}$ = 0.00002 s and $\Delta t_{p\,max}$ = 0.0002 s. Therefore, the chosen particle time step was already the maximum recommended one.

The influence of the time step was investigated for determining the potential of result improvements. The spring-dashpot coefficient was tripled to K = 300 N/m (valid range for K is 100 – 1000 N/m [12]). This resulted in a recommended particle time step range of $\Delta t_{p\,min}$ = 0.00001 s to $\Delta t_{p\,max}$ = 0.00012 s. A step size of Δt_p = 0.0001 s was chosen. Since the calculations took already a long time, the time step was not reduced any further [12,13].
In Figure 4-17, the results with a time step of Δt_p = 0.0001 s are confronted with a time step of Δt_p = 0.0002 s. The halving of the particle time step resulted in a nearly doubled calculation time. Calculation with Δt_p = 0.0002 s needed about 18 h for simulating 12.5 s. With Δt_p = 0.0001 s the calculation lasted already for 34 h. Hence the accuracy of the particle velocity is not changing much, it is not necessary for the NETL I challenge to use a lower time step.

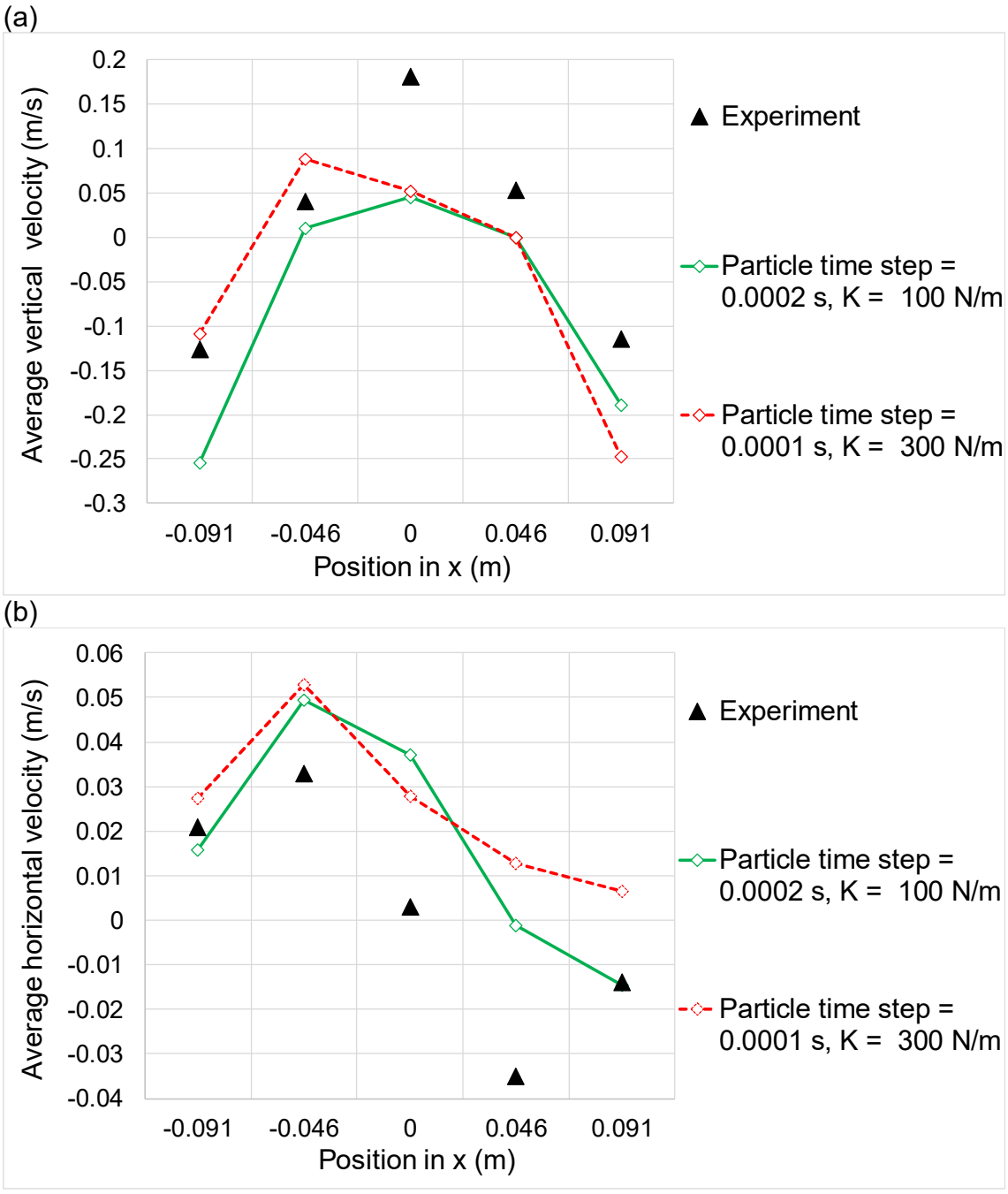

Figure 4-17: Influence of DEM settings,

(a) average vertical fluid velocity, (b) average horizontal fluid velocity.

4.4.6 Granular temperature

For Euler Granular KTGF and DDPM-KTGF simulations, the granular temperature is one of the most important variables. It is required for the calculation of the kinetic and collisional stress (see chapter 3.4). The granular temperature is dependent on the accuracy of the particle velocity components. As mentioned in chapter 4.2, there are often confusions in obtaining and comparing the granular temperature with experiments. The granular temperatures presented in the following charts are the values calculated in ANSYS ® Fluent (including all particle velocity components).
NETL just measured the horizontal (x-direction) and the vertical (y-direction) particle velocity and also used these components for calculation of the granular temperature. The particle velocity component in y-direction was not included in their considerations. Therefore, the calculation basis of the compared values is not the same. The calculation results were not transformed because the necessary relative motion of the particles was not captured during the simulation [45]. Because of these reasons, the influence of the third velocity component was ignored, and the in ANSYS® Fluent calculated value was directly taken for comparison [10,48,50,51].
Figure 4-18 shows the granular temperature for case I. The qualitative trend of the granular temperature is not well captured. The Euler Granular model shows under-prediction for every measurement volume.

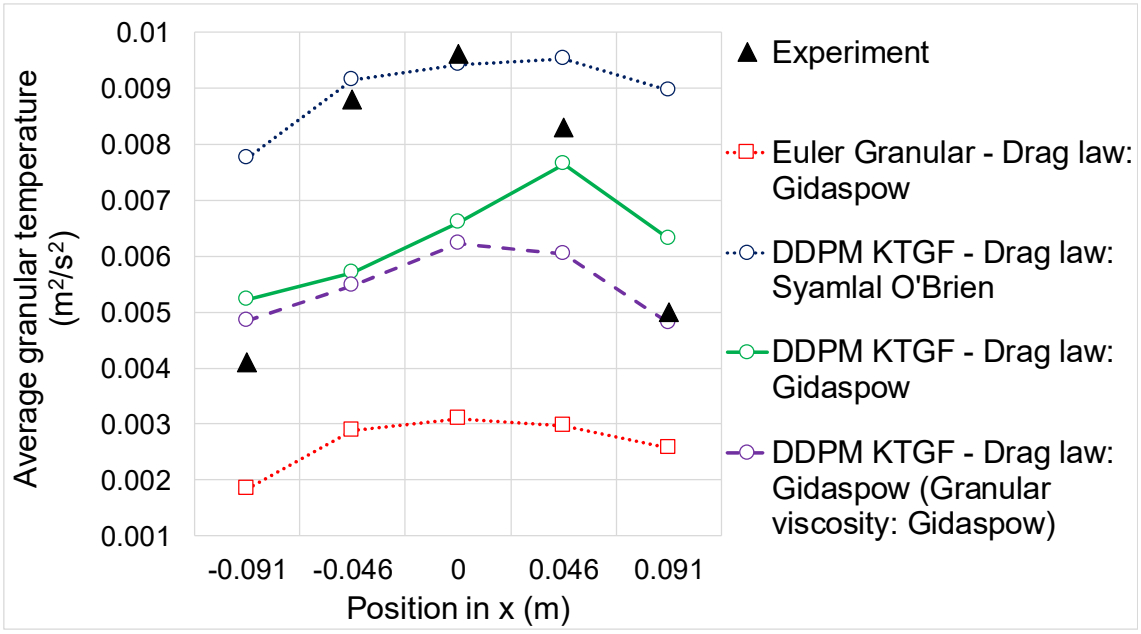

Figure 4-18: Averaged granular temperature, case I.

In Figure 4-19 and Figure 4-20, which are representing case II and case III, similar behavior is shown. The deviations to the experimental results are fluctuating between 1 – 55 %. For the higher superficial gas velocities (especially for case II), no significant differences between the KTGF models exist. All results are yielding similar trends and values. There are several reasons for the discrepancy to the experiments. If the accuracy for the particle velocity components is low, also the accuracy of the granular temperature is going down. Another issue is that the granular temperature was just calculated by using an algebraic approach. Another possibility (for the DDPM calculations) is the DPM averaged granular temperature model. Alternatively, also an own transport equation could be solved (compare with chapter 3.4.1) [10,13,65]. Just a few authors published results for granular temperature. Lungu et al. [58], were providing data for case I. Their results are around in the same magnitude as the ones obtained in this work. Agrawal et al. [57] were providing detailed data for every case with different drag laws. However, most of their results were over-predicting the granular temperature by orders of magnitude. They are reporting a scattering of the results between 1 – 517 %. The reasons are unknown, however, it is to say that they were solely using DEM, which is not requiring the granular temperature concept [57,58].

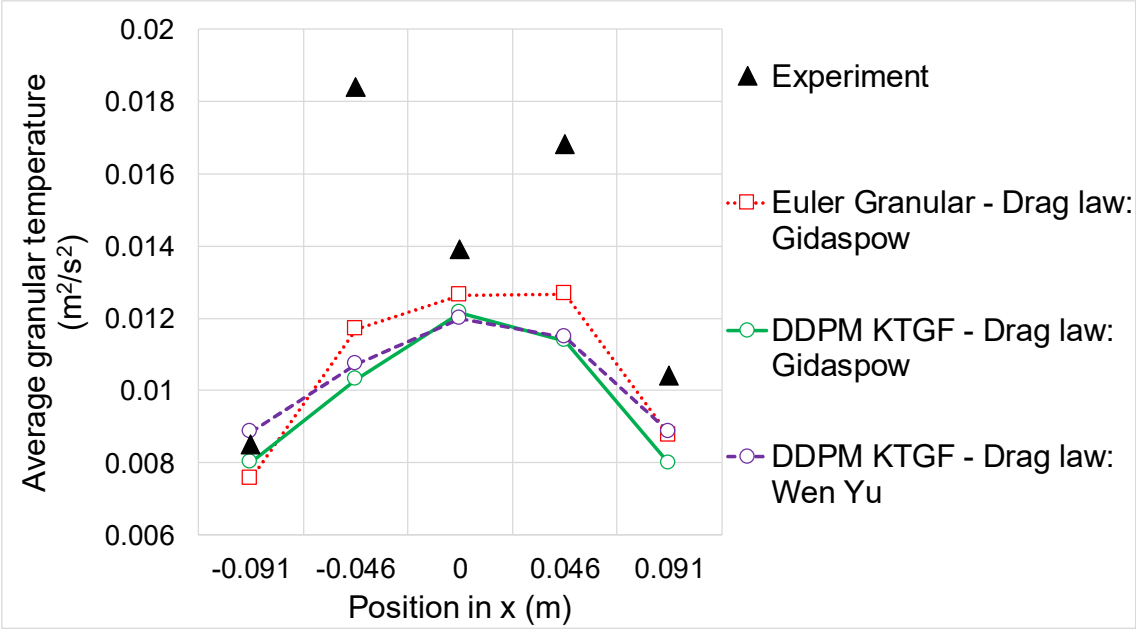

Figure 4-19: Averaged granular temperature, case II.

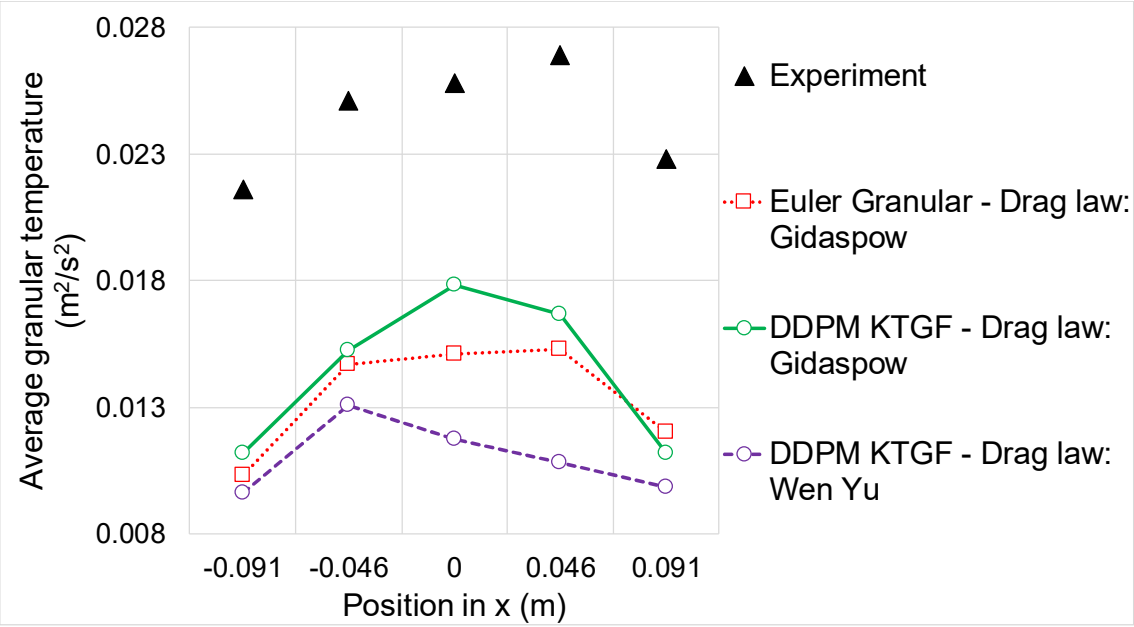

Figure 4-20: Averaged granular temperature, case III.

4.4.7 Particle velocity

In chapter 4.2, the measurement methods for the particle velocity and the handling of the experimental data are explained. The measurement volumes 2, 3 and 4 will be referred to as inner bed region. The measurement volumes 1 and 5 will be called near wall regions.

Case I

In Figure 4-21, the vertical particle velocity is shown for the different model variations. The DEM models were yielding the best results. Furthermore, the DEM models were the only ones able to represent the qualitative trend of the vertical particle velocity over the full bed width.
KTGF models were not able to reproduce the trend of the vertical particle velocity profile (Figure 4-21). Especially in the denser regions (center of the bed and wall regions – also compare chapter 4.4.2), the deviation is quite high. In contrast to that, in areas without preferred particle paths (measurement volumes 2 and 4, also see chapter 4.4.2) the predictions are well fitting. Furthermore, the different multiphase and drag model combinations were yielding similar results for these measurement volumes. A direct comparison between the Euler Granular KTGF and the DDPM-KTGF approach shows no significant differences.

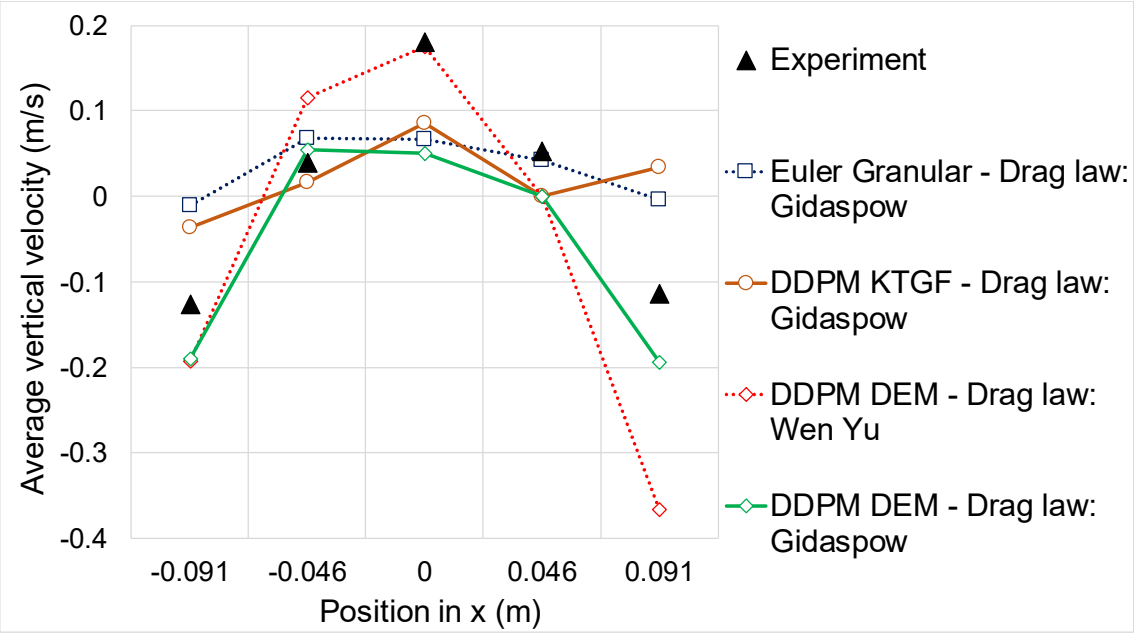

Figure 4-21: Averaged vertical particle velocity, case I.

Regarding the horizontal particle velocity, most models were not able to qualitatively reproduce the experimental data for case I (Figure 4-22). The chart shows a preferred direction for the horizontal velocity component in the measurement volumes next to the wall.

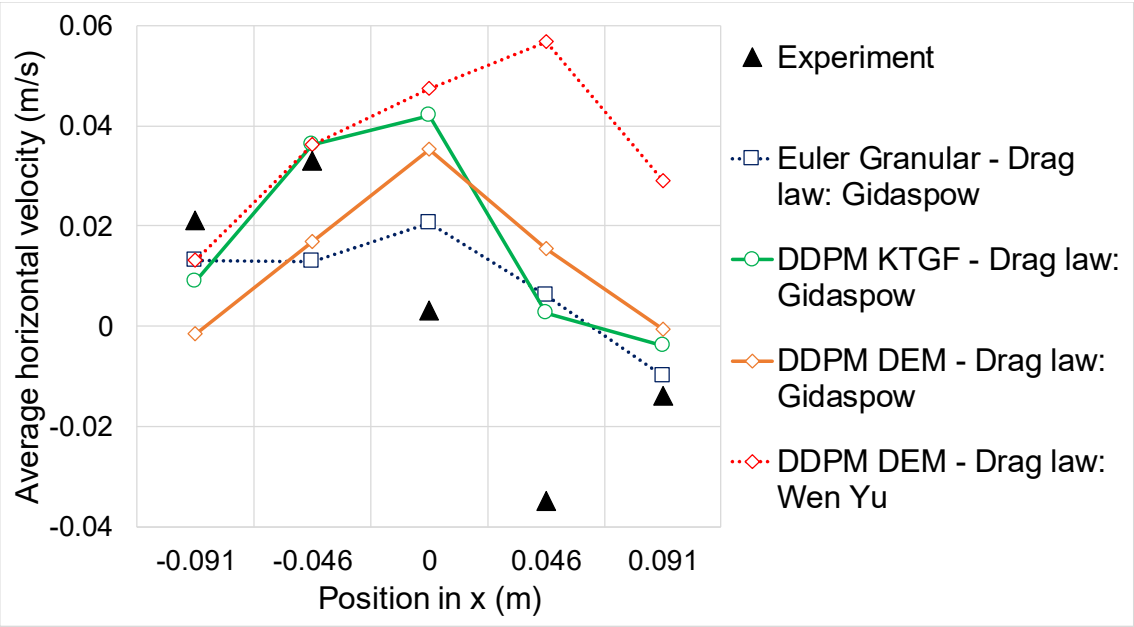

Figure 4-22: Averaged horizontal particle velocity, case I.

Case II

For increasing superficial gas velocities, the predictions of the vertical velocity with the KTGF models improved but were still unsatisfying (Figure 4-23). However, results for the horizontal particle velocity were not improving (Figure 4-23Figure 4-24). The best model is again the DEM approach in combination with the drag law derived by Gidaspow.

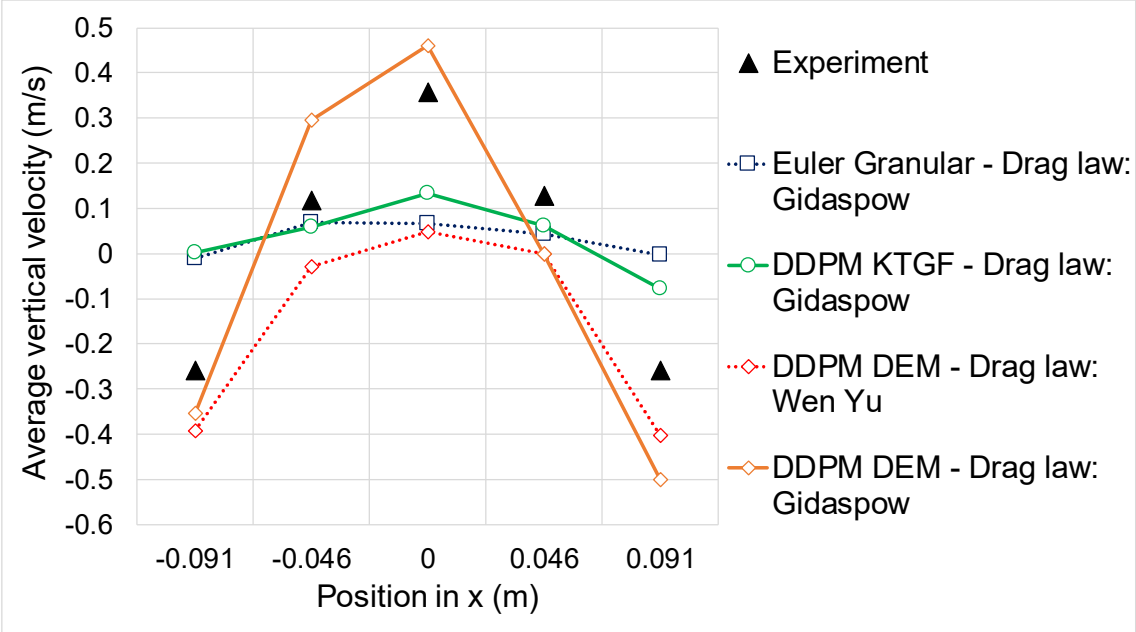

Figure 4-23: Averaged vertical particle velocity, case II.

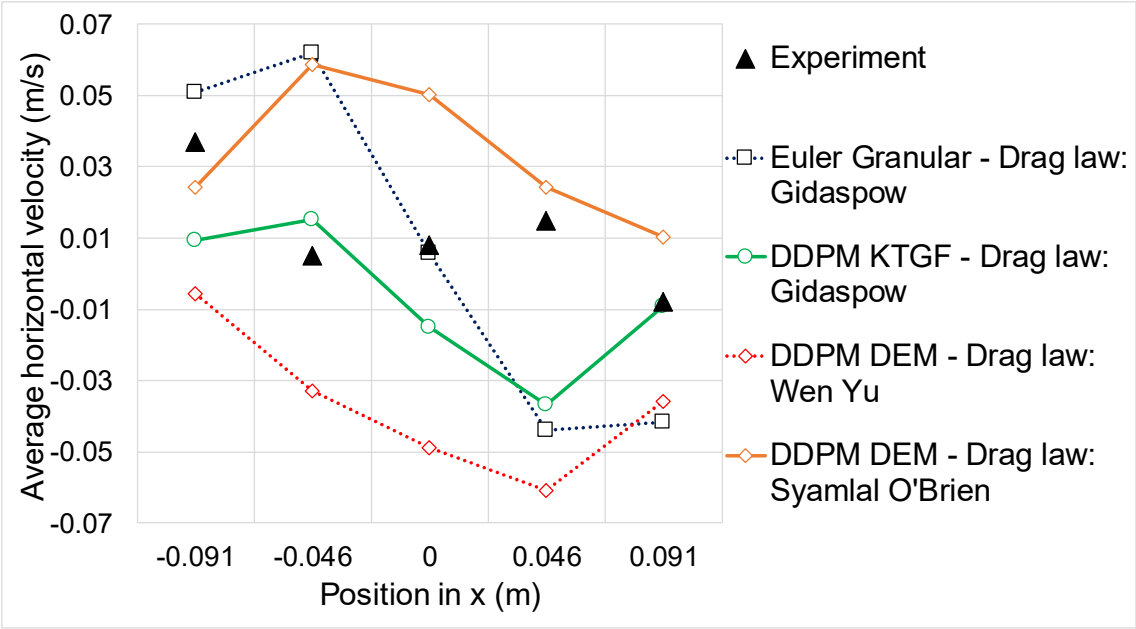

Figure 4-24: Averaged horizontal particle velocity, case II.

Case III

The best model for case III was DDPM-DEM in combination with Gidaspow drag law (Figure 4-25). The predictions for the horizontal particle velocity were significantly better for case III (Figure 4-26).

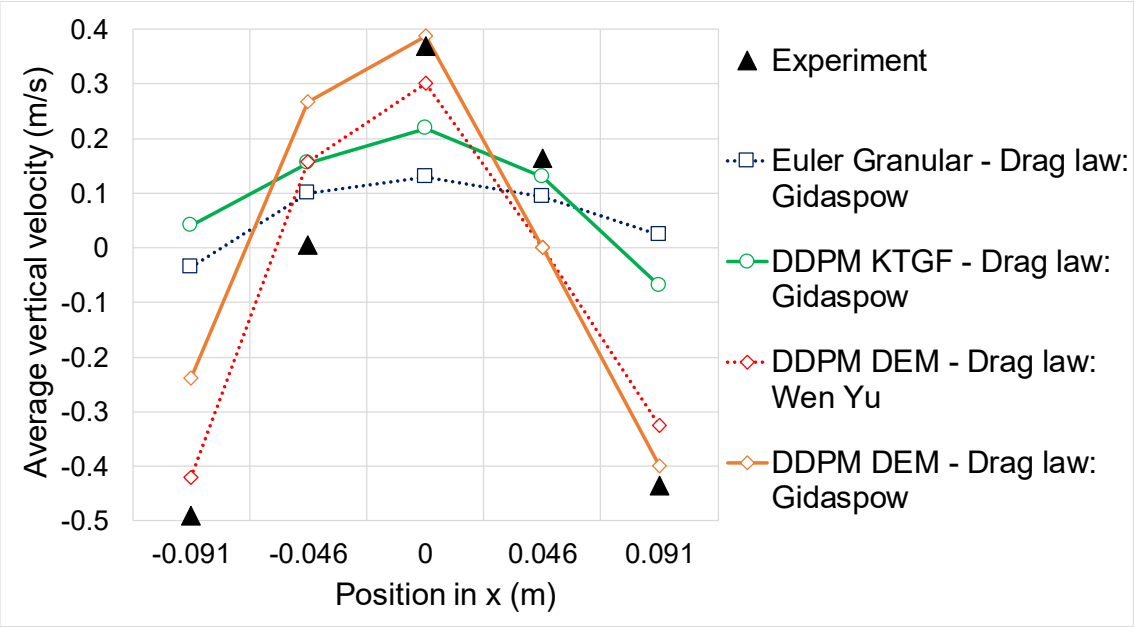

Figure 4-25: Averaged vertical particle velocity, case III.

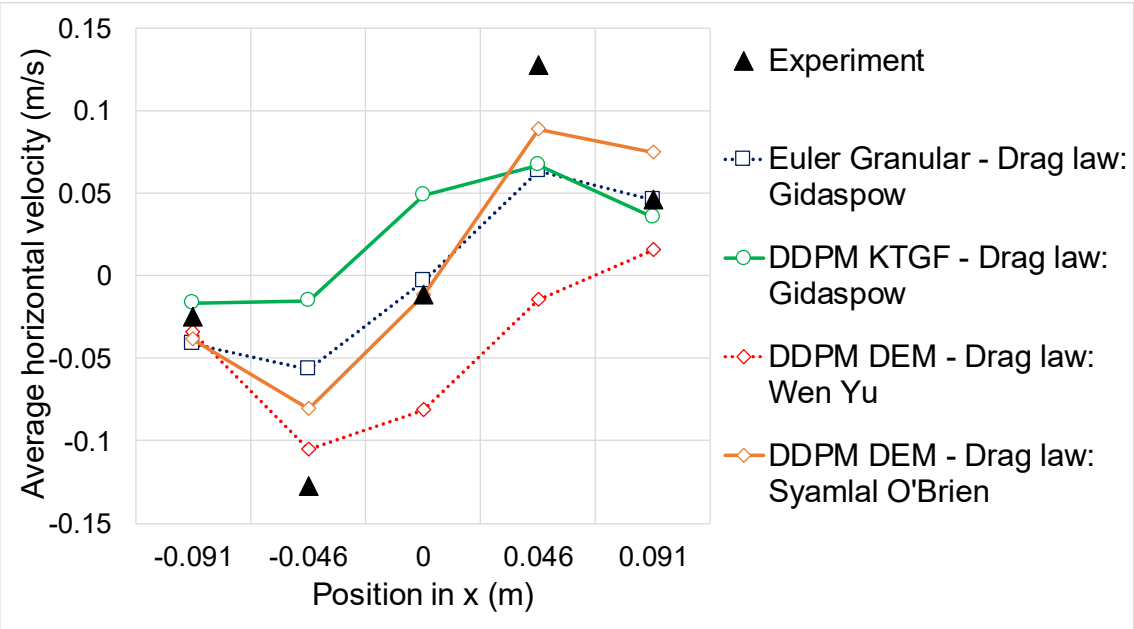

Figure 4-26: Averaged horizontal particle velocity, case III.

The DEM models were yielding the best results. KTGF models were not able to reproduce the trend of the vertical particle velocity profile. Especially in the denser regions (center of the bed and wall regions), the deviation is quite high. A direct comparison between the Euler Granular KTGF and the DDPM-KTGF approach showed no significant differences in the velocity profile. Regarding the horizontal particle velocity, no model was reproducing the trend of the experimental data for case I and case II. However, for case III the results improved significantly.
In areas with denser particle packing more particle collisions can be expected, which were not correctly resolved by the KTGF approximation. Another reason is the observed measurement volume itself. Because of the restrictions of the HsPIV measurement, the averaged velocity data is just provided for a depth of about one particle diameter from the wall. However, for the DDPM models, a cell size of 0.01 m was chosen, which is about three times the particle diameter. Since the KTGF is averaging the interactions for the cell, the error for one single cell can be quite high. Smoothing algorithms are suggested in literature [66] (e.g., by considering the neighbor cells), to overcome this issue. Furthermore, a simple mesh without inflation layers was used. According to Ozarkar et al. [67], inflation layers are improving the accuracy of the particle down-flow next to the wall.
The vertical velocity profiles obtained by the Euler Granular modelers Tandon and Karnik [65] as well as by Lungu et al. [58] were in good agreement with the experiments. They were using the solid phase wall boundary condition derived by Johnson and Jackson (see chapter 3.7) [29]. In the Johnson and Jackson [29] approach a specularity coefficient φ is describing the momentum transfer between wall and particles during collisions. They were also investigating the influence of the specularity coefficient. Lungu et al. are recommending a specularity coefficient of $\varphi = 0.5$ for low superficial gas velocity (case I) and a $\varphi = 0.05$ for higher superficial gas velocities (case II and case III). The discrepancy of the results obtained in this work can be explained with the lack of a model, which is modeling the particle wall interactions (collisions, slip and friction) [29,58,65].
Other modelers (Ayeni et al. [60], Koralkar and Bose [36]) were also reporting good qualitative results with DEM. Agrawal et al. [57] were using Syamlal O'Brien and Gidaspow among other drag laws in combination with a DEM approach. They are also reporting deviations in around the same magnitude. Other DEM modelers (Koralkar and Bose [36]) experienced a wide scattering of results, especially for the horizontal velocity.

4.4.8 Pressure drop

One of the most important parameters of fluidized beds is the pressure drop across the bed. Figure 4-27 shows the average pressure drop for selected model settings. The pressure drop was reported between the bed heights $z = 0.0413$ m and $z = 0.3461$ m. Tested drag laws were: Wen-Yu, Gidaspow, and Syamlal O'Brien. Noticeable is that the pressure drop for every multiphase model, drag law and granular viscosity model is over-predicted. The DDPM-DEM models yielded the best results (deviation 17 - 20%). Especially the results obtained with the drag laws by Syamlal O'Brien and Gidaspow are in good agreement with the measurements. In addition, the DEM prediction got better with higher gas velocity (except for the Wen-Yu drag law). The KTGF models predicted the qualitative trend of the pressure drop well. However, for case III the absolute deviation was high (about 60% for the Euler Granular model and 55% DDPM-KTGF). Multiphase models with Gidaspow's drag law were the best variant for pressure drop calculation. However, the best result had still an over-prediction of about 16%.

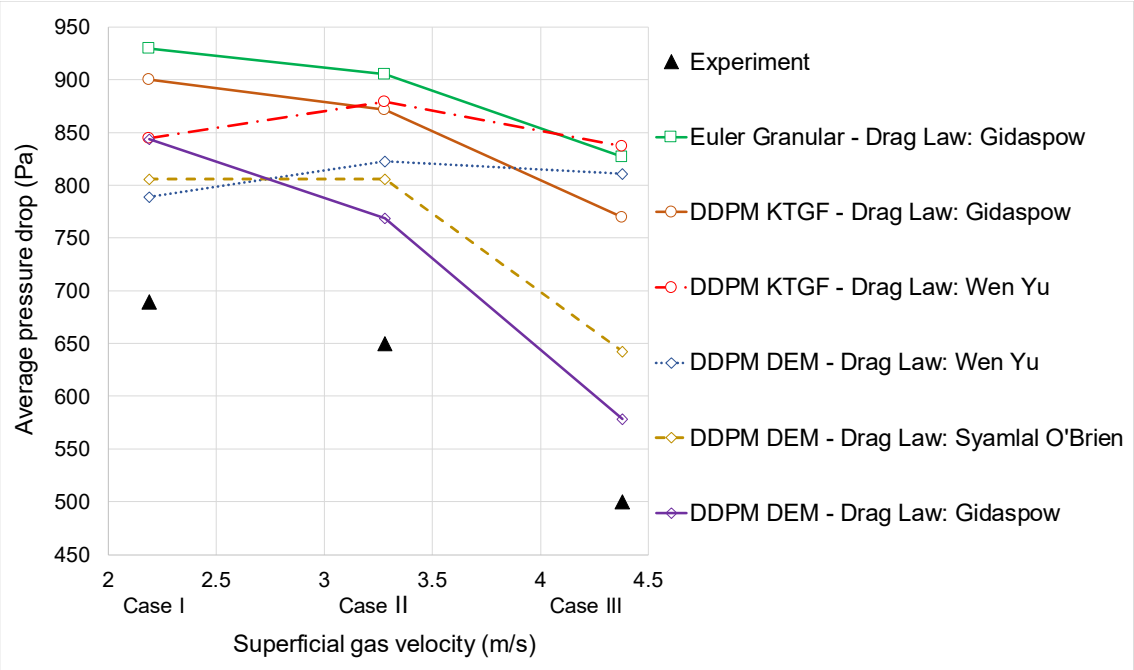

Figure 4-27: Pressure drop across bed between z = 0.04 m and z = 0.34 m.

The over-predictions are also reported in the literature. Koralkar and Bose [36], who were doing DEM simulations with different drag laws, are reporting pressure drop deviations of about 17% (case I) to 20% (case II), and up to 55% for case III (using same drag laws). The pressure drop deviations, obtained by Tandon and Karnik [65] (Euler Granular model) as well as by Ayeni et al. [60] (DEM) and Elghannay and Tafti [59] (DEM) are in the same magnitude.

The traditional drag laws are yielding over-predicted drag forces due to the coarse grid. The primary reason is that the influence of the microscale structures on the macroscale structures cannot be determined on coarse grids [68]. Igci and Sundaresan [69] were introducing filtered drag coefficients which are modeling the microscale structures and resolving the macroscale ones. That approach is an affordable alternative to a highly resolved mesh. Ozarkar et al. [68] are reporting better results with approaches based on filtered drag laws. ANSYS® Fluent provides the possibility to write user-defined functions (UDF's) for personalized drag laws [13]. In the literature, many alternative drag laws can be found. For example, Koralkar and Bose [36] were additionally testing drag laws by Hill et al. [70,71], Beestra et al. [72] and Rong et al. [73]. These approaches yielded better results than the traditional drag laws. In addition, calculations using drag approaches by Arastoopour et al. [74] and Ayeni et al. [60] and Milioli [75] (based on filtered drag coefficient) can be found in the literature [60,65].

4.4.9 Parallelization

Multiphase models are numerically very demanding, particularly the DDPM-DEM models. In addition, Euler Granular models, which are using different discrete phases or a particle size distribution, can result in demanding calculations (compare chapter 3.1). To keep the overall simulation time low, possibilities for calculation acceleration were investigated. The standard method is, to parallelize the calculation on different CPU cores by separating the mesh in different partitions [10]. Every CPU core is calculating another part of the flow field (partition). This splitting is very effective for single-phase fluid flows with a high cell amount. However, all calculated multiphase models were using a relatively low number of cells (chapter 4.3.2). A problem for DDPM fluidized bed models is the uneven distribution of the particles inside the mesh. The particles are tracked through the flow field. Every time a particle is moving from partition A to partition B the information about the particles is transferred from CPU A to CPU B. This information transfer is slowing down the calculations. Therefore, particles should change the partition as seldom, as possible to avoid unnecessary data transfers Hence, the interfaces between different partition regions should be as small as possible [13,17].
One possibility is to use one partition for the whole packed or fluffed bed of particles – shown in Figure 4-28 (a) and (c). Each color is representing one partition. The particles will rarely change their partition so that the data transfer rate between the CPU cores is low (ANSYS® Fluent default setting, called metis-method [13]). It will balance the mesh into around equal partitions with small data transmission interfaces. The problem with the standard setting is now that the particle load is differently distributed on the cores. Because the mesh is just split by the mesh size and shape, one partition may include all particles, and the others are just handling the continuous phase. Figure 4-28 (a) is an example of this. All injected particles are inside the red partition. With a low superficial gas velocity, most of the particles will remain in this partition.
The idea was to separate the partitions along the main flow direction – see Figure 4-28 (b) and (d), that every partition contains a similar number of particles. This option is called “Cartesian RZ-coordinates” (captioned as “cart-RZ-coo” in the following charts) [10]. It avoids the uneven distribution of particles on different cores. A disadvantage of this method is the much bigger interface between the partitions, which leads to a high data transmission rate [13,17].

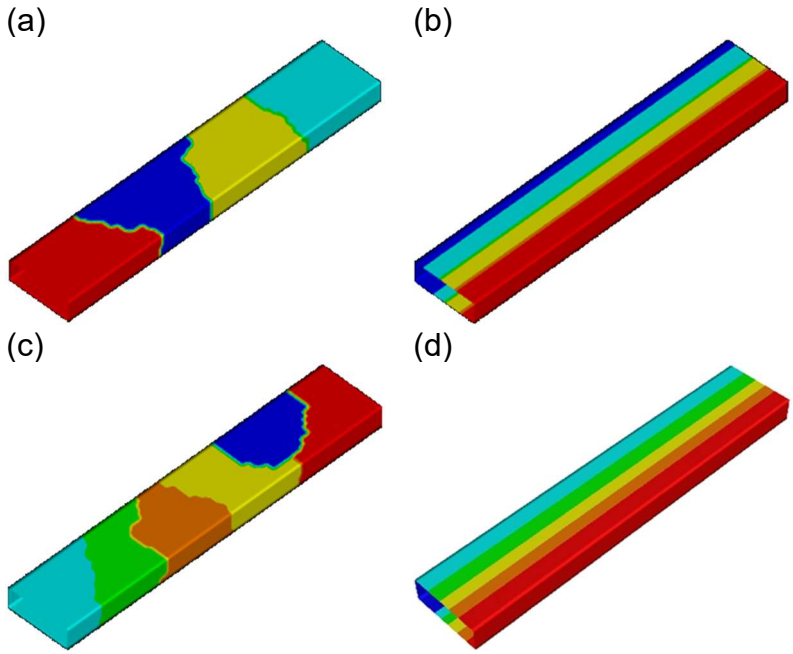

Figure 4-28: Partition options in ANSYS® Fluent
(a) metis - 4 cores, (b) Cartesian-RZ coordinate - 4 cores
(c) metis - 6 cores, (d) Cartesian-RZ coordinate - 6 cores

Because it was unclear which approach will have more effect on the calculation time, different multiphase models were calculated with different CPU settings. Calculations were done with an Euler Granular model, a DDPM-KTGF model, and a DDPM-DEM model. For comparison, all calculations (for case I) were done on a single processor. Afterwards, 4 cores and 6 cores were used to calculate the same case. For comparison, the same machine was used (ANSYS® Fluent v17, 6-cores, 3.2 GHz and 32 GB RAM).
An exception is the DEM model, which was not calculated on a single core for the extended test run. The calculation in serial mode would have needed too much time. For evaluating the results, the wall clock time, as well as the total calculation time was recorded. The wall clock time is the net-calculation time of the CPU, not considering any plotting or reporting operations during the calculation. In the total calculation time, everything is accounted. The total calculation time includes the creation of plots and reports as well as the time needed for auto-saving the data files [10,13].
First, short tests for 300 time steps (0.3 s of real time) were performed. Then longer lasting calculations were evaluated (in total 20 s real time). The long runs were paused after 12.5 s simulated time for exporting the results (fully fluidized after 12.5 s). Then the calculations were continued for 7.5 s to evaluate the difference in calculation time for an established fluidized bed. The extended tests were executed in serial mode and in parallel mode with six cores.

Short test runs

Figure 4-29 shows the comparison for all models. Generally, the calculation time is getting lower with a higher amount of parallel processes. However, this effect was not directly proportional. Switching to four cores yielded a 2.88-times accelerated calculation (compared to serial mode). With six cores the time-advantage was about 3.5 times for the best case. The reason is the increasing number of boundaries between the partitions. Every additional partition also needs additional effort for information transfer between the cores. For the short test runs, the partition option with evenly distributed particle load was the faster variant for the DDPM calculations. That finding agrees with the assumption that the particle tracking is significantly influencing the calculation time. Since no individual particle tracking exists in the TFM, also no time advantage should be observed with Cartesian RZ -coordinates. Figure 4-29 (a) is proving that. Just balancing the cell amount between the partitions is the best option in this case.

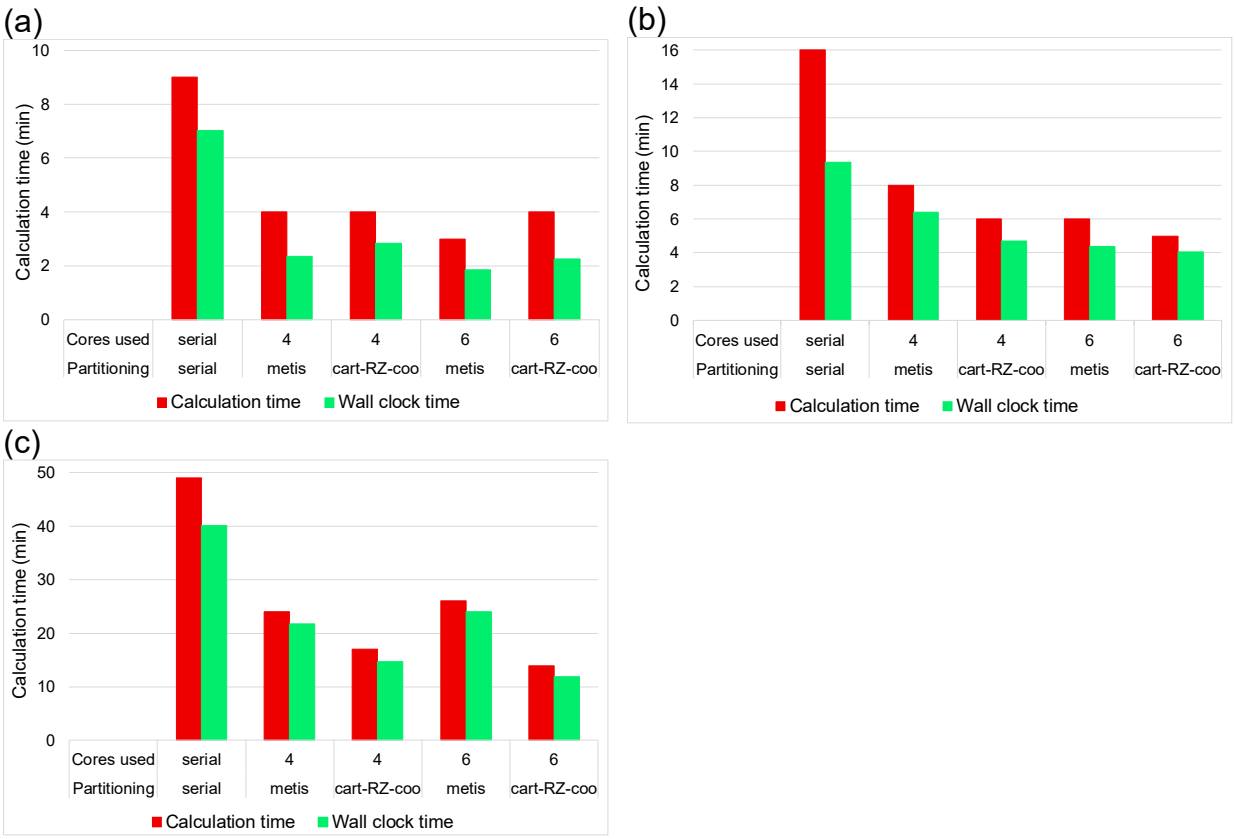

Figure 4-29: Calculation time - short run for 0.3 s
(a) Euler Granular, (b) DDPM-KTGF (c) DDPM-DEM.

Long test runs

For the long test runs, the calculation acceleration was low. Running on six cores was just between 1.3 – 2.3 times faster than running in serial mode. In contrast to the short tests, the default partition method Metis was always the fastest choice. Therefore, no benefit was achieved by using the alternative partition method. The advantage for the short run was due to the particle movement at the start of the fluidization. In the beginning, all particles are nearly vertically rising. In that case, few particles are changing their partition. When the bed is fluidized, and the preferred particle paths are developed (compare chapter 4.4.2), the particles are changing quite often through the partitions.
The particle tracks have a significant influence on the calculation time. However, because of the preferred motion inside the bed, no advantage is achieved by using the Cartesian-coordinates-RZ method. Instead of using conventional partition methods for parallelization, it might be more advantageous to accelerate the information exchange between the individual cores. For example, using GPU's additionally to CPU's could improve the calculation time, if the graphics memory is sufficiently large enough for the used model [13,76,77].

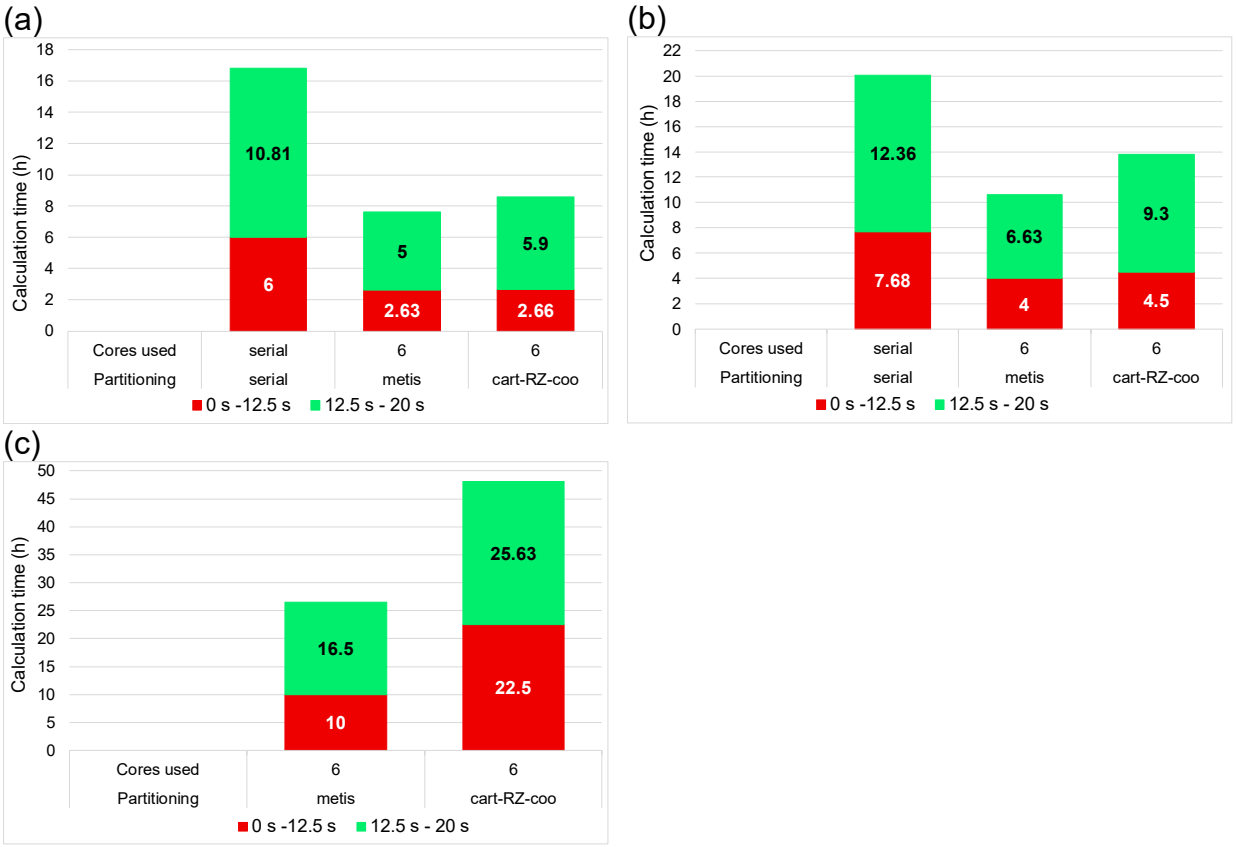

Figure 4-30: Calculation time - long run for 12.5 + 7.5 s
(a) Euler Granular, (b) DDPM-KTGF (c) DDPM-DEM.

Model comparison

A direct comparison of the calculation time between the multiphase models can be found in Figure 4-31. The DEM model needs more than 2.5 times longer for calculation than the DDPM-KTGF model. Therefore, DEM-Models are still not widely used for industrial scale problems. A cold flow model, just considering the hydrodynamics in a small fluidized bed takes for 20 s simulated real time already needed more than one day of calculation time (in average the DEM calculations needed even more than 30 h for 12.5 s real time, compare with Table 4-6).
All calculations done with the Euler Granular model were faster than the ones using the DDPM-KTGF models. The reason is the uniform particle size, which requires only one set of conservative equations for the solid phase. Although a DDPM-KTGF is not solving any conservative equation for the solid phase, it is calculating all particle tracks, which is slowing down the calculation (compare with chapter 3.3 and chapter 4.4). The Euler Granular model is between 1.3 - 2.7 times faster than the DDPM-KTGF model.

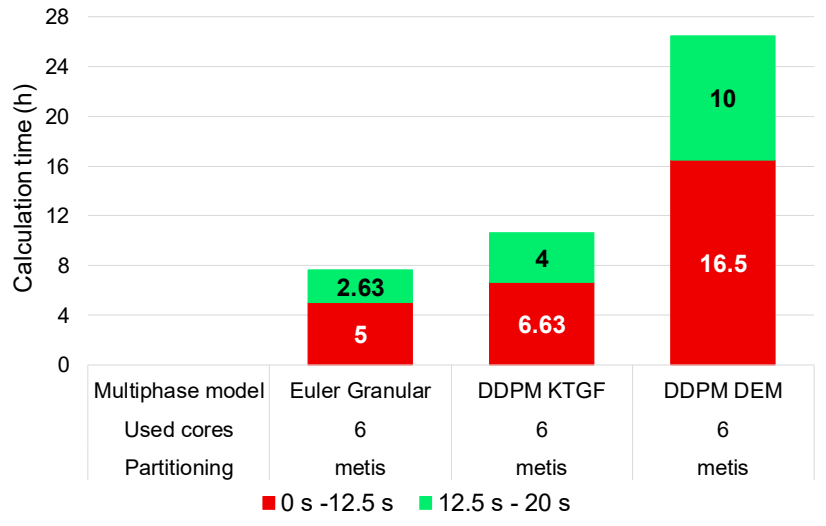

Figure 4-31: Calculation time – comparison of multiphase models.

4.5 Discussion NETL I

The DDPM-DEM model predicted the best results (chapter 4.4). It was the only model, which predicted the particle velocity near the wall without the need for additional models (e.g., Johnson and Jackson [29]). However, the drawback of the model is the high numerical demand. Since the NETL I challenge is a small-scale problem with a very low particle number, the calculation time was still acceptable. However, for most industrial beds, the DDPM-DEM approach is still too costly. The DDPM-DEM models needed more than 2.5 times longer for calculation than the DDPM-KTGF models.
DDPM-KTGF is a faster model, which is approximating the particle interactions with the granular temperature concept (see chapter 3.4). However, the accuracy is especially for the denser regions and nearby to the walls less reliable than for the DDPM-DEM models. According to other NETL challenge modelers (Tandon and Karnik [65], Lungu et al. [58]), an additional wall boundary condition for the granular phase (e.g., Johnson and Jackson [29]) can significantly improve the results (careful choice of the specularity coefficient necessary, compare with chapter 3.7 and chapter 5.2.4). Another possibility to improve the results to include inflation layers in the mesh [13]. Ozarkar et al. [67] stated that the inflation layers are essential for the prediction of the particle down-flow next to the wall. For the NETL III Task 3, the Johnson and Jackson [29] model and inflation layers were included (compare with chapter 5.2.4). The Euler Granular model in combination with the KTGF approach is yielding similar results as the 1.3 - 2.7 times slower DDPM-KTGF model. However, the complexity of the model is restricting it to a few particle diameter sizes (more details in chapter 5.1.3).
Generally, the results were improving with higher superficial gas velocity (case II and case III). Calculations nearby to the minimum fluidization velocity should be avoided and are not common in industrial plants [1]. Regarding the granular viscosity model, the model by Syamlal O'Brien was yielding the best results. Since every drag law had strengths and weaknesses, no general recommendation for the drag model can be given. However, the Gidaspow approach was the most reliable drag law for higher superficial gas velocities. The pressure drop was over-predicted in every case (Figure 4-27 in chapter 4.4.8). This effect is also observed by many other authors (Koralkar and Bose [36], Tandon and Karnik [65], Ayeni et al. [60], Elghannay and Tafti [59]). For improving pressure drop predictions, the use of alternative drag laws might be necessary. For example, Ozarkar et al. [68] were testing the drag law derived by Milioli et al. [75], which was yielding significantly better results.
Turbulence models are not essential for small-scale cold-flow problems like the NETL I. Calculations using the default laminar model are yielding competitive results. For the used Geldart D particles, the influences of the particle/wall and particle/particle interactions were much higher than the influence of the turbulence model. However, for reactive fluidized beds, a turbulence model is mandatory, since the reaction rate is significantly influenced by turbulent mixing and eddy dissipation [58,61]. Moreover, for calculations, the plenum chamber and the distributor plate were neglected or simplified. Including these parts could improve the quality of the results. Furthermore, there is potential for improved results by reducing the cell size and the time step. As explained in chapter 4.3.2, a minimum cell size is required, which limit was not exploited. In addition, for a better DDPM-KTGF particle tracking the time step can be further reduced.
Investigations on calculation accelerations using partition settings were not successful. The default settings were the fastest choice when considering the whole simulation time. Furthermore, parallelization is not proportionally speeding up the calculations. Parallel calculations on 6 cores were just about 2.5 times faster than calculations in serial mode (single core).

5 Simulation of NETL challenge III

After gaining experience with small-scale beds, a more industry relevant challenge was investigated. Again, a challenge published in 2010 by NETL in cooperation with the Particulate Solid Research Inc. (PSRI) was chosen [78]. Challenge III is primarily handling with industrial-scale fluidized beds. In contrast to the NETL challenge I, challenge III is using a broad particle size distribution [78]. The investigations on particle size distribution modeling were also one of the main tasks for this challenge. Another important question was which drag laws are suitable for modeling of circulating fluidized beds. In the bed, the volume fraction of the granular phase is always relatively high, however, for the particle transport (e.g., in recirculation pipes in CFB's) the solid-gas mixture can be very dilute. Therefore, another point of interest is the behavior of the applied multiphase models when areas with very dense regions and very dilute regions are occurring. The NETL III challenge is divided in three different tasks. The tasks are listed in Table 5-1 [78–81].

Table 5-1: NETL challenge III tasks [78].

	Name	Abbreviation
Task 1	Fluidization challenge	FB
Task 2	Bubbling fluidized bed challenge	BFB
Task 3	Riser, circulating fluidized bed challenge	CFB

First, the fluidization curve (compare chapter 2.1) for a small fluidized bed should be reproduced for two different kinds of bed material (see chapter 5.1). The model set-up should be optimized to obtain a good representation of the fluidization curve. This task will be referred to as "Fluidization challenge" (FB) or as Task 1 [82].
The bubbling fluidized bed (BFB or Task 2) was not evaluated within this thesis. Task 3 is a circulating fluidized bed (CFB). The superficial gas velocity is high enough to entrain the bed material. Experimental data for different recirculation rates and particle size distributions are provided by NETL. The particle size distribution is not the same as in Task 1 and 2. Investigations on the riser are presented in chapter 5.2. In Figure 5-1, the different experimental set-ups are shown. The pictures are showing the actual simulated parts of each task [78,83].

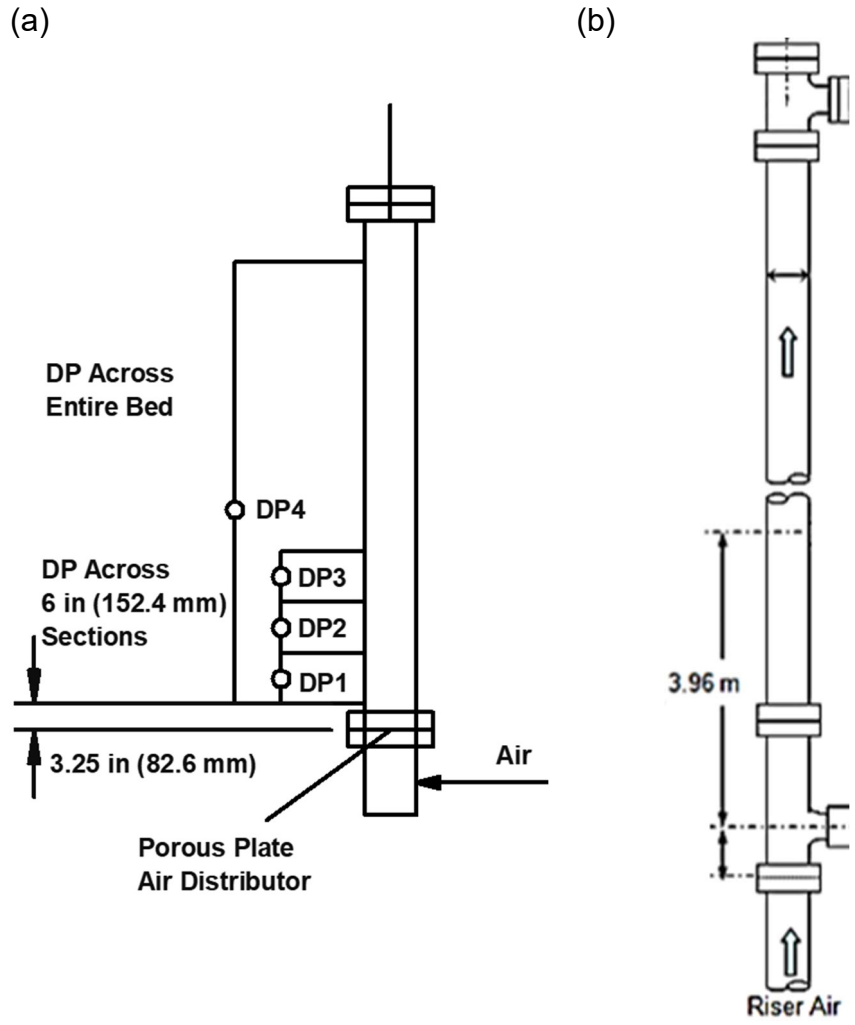

Figure 5-1: NETL challenge III
(a) Task 1 [82], (b) Task 3 [83].

5.1 Task 1: Fluidization challenge

For Task 1 the fluidization curve should be reproduced. Experimental results for two different particle size distributions are given [80]. The parameters of the multiphase models, the missing particle properties (details in chapter 5.1.1) and the numerical settings should be adjusted to reach a good agreement between measurement data and simulation results [80].

5.1.1 Problem description

Geometry

Task 1 is a lab-scale fluidized bed. The bed section is circular, and the bed dimensions are relatively small (Table 5-2). The experimental set-up is shown in Figure 5-2. The fluidizing gas is air. The air is evenly distributed by a porous plate [82]. The air density was calculated with the ideal gas law as ϱ_{air} = 1.2041 kg/m^3. The dynamic viscosity was calculated by Sutherland´s law: μ_{air} = 1.82E-05 kg/(ms) [55]. The air had a temperature of t_{air} = 20°C and an ambient pressure of p_{air} = 101,325 Pa [78,82].

Table 5-2: Dimensions for Task 1 [82].

Dimension		
Height	(m)	1.625
Outside diameter	(m)	0.178
Inside diameter	(m)	0.152
Length of measurement sections	(m)	0.1524

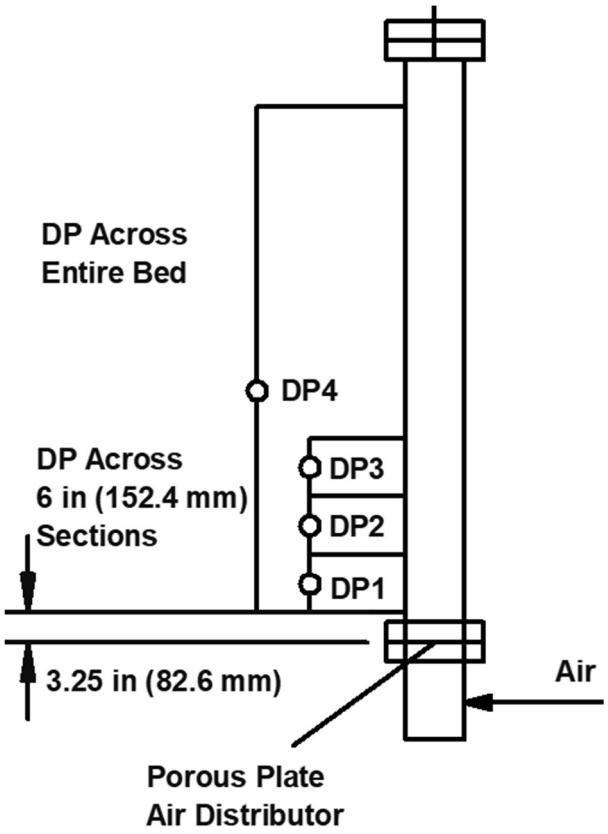

Figure 5-2: NETL III Task 1: Experimental set-up [82].

Particle properties

Experiments were executed with two different kinds of bed material. The particle size distribution (PSD) was labeled by the mass fraction content of fine particles [80]. Fine particles are solids with a diameter smaller than d = 44 μm. Particle size distribution A consists of 3% fine particles. Distribution B has 12% fines. The given particle properties are listed in Table 5-3. Not all necessary information was provided. For example, the data for the restitution coefficients as well as information about the initial bed (bed height and volume fraction) is missing. These missing values should be used as a parameter for the calculation. Challenge participants are asked to vary the parameters in order to obtain the real fluidization curve [78,81,82].

Table 5-3: Particle properties for Task 1 [82].

		PSD A	PSD B
Mass fraction of fine particles (d < 44 µm)	(%)	3	12
Particle type		Geldart A [5]	Geldart A [5]
Density	(kg/m^3)	1,489.86	1,489.86
Sphericity	-	0.98	0.98
Minimal diameter	(µm)	5	5
Maximum diameter	(µm)	290	165
Sauter mean diameter	(µm)	78.7	68.1
Initial particle weight	(kg)	7	6.832

The provided particle size distributions are presented in Figure 5-3. Since the mass fractions of the smallest, and the biggest particles are close to zero, the graphs are not showing the full distribution (maximum and minimum diameter are listed in Table 5-3) [82].

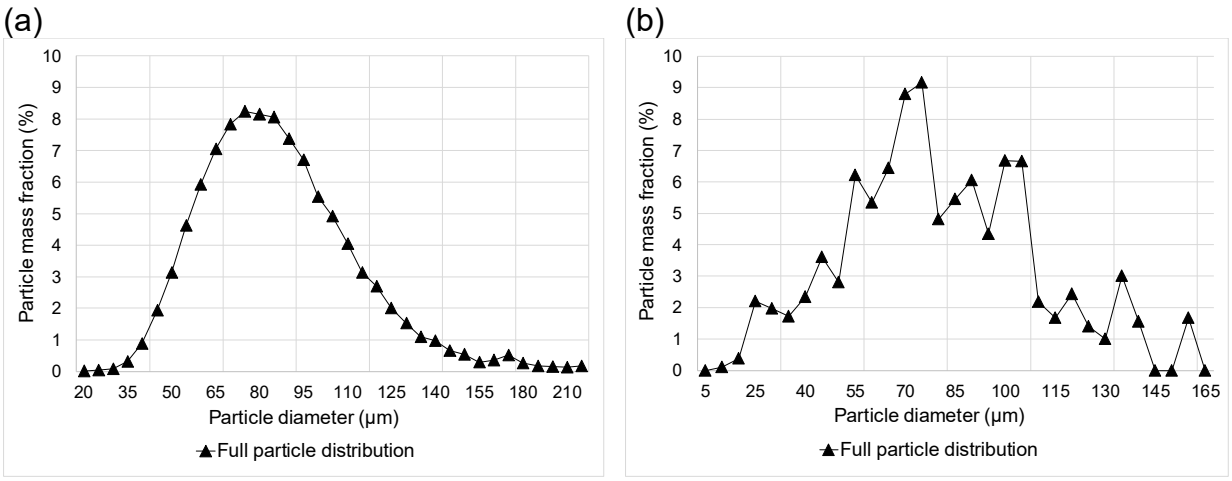

Figure 5-3: NETL III Task 1: Particle size distributions [82],
(a) particle size distribution A (3% fines), (b) particle size distribution B (12% fines).

5.1.2 Provided data

The observed measurement section DP2 reaches from bed height z = 0.235 m to z = 0.3874 m (see Figure 5-2). The pressure drop was measured for several superficial gas velocities. The range of air velocity was between zero and U_{max} = 0.0144 m/s. In Figure 5-4, the experimental results are presented. The obtained fluidization curve is typical for the used particle type and distribution [1,5,82].

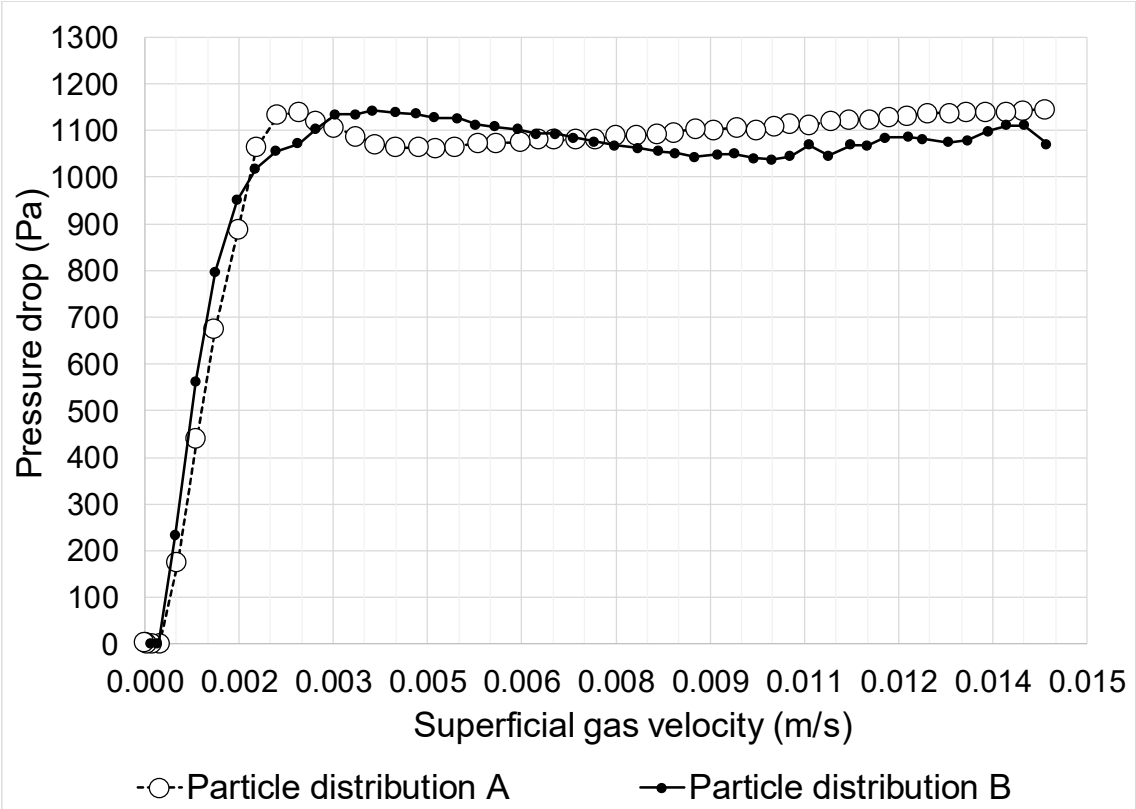

Figure 5-4: NETL III Task 1: Fluidization curve across DP2 [82].

Experimental data was provided for about 50 different superficial gas velocities. The fluidized regime can clearly be distinguished from the packed bed regime. Below the minimum fluidization velocity, a nearly linear increase of the pressure drop can be observed. Around the minimum fluidization velocity, a small, non-linear transition area is recognizable (more distinct for PSD A). For velocities higher than U_{mf} the pressure drop is statistically constant. The bed is fluidized (also compare with chapter 2.1 and chapter 2.3). The minimum fluidization velocity for particle size distribution A is about U_{mfA} = 0.0023 m/s and for PSD B about U_{mfB} = 0.0025 m/s [78,82].

5.1.3 Models and settings

Multiphase models

The focus of this work was on DDPM-KTGF models and primarily they were used for modeling NETL challenge III, since the Euler Granular model, as well as the DDPM-DEM models, are getting numerically too demanding for fluidized beds with a high particle number, especially when using a PSD (compare chapters 3.5 and 4.4.5).
The Euler Granular model would require an own set of conservative equations for each size class (every size is considered as an own phase). In addition, a drag relation between each phase is necessary. An Euler granular model with one granular type with ten different diameter size classes and one continuous phase is resulting in 11 different phases. Therefore, the Euler Granular model already has to solve 44 conservative equations (1 x continuity, 3 x gas momentum, 30 x particle velocity, 10 x volume fraction), when not considering any turbulence model. Additionally, 11 drag laws have to be defined (more drag laws possible since a drag between two solid phases can be defined in the TFM approach). Solving of all these equations is already numerically very demanding.

The DDPM-model, which only needs one solid phase for all modeled size classes, is in advantage. DDPM is only solving four conservative equations (1 x continuity, 3 x gas momentum). Calculations for the solid phase are only executed in the Lagrangian frame (Compare with chapter 3.1 and chapter 3.2) [10,12].
For simulating the minimum fluidization challenge, the most promising settings found in the NETL I challenge were used. For the granular viscosity, the approach by Syamlal O'Brien was used. For the drag law, the formulation derived by Gidaspow was chosen. Since the superficial gas velocities are low and a dense bed can be expected, a frictional viscosity model was included. In Table 5-4, the applied models and sub-models are summarized. The small mass defect due volume injection (see chapter 4.3.1) was neglected since no detailed investigations of sub-models were done, which would require an exact reproducibility of the initial mass. The values of the listed specularity coefficient and the coefficient of restitution were first estimated with the experience obtained from NETL challenge I and then adjusted (listed ones in Table 5-4) by the help of literature to obtain a good agreement to the experiments [68,84].

Table 5-4: NETL III Task 1: Used DDPM model.

Multiphase model	DDPM
Particle interactions	KTGF
Particle seeding	Volume injection
Drag law	Gidaspow [25]
Granular viscosity	Syamlal O'Brien [26]
Granular temperature	Algebraic
Frictional viscosity	Schaeffer [30]
Frictional pressure	Based-KTGF
Granular bulk viscosity	Lun et al. [28]
Solids pressure	Lun et al. [28]
Radial distribution	Lun et al. [28]
Solid wall boundary condition	Johnson and Jackson [29]
Specularity coefficient	0.3
Restitution coefficient solid-solid	0.84

Additionally, an Euler Granular – packed bed model was set up for comparison. It was used for the non-fluidized regime below U_{mf} (see chapter 5.1.4). The packed bed option is freezing the velocity field for the solid phases [13]. Details about the model can be found in the ANSYS® Fluent Theory Guide [10] and the User's Guide [13].

Table 5-5: NETL III Task 1: Used Euler Granular models.

Multiphase model	Euler Granular – packed bed
Particle interactions	KTGF
Particle seeding	Volume injection
Drag law	Gidaspow [25]
Granular viscosity	Gidaspow [25]
Granular temperature	Algebraic
Frictional viscosity	None
Granular bulk viscosity	Lun et al. [28]
Solids pressure	Lun et al. [28]
Radial distribution	Lun et al. [28]
Solid wall boundary condition	Johnson and Jackson [29]
Specularity coefficient	0.3
Restitution coefficient solid-solid	0.9

Calculated cases

Not all 50 superficial gas velocities were calculated, to keep the overall calculation time low. About ten velocities were chosen for evaluation. Inside the fluidized regime, the points were divided into broader ranges. Around and below the minimum fluidization velocity more cases were calculated. Since the minimum fluidization velocities are very low, also the Reynolds numbers are very low. For the lowest superficial gas velocity (U_{min} = 0.0005 m/s) the Reynolds number is about Re ~ 5. The Reynolds number for the highest superficial gas velocity (U_{max} = 0.014 m/s) is Re ~ 145. Because of the low Reynolds number, the influence of the turbulence was neglected, and the default laminar model was used [82]. As mentioned before (chapter 5.1.1), not all necessary information about the initial particle inventory was provided. Just the initial mass of the bed was provided for each particle size distribution. Therefore, the initial bed height and the void fraction had to be estimated. Jang and Arastoopour [84] were initializing the calculation with a solids volume fraction of α_s = 0.54. Ozarkar et al. [68] were using a particle fraction of α_s = 0.6. For calculations in this work an initial solids volume fraction of α_s = 0.55 was chosen. No information for the particle restitution coefficients and the specularity coefficients were given [29]. The restitution coefficient between particles was set to η_{ss} = 0.84, the coefficient between wall and particles is set to η_{sw} = 0.92. These values were taken from the NETL challenge I. Jang and Arastoopour [84] were using a particle-particle restitution coefficient of η_{ss} = 0.9. For the particle-wall coefficient, they set η_{sw} = 0.3. Ozarkar et al. [68] also were using η_{ss} = 0.9, however, they provided no information about their used particle-wall restitution coefficient. A specularity coefficient of φ = 0.3, was set for the solid phase wall boundary condition (Johnson and Jackson [29] – compare with chapter 3.7) [84].
In general, convergence was harder to achieve than in NETL Challenge I. With smaller time steps, convergence was getting better. For the first time steps (including the injection time step), very low values were needed. A time step size of Δt = 1E-05 s was used for these first iterations. After reaching good convergence and low residuals, the step size was slowly increased between Δt = 5E-05 and 7.5E-04 s, depending on the particular case.

Description of the particle size distribution

The provided particle size distributions (PSD) are reaching over a broad range (PSD A: 46 size classes, PSD B: 42 size classes, see Figure 5-3) [82]. The PSD was modeled to keep calculation times low. Three PSD models were investigated. First, the ANSYS® Fluent built-in Rosin Rammler fit has been tested. The Rosin Rammler fit is classifying the whole particle size distribution into diameter ranges. For each of this diameter classes, the inversed cumulative particle mass fraction is calculated (Y_d). The mean diameter for the Rosin Rammler distribution is, where Y_d = e^{-1}. A spread parameter is calculated using this mean diameter. Besides these values, the minimal and maximum diameters, as well as the number of wished diameters have to be defined. More details about the calculation of the PSD can be found in the ANSYS® Fluent Users Guide [13].
In addition, an own representation of the particle size distribution was created. A Sauter mean diameter (compare with chapter 2.5.4) was calculated for each size class. That variant will be called piecewise Sauter mean diameter. The advantage is that the size classes are manually defined. Therefore, size classes which are important for the fluidization (smaller particles) can be weighted more. A comparison of both approaches for five particle classes is given in Figure 5-5. The charts show, that the smallest and biggest particles in the Rosin Rammler fit are less good represented than the particles in the medium size spectrum.

However, especially the smaller particles have a significant influence on the fluidization [1,2]. The piecewise Sauter mean model allows a better representation of the whole PSD with the same number of particle size classes. For very regular PSD's (as in PSD A in Figure 5-5), the Rosin Rammler fit is well representing the PSD. However, especially for more irregular PSD's (as PSD B in Figure 5-5 or in Figure 5-7), the Rosin Rammler is not a good representation. For example, the second peak of PSD B (for d_s = 90 µm) is not considered at all. An own PSD model can be set to represent such local peaks. Therefore, the Rosin Rammler fit was used for first calculations (with five particle size classes). Afterwards, for obtaining a better agreement with the experiments, the more detailed PSD model piecewise Sauter mean diameter was used with a doubled number of particle size classes (only done for PSD B). The PSD model is shown in Figure 5-7 (b).

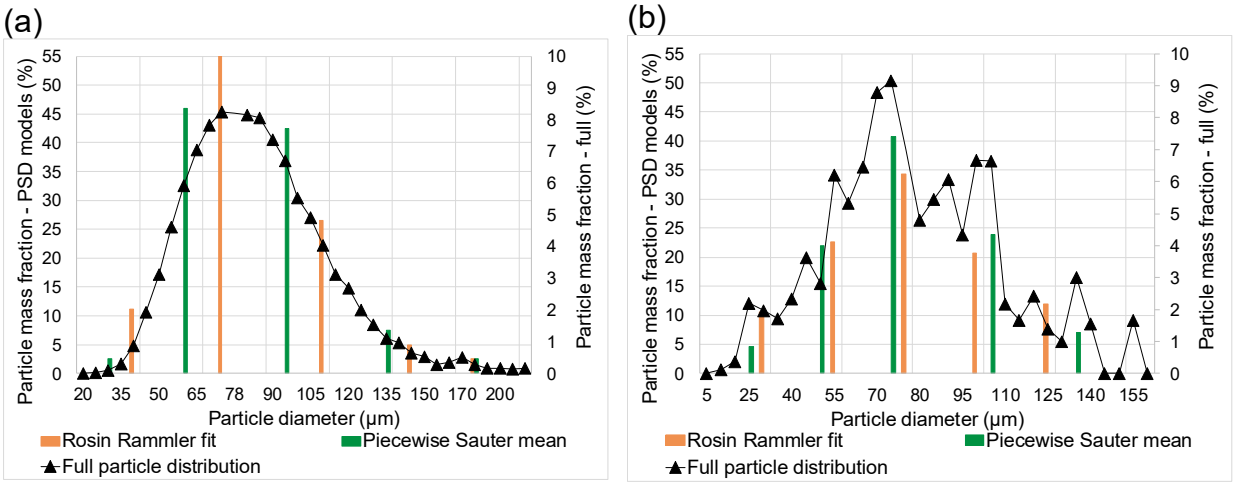

Figure 5-5: NETL III Task 1: PSD models, 5 size classes [82], (a) PSD A, (b) PSD B.

Another possible representation of the distribution is an overall Sauter mean diameter. With this approach, all particles are set to a uniform size. Details about the Sauter mean diameter can be found in chapter 2.5.4. An issue when handling with Sauter mean diameters is that smaller particles are weighted more than bigger ones (because it is more sensitive to the presence of small particles in the PSD) [2,7]. In the case of fluidized beds, the weighting is not a real disadvantage since the smaller particles have the biggest influence on the fluidization. According to Hofbauer [2], the Sauter mean diameter should not be used for very broad size distributions or size distributions like a bimodal distribution. Considering the whole particle size range, the Sauter mean diameter for PSD A is $d_{32\,A}$ = 78.7 µm and the one for distribution B is $d_{32\,B}$ = 68.1 µm [2].
The different PSD models, as well as the real distribution used in the experiments, are shown in Figure 5-6. The value Y_d, which is used in the charts is the reversed cumulative mass fraction, or in other words, Y_d is the mass fraction of all particles greater than the presently observed diameter [13].

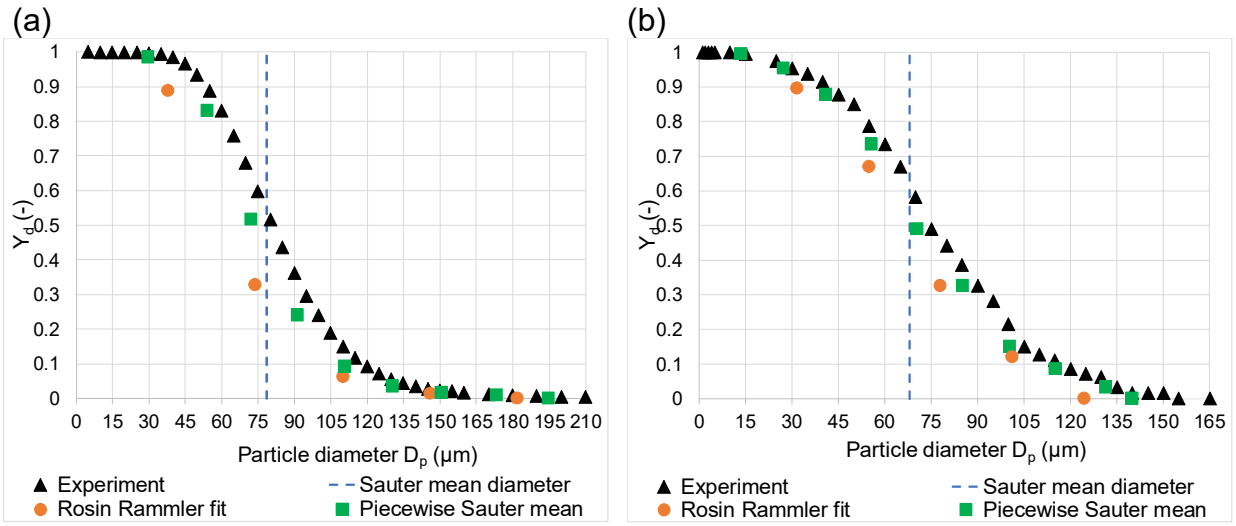

Figure 5-6: NETL III Task 1 & 2: Particle size distribution models [82], (a) PSD A, (b) PSD B

When using the Rosin Rammler distribution, the necessary parameters can directly be set in the injection panel. ANSYS® Fluent is automatically creating the distribution. Especially for diameters near the Sauter mean diameter, the deviations to the real distribution are quite high. Input parameters for the injection panel (volume injection) with Rosin Rammler fit are summed up in Table 5-6 [10,12,13].

Table 5-6: Rosin Rammler injection parameters.

		PSD A	PSD B
Minimal diameter	(µm)	20	20
Maximal diameter	(µm)	200	135
Mean diameter	(µm)	90.71	86.52
Spread parameter	-	2.889	2.594
Number of diameters	-	5	5
Total parcel amount	-	125,510	128,595
Total particle amount	-	1.34E+11	1.29E+11

For the piecewise Sauter mean diameter calculations, an own volume injection for each size class was created. Each of these injections is handling one uniform particle size. The initial particle load is injected at calculation start. The injection panel settings are summed up in Table 5-7. The chosen diameters (ten particle size classes) are shown in Figure 5-7. The PSD's are already well represented with ten size classes [2,12,13].

Table 5-7: Piecewise Sauter mean injection parameters.

		PSD B
Minimal diameter	(µm)	13.46
Maximal diameter	(µm)	140
Number of diameters	-	10
Total parcel amount	-	128,595
Particle amount	-	6.556E+10

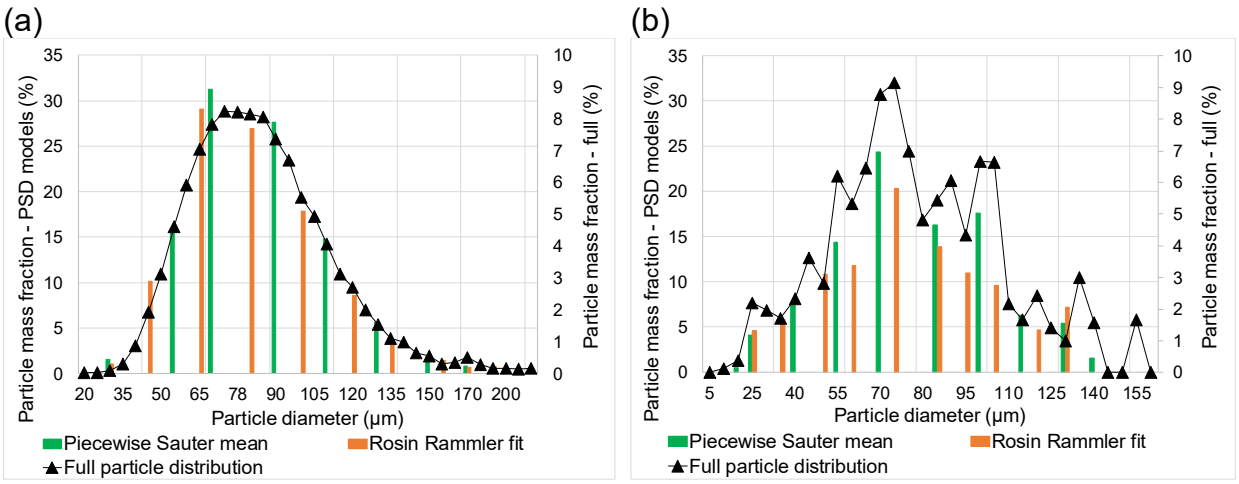

Figure 5-7: NETL III Task 1: Particle size distribution, 10 size classes [82], (a) PSD A, (b) PSD B.

For the calculations with an overall Sauter mean diameter, a single volume injection with a uniform particle size was used.

Mesh

The geometry was meshed with the same strategy as the first challenge. The mesh is relatively coarse with a cell size of 0.01 m (ANSYS® recommendation for DDPM models, also see chapter 4.3.2). Because of the relatively low superficial gas velocities and the very low Reynolds number, no boundary layers were used. The missing boundary layer, the minimum cell size restriction (5 packed parcels per cell), and the small over-all size results in a cell amount of 29,318 cells (Figure 5-8). The bed has a circular shape, which results in minimal distorted hexahedron elements [12,13].

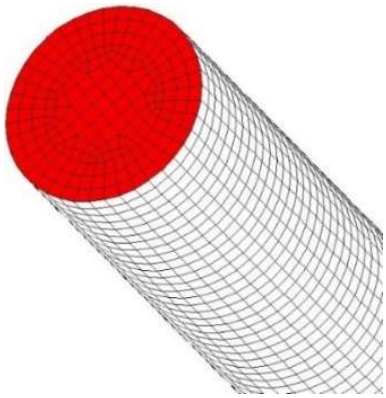

Figure 5-8: NETL III Task 1: Mesh.

5.1.4 Results

The calculations always started from an injected fixed bed. Then the velocity was slowly increased until the desired superficial gas velocity was reached. Afterwards, the static pressure values were averaged over a sufficiently long period to overcome the instantaneous pressure fluctuations (also compare chapter 4.4.1). Since the velocities of the calculated cases were reaching over several magnitudes, also the period until a statistically steady state was reached was different. Therefore, the calculation time for the different velocities was changing.

The fastest calculations (Rosin-Rammler fit with 5 particle size classes and high gas velocity) took about 15 hours and the slowest calculations (piecewise Sauter mean diameters with 10 particle size classes and low gas velocity) took about 30 hours. Calculation needed up to 8.42E-05 ms per cell, parcel and real time. The results were in good agreement with the experiments (for velocities higher than the minimum fluidization velocity). However, below U_{mf} the model is failing and cannot describe the linear increase of pressure drop with increasing superficial gas velocity.

Bed expansion

In Figure 5-9, the bed expansion for PSD B is shown. The graph shows the pressure curve obtained by the NETL experiments. Calculations were done with a DDPM-KTGF model and a piecewise Sauter mean PSD model. For a superficial gas velocity close to the minimum fluidization velocity of $U_{mf\,B}$ = 0.0025 m/s, the solid phase volume fraction is nearly constant over the full bed (U_f = 0.0034 m/s). The bed is expanded just to a very small extent compared to the static bed height. The bed volume is around 4.67% bigger than in the packed bed regime. No bubbles are formed yet. With doubled gas velocity (U_f = 0.0068 m/s), first bubbles can be observed. The fluffed bed volume is 9.44% bigger than the static bed. With still increasing velocity (U_f = 0.0122 m/s), bubbles are getting bigger and more numerous. The bed volume is already expanded by 12.73%.

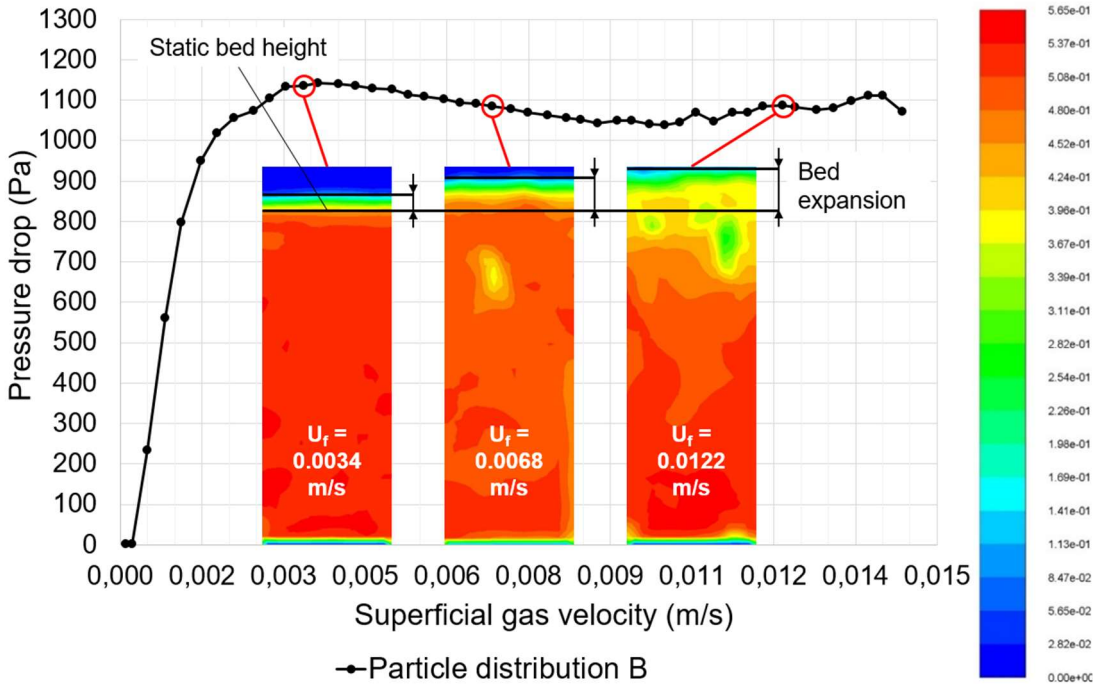

Figure 5-9: NETL III Task 1: Bed expansion of particle size distribution B, ***solid volume fraction (-)*** *contour plot.*

Pressure drop

As in the NETL challenge I (chapter 4.4.8) the pressure drop is over-predicted for most cases (see Figure 5-10). For higher superficial gas velocities, the agreement to the experiments is getting better. The slightly decreasing pressure drop between the minimum fluidization velocity (about 0.0023 m/s) and a value of about 0.005 m/s is not reproduced by the model. A reason might be the relatively coarse representation of the PSD with only five particle size classes.

The error in the fluidized regime is between 1.6 % – 13.4%. However, for low velocities (below the minimum fluidization velocity), the DDPM is failing. It was not able to reproduce the linear dependency of the pressure drop, the predicted pressure drop kept nearly constant. To determine the reason for that, PSD B was calculated with the same approach (Figure 5-11). In the fluidized regime, the calculation results for PSD B were better than the ones for PSD A. In addition, the curve trend is well recreated. The error in the fluidized regime is between 2.1% – 12.5%. Therefore, the Rosin Rammler results for distribution A and B are yielding similar accuracy. However, the pressure drop in the packed bed region was still not captured.

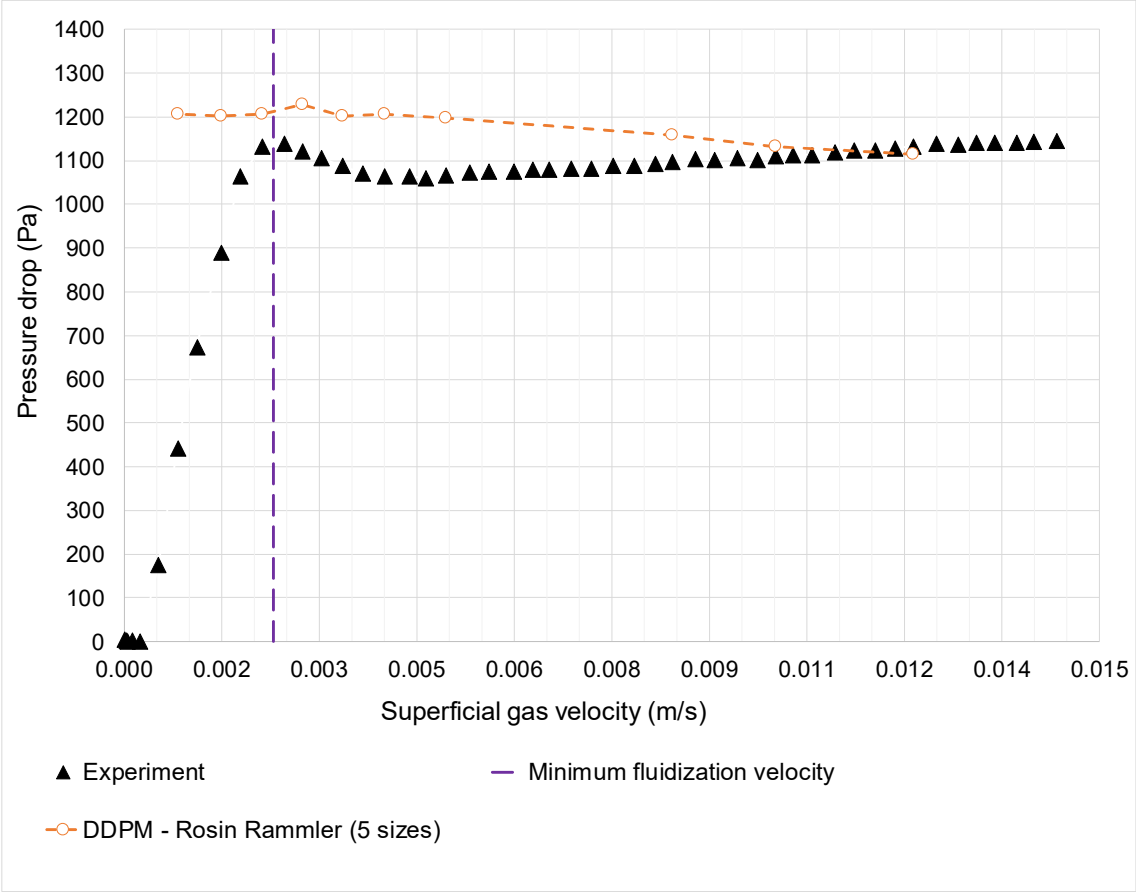

Figure 5-10: NETL III Task 1: Fluidization curve for PSD A across DP2 [82].

Therefore, a more detailed model for PSD B was tested to overcome this issue (see Figure 5-11). For determining the most promising PSD model approach, a single point (U_f = 0.0122 m/s, blue cross in Figure 5-11) was calculated respectively for a Rosin Rammler and a piecewise Sauter mean PSD model (both with 5 particle size classes). As shown in Figure 5-11, the piecewise Sauter mean diameter PSD model yielded slightly better results (about 6% deviation to the experiments) compared to the Rosin Rammler fit (about 7.5% deviation to the experiments). Therefore, the piecewise Sauter mean diameter (compare with chapter 5.1.3) approach was applied for the more detailed calculations. PSD B was chosen because of the less uniform particle distribution (see Figure 5-7) since it was assumed to be the more complex configuration. With the more detailed representation, the results were significantly improving. The error to the experiments ranged from 0.5% – 7.8%. The qualitative trend of the curve trend improved. However, below U_{mf} the model is still failing and cannot describe the linear increase of pressure drop with increasing superficial gas velocity.

Consequently, the reason for the failing DDPM was not an insufficient description of the PSD. Rather, the DDPM model itself was not able to calculate fixed beds (see summary on page 73).
Therefore, other models were tested for the non-fluidized regime. The goal was to obtain the linear dependency in the fixed bed regime. A KTGF Euler Granular model with the packed bed sub model was set up (inside secondary phase settings panel) – also see chapter 5.1.3 [10,13]. First, calculations were done with an overall Sauter mean diameter. The chart shows that the linear increase in the pressure drop was indeed reproduced. However, the gradient is not well represented. Furthermore, it was shown that a more detailed PSD model (piecewise Sauter mean diameters) improved the results.

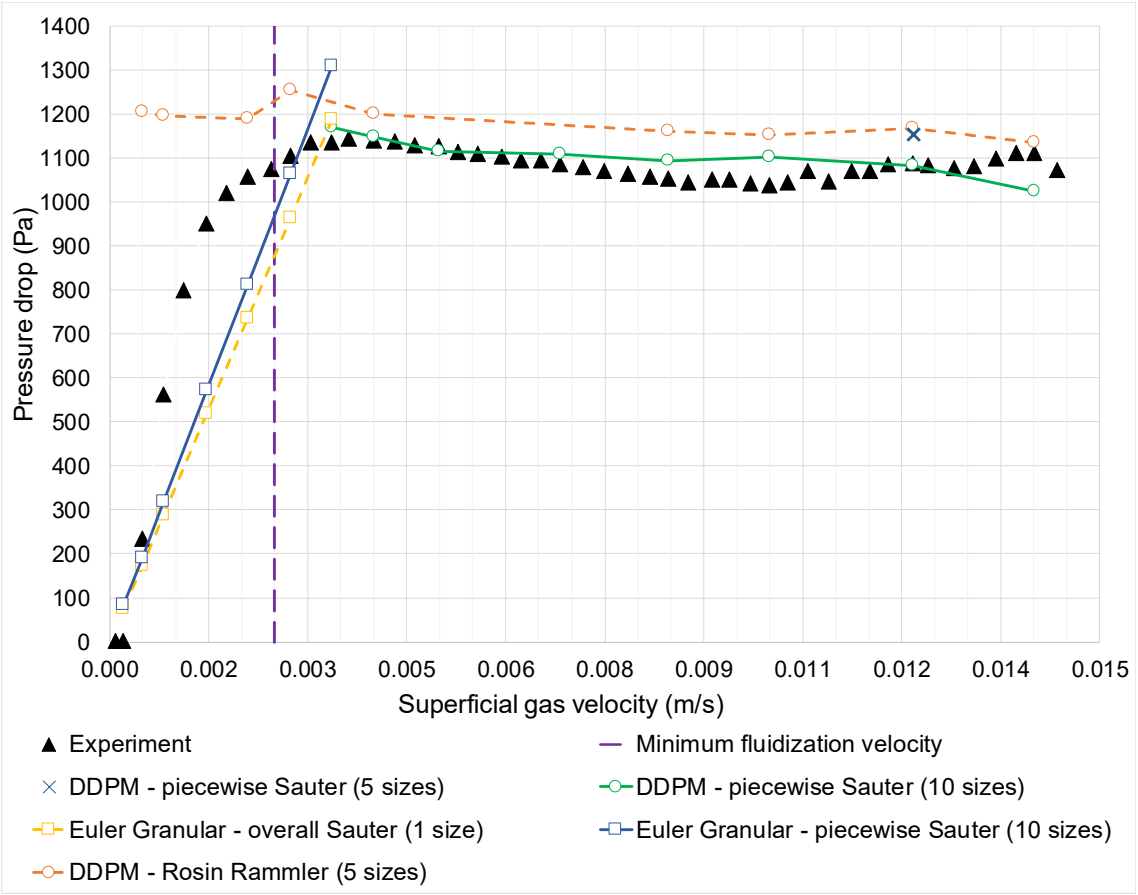

Figure 5-11: NETL III Task 1: Fluidization curve for PSD B across DP2 [82].

Summary

One reason for the failure of the DDPM-KTGF model for superficial gas velocities U_f below the minimum fluidization velocity U_{mf} could be the wrong prediction of the particle-particle interactions in the packed bed. When investigating calculations with very low superficial gas velocities, where no particle movement or bed expansion is expected, it was found, that the bed was already expanded. For example, for a superficial gas velocity of U_f = 0.0008214 m/s (U_{mfB} = 0.0025 m/s), the bed was already expanded for more than 2.5% [1]. Therefore, the DDPM already interprets the bed as fluidized, which would explain the predicted constant pressure drop in the packed bed region. The Euler Granular packed bed model, which is freezing the particle velocity (and is therefore preventing an unphysical bed expansion below U_{mf}) is predicting the linear dependency of the pressure drop. However, since fluidized beds are usually operating well above the minimum fluidization velocity, DDPM-KTGF is still a good choice. For beds operating close to U_{mf} or below in the packed bed regime, DDPM-KTGF is not recommended and a more detailed description of particle-particle interactions would be needed (e.g., with the DEM).

For modeling the PSD, two important factors exist. First, the shape of the PSD is important. Smooth and regular shaped distributions are easier to model (see chapter 5.1.3). Non-regular size distributions (e.g., bimodal distributions) are requiring models, which are not simply averaging the PSD. For example, the Rosin Rammler distribution is smoothing local peaks in the PSD. As shown in Figure 5-5 and Figure 5-7, the piecewise Sauter mean diameter PSD model is a better representation for local peaks, since a particle class can manually be set into the peak. Therefore, the piecewise Sauter mean diameter yielded better results (about 6% deviation to the experiments) than the Rosin Rammler distribution (about 7.5% deviation to the experiments) for the pressure drop. The second factor is the number of chosen particle size classes. An increasing number of size classes resulted in a much better representation of the PSD and therefore to better results (for piecewise Sauter mean diameters). A doubling of the particle class number (5 to 10 classes) was lowering the average pressure drop deviation to the experiments from 7.3% to 4.15%. Furthermore, the calculation time doubled as well (15h to 30h).

For NETL challenge III Task 1, the variants Rosin Rammler fit, and piecewise Sauter mean diameter were used. Task 1 still had a relatively low particle number in the bed (compared to Task 3). Therefore, the PSD models can be applied with reasonable calculation times (up to 30 hours). No detailed PSD models were used for the NETL III Task 3 (parcel number too high – compare with chapter 5.2.3). For Task 3, the overall Sauter mean diameter was used, which was sufficient for the recreation of the particle velocity profiles (more details can be found in chapter 5.2.3 and chapter 5.2.4). Task 3 is operating far above the minimum fluidization velocity. Therefore, the DDPM-KTGF can be used.

5.2 Task 3: Circulating fluidized bed challenge

5.2.1 Problem description

Task 3 of NETL challenge III is a circulating fluidized bed (CFB). The bed is operating in the pneumatic transport regime (compare with chapter 2.1 and chapter 2.3), so the particles are being entrained during the operation. Without recirculation of the particles, the bed will be evacuated [1,78,83,85].

Geometry

In Figure 5-12, the experimental set-up for the CFB challenge is shown. Inside the riser (left part) the particles are carried up. After leaving the riser, particles are separated from the air in the cyclones. The separated particles are transported back through the standpipe and the L-valve sparger [78,83]. The main dimensions of Task 3 are listed in Table 5-8. A common strategy for simulating CFB's is only to calculate the riser. Other parts were neglected or considered with boundary conditions. The reason for this is the necessary simplification of the model. A full-loop CFB calculation would require a high cell number [61]. Furthermore, the particles are very inhomogeneous distributed in the different CFB parts. The particle volume fraction in the riser is very low, whereas the particle volume fraction in the L-valve sparger and at the bottom of the standpipe is very high. Therefore, a complex model would be needed that can model the dense and dilute regions, as well as the transition regions. All of this would result in an unacceptable high calculation time. Therefore, just the riser was simulated (indicated with blue rectangle). Nearly all challenge participants were only simulating the riser [61,85–87]. An exception is a paper by Li and Dietiker [61], who were also calculating a full-loop case [85].

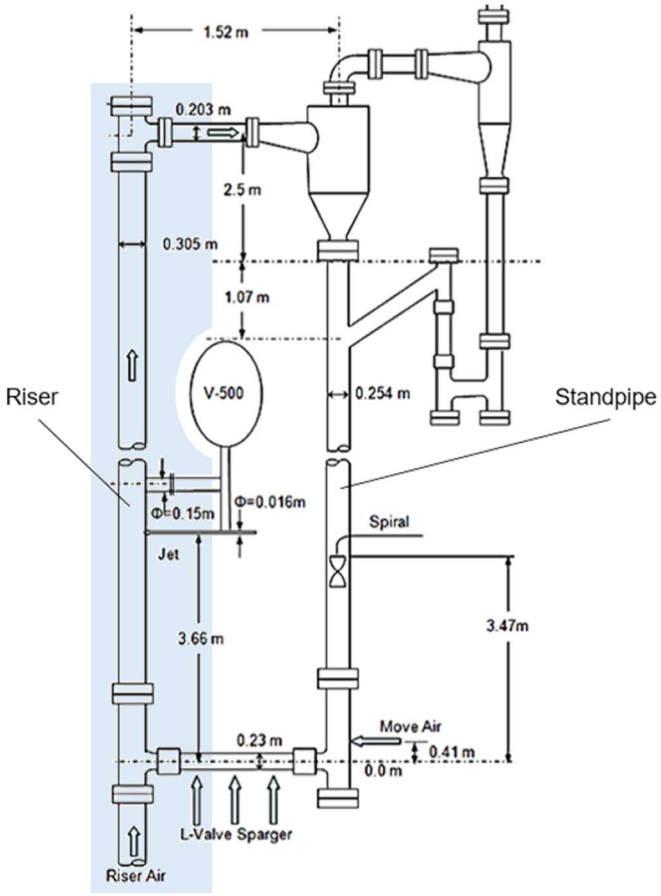

Figure 5-12: NETL III Task 3: Experimental set-up [83].

Table 5-8: Dimensions for Task 3 [85].

Dimension		
Riser height	(m)	16.79
Riser diameter	(m)	0.305
Exit diameter to cyclones	(m)	0.203
Diameter from L-valve-sparger	(m)	0.23

Particles

NETL was providing detailed particle properties and the full PSD for two different bed materials. Group A material consisted of glass beads with a Sauter mean diameter of d_{32} = 58.9 µm [44]. Group B particles were beads made of polyethylene with a Sauter mean diameter of d_{32} = 802 µm [44,85].

Table 5-9: Particle properties for Task 3 [85].

		Group A particles	Group B particles
Minimum fluidization velocity	(m/s)	0.0079	0.13
Particle type	-	Geldart A [5]	Geldart B [5]
Density	(kg/m^3)	2,425.1	863.3
Sphericity	-	0.98	0.95
Sauter mean diameter	(µm)	58.9	802

5.2.2 Provided data

Data was provided for five different cases. Besides the PSD, the recirculation rate and the superficial gas velocity at the bottom of the bed were varied. The case variations are summed up in Table 5-10. For this work, the cases 3, 4 and 5 were calculated. That was done because less data and variations were provided for PSD A. For PSD B much more information was available. Besides the influence of the recirculation rate, also the influence of the superficial gas velocity can be investigated for PSD B. According to the challenge providers, case 3 is near to the fast-fluidized bed transition. Case 4 is a core-annular flow, and case 5 is operating in the dense suspension up-flow. The pressure at the riser outlet was provided by NETL as well as the different superficial gas velocities at riser bottom and L-valve sparger [78,83,85].

Table 5-10: Cases for Task 3 [85].

Case	PSD	Superficial gas velocity (bed bottom) (m/s)	Solids circulation rate (kg/s)	Gas velocity from L-valve (m/s)	Riser outlet pressure (kPa)
Case 1	A	5.14	1.44	0.023	182
Case 2	A	5.14	9.26	0.036	167
Case 3	B	5.71	5.54	0.604	100
Case 4	B	7.58	7.03	0.573	102
Case 5	B	7.58	14	0.688	105

For validation of the simulations, the average pressure gradient and the radial profiles of the averaged vertical particle velocity were used. The pressure gradient was measured along the axial direction between 20 measurement sections. The vertical particle velocity profiles were measured along the bed height in different azimuthal directions. The azimuthal directions are defined according to cardinal points (see Figure 5-13) [83,85].

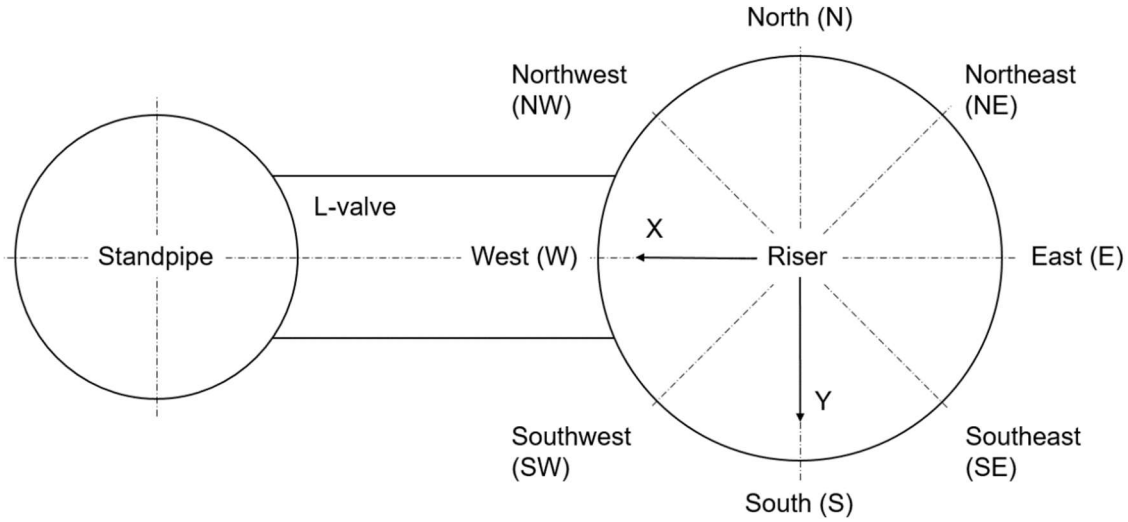

Figure 5-13: NETL III Task 3: Azimuthal directions of velocity measurements [83].

5.2.3 Model and settings

Multiphase model

The model was set-up with the experience gained in the previous challenges. The settings for the multiphase model are summarized in Table 5-11. The DDPM-KTGF can be used since the fluidization velocity is well above U_{mf} (compare with chapter 5.1.4). The frictional effects between particles were neglected, since the granular flow in the riser is very dilute). The riser is very tall and slim, therefore the wall influence was considered with a specularity coefficient of φ = 0.005 [86]. Since the lowest Reynolds number was about Re = 110,000, a turbulence model was included in the model. A time step of Δt = 0.0008 s was chosen [10,12,83,86].

Table 5-11: NETL III Task 3: Used models and settings.

Multiphase model	DDPM
Particle interactions	KTGF
Particle seeding	Volume injection
Drag law	Gidaspow [25]
Granular viscosity	Gidaspow [25]
Granular temperature	Algebraic
Granular bulk viscosity	Lun et al. [28]
Solids pressure	Lun et al. [28]
Radial distribution	Lun et al. [28]
Turbulence model	Realizable k-ε
Wall treatment	Enhanced
Turbulence multiphase model	Dispersed
Solid wall boundary condition	Johnson and Jackson [29]
Specularity coefficient	0.005
Restitution coefficient solid-solid	0.8
Restitution coefficient wall-solid	0.7

Handling of particle size distribution

Because the standpipe, the L-valve, and the cyclones were not included in the model, the particle mass loss on the riser top, as well as the recirculation of the particles at the riser bottom had to be modeled. The exit to the first cyclone was defined as a pressure outlet condition, and the DPM behavior was set to escape. The pressure at the top of the riser was provided by NETL. The air inlet from the L-valve was modeled by an additional velocity inlet boundary condition. For the particle recirculation, an additional injection was set up. The surface injection was chosen for seeding a continuous particle stream from a bounded plane (standard parcel method). The total mass rate was set to the recirculation rate of the L-valve [13,83].
The initial particle volume fraction was set to α_s = 0.1 (injected with volume injection, standard parcel method). Since no information about the actual or initial mass inside the riser was provided, calculations were executed until a statistically constant riser mass inventory was reached. The particle inventory data, after reaching a pseudo-steady state, is listed in Table 5-12. The particle to parcel ratio is not the same for the different cases, since the standard parcel method was chosen (ANSYS® Fluent calculates the particle per parcel amount for each case, depending on the regarding mass flow rate [13]). Calculations in Task 1 took up to 8.42E-05 ms per cell, parcel and real second. An upscaling of this value for Task 3 would mean a calculation duration of more than 10 days (because of the much higher parcel and cell number). Although, Task 1 and Task 3 are not directly comparable, that should be a sufficient first rough estimation. Therefore, the particle size distribution was just modeled by a single diameter (overall Sauter mean diameter – compare with chapter 2.5.4), in order to lower the overall calculation time.

Table 5-12: NETL III Task 3: Initial injection – volume injection.

		Case 3	Case 4	Case 5
Sauter mean diameter	(µm)	802	802	802
Total parcel amount	-	7,738,470	7,308,608	6,193,884
Total particle amount	-	3.7E+08	2.82E+08	4.53E+08

Mesh

Ozarkar et al. [67] were doing detailed studies on the grid topologies for the NETL III riser. Their findings were used as a guideline for the mesh creation. One of their key findings was that the presence of a boundary layer is essential for the particle down-flow prediction near the wall. According to them, boundary layers were included in Task 3. Nine inflation layers were used to improve predictions nearby to the wall. This layers reached over one-third of the riser radius [12,13,67].

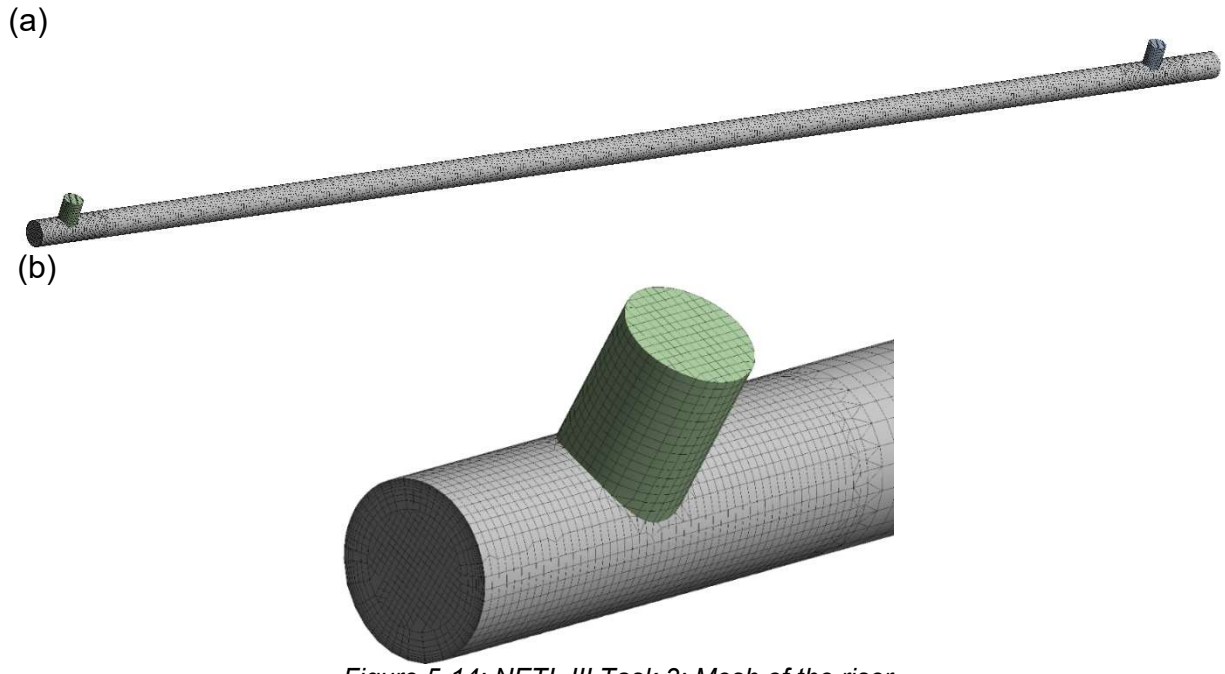

Figure 5-14: NETL III Task 3: Mesh of the riser
(a) full mesh, (b) detail of riser top.

Another key finding of Ozarkar et al. [67] was that the used grid topology has just a minor influence on the results. Therefore, a cut-cell method was used to ensure equally sized cells. Furthermore, with the cut-cell method, it is easier to adjust the recommended minimum cell volume for the DDPM model. A cell amount of 228,145 was used for calculations. In Figure 5-14, the cut-cell mesh including the inflation layers can be seen. The view shows the top of the riser with the exit to the cyclones [12,13,67].

5.2.4 Results

In the following chapters, the calculation results are presented. The overall calculation time (including auto-save, and time for creating reports and plots) was about one week for each case. The calculation time per cell, parcel and real time was about 0.188 ms.

Solid volume fraction

In Figure 5-15, the gas volume fraction is shown for different time steps. The view shows the riser bottom from z = 0 m to about a bed height of z = 2.4 m. For the qualitative analysis, case 3 was chosen. The pictures are showing the xy-symmetry plane. The left side of the picture is the azimuthal direction West. The overall observed time is about 0.5 seconds. Noticeable is the agglomeration of particles near the wall. These particle clusters are sliding down on the riser wall (indicated with blue arrow). The gas volume fraction in the symmetrical axis of the riser is very high. The particle volume fraction is less than 10%, so also a DPM model would be suitable (compare with chapter 3.2). At the lower part of the riser, ascending particle clusters are recognizable. During the upward movement, the dense clusters are breaking up, and the particles are diluted in the riser (indicated with blue circles).

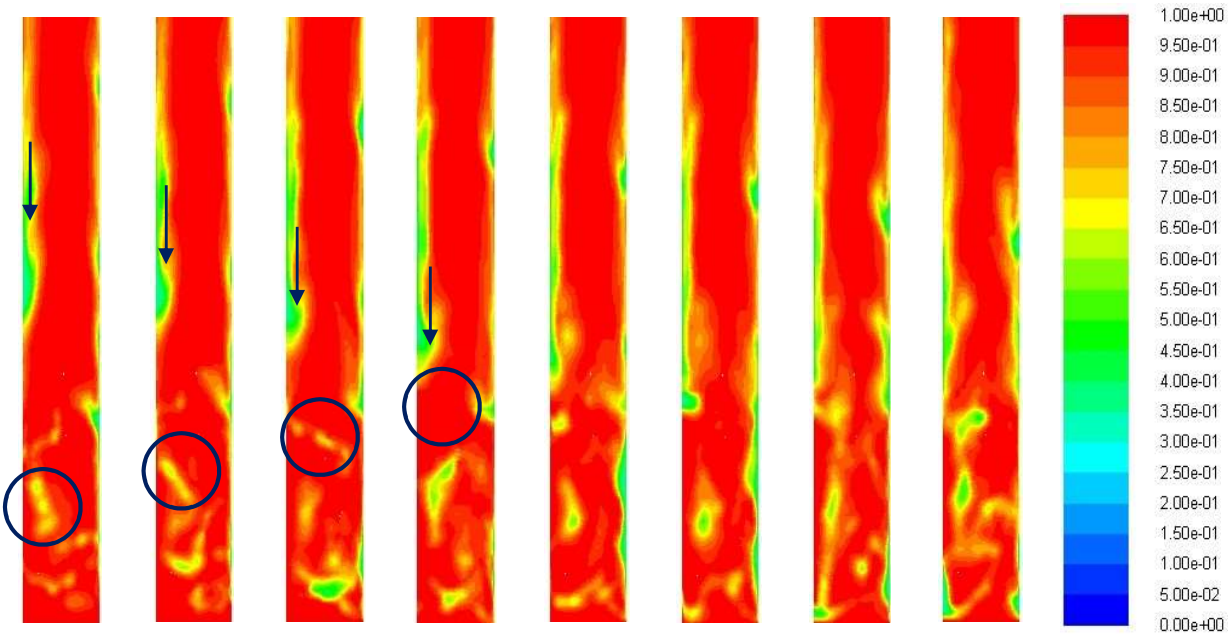

*Figure 5-15: NETL III Task 3, case 3: Contour plots of the **gas volume fraction (-)** at the riser bottom (z = 0 m – z = 2.4 m).*

Pressure gradient

In the following charts, the experimental pressure gradient is compared to the corresponding simulation results. The depicted experimental data points were already averaged by NETL from the actual measured data points considering the confidence interval. The pressure gradient for case 3 is shown in Figure 5-16. The deviation to the experiments is quite high. Especially in the lower part of the riser, the real pressure gradient was not reproduced, and the simulation results show a fluctuating behavior. For the upper part, the qualitative trend of the constant pressure gradient is well recreated. However, the prediction of the pressure gradient is far too low. In addition, the increase at the riser top was not reproduced.

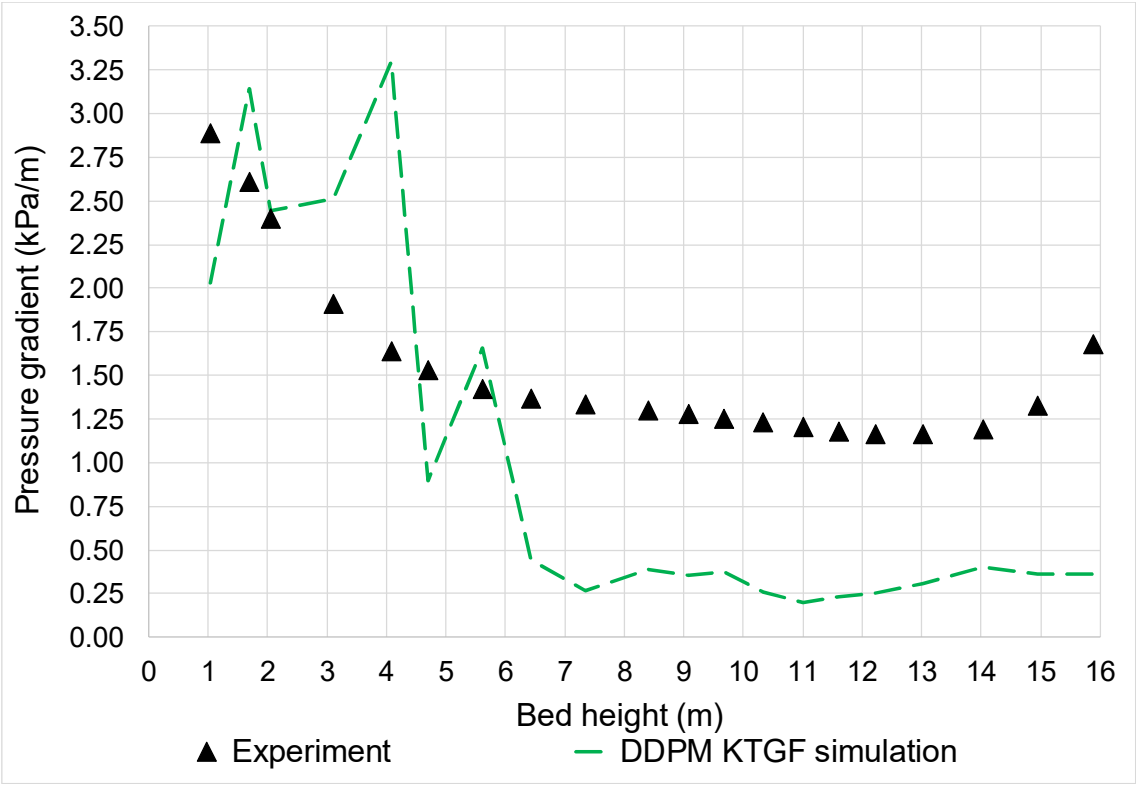

Figure 5-16: NETL III Task 3, case 3: Pressure gradient [83].

In Figure 5-17, the pressure gradient for case 4 is presented. The accuracy of the model was improving with increasing superficial gas velocity. Extreme fluctuations as in case 3 were not observed. However, the increase of the pressure gradient at the riser top cannot be reproduced. The pressure gradient between riser height z = 4 m and z = 9 m is over-predicted.

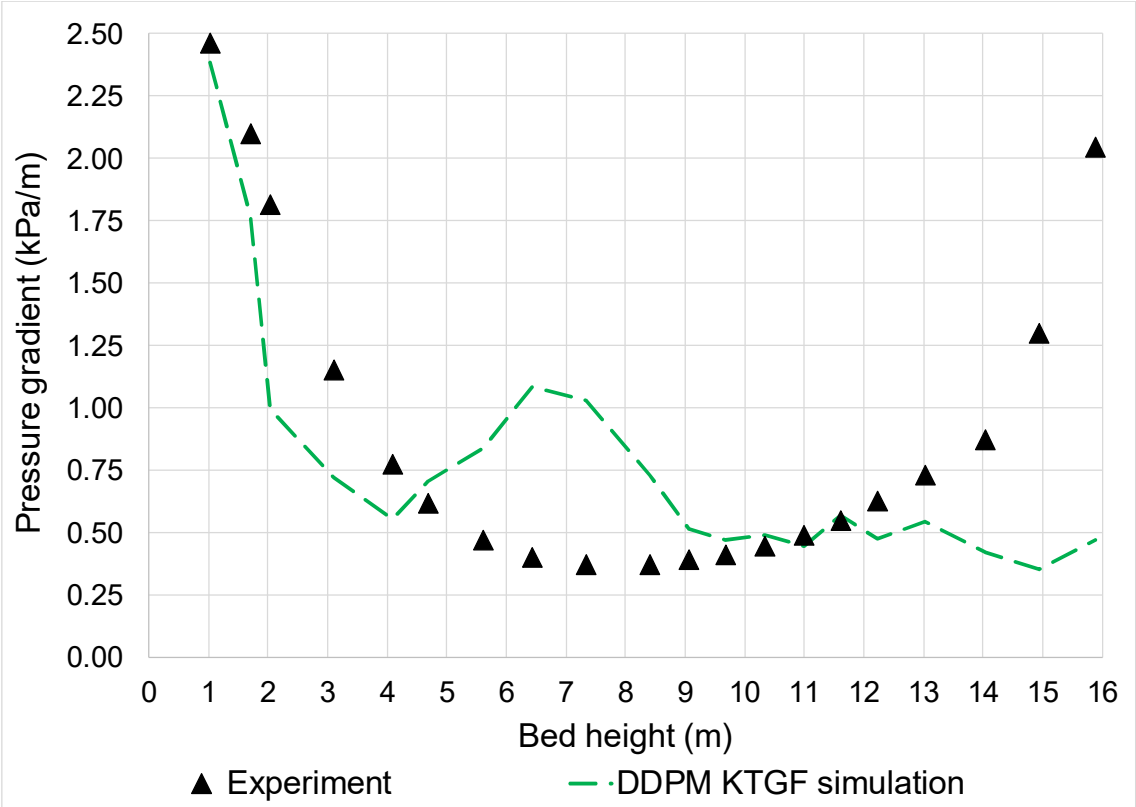

Figure 5-17: NETL III Task 3, case 4: Pressure gradient [83].

For case 5 (Figure 5-18), the increasing pressure gradient at the particle exit is captured. However, for case 3, unphysical pressure gradient predictions are occurring at the lower riser part. The pressure gradient results for case 5 were the best ones. As observed before, the pressure gradient prediction for higher gas velocity is getting better. Li et al. [61,87] also reported better predictions for PSD B and higher superficial gas velocity. This again indicates better performance of the KTGF model for superficial gas velocities much higher than the minimum fluidization velocity.

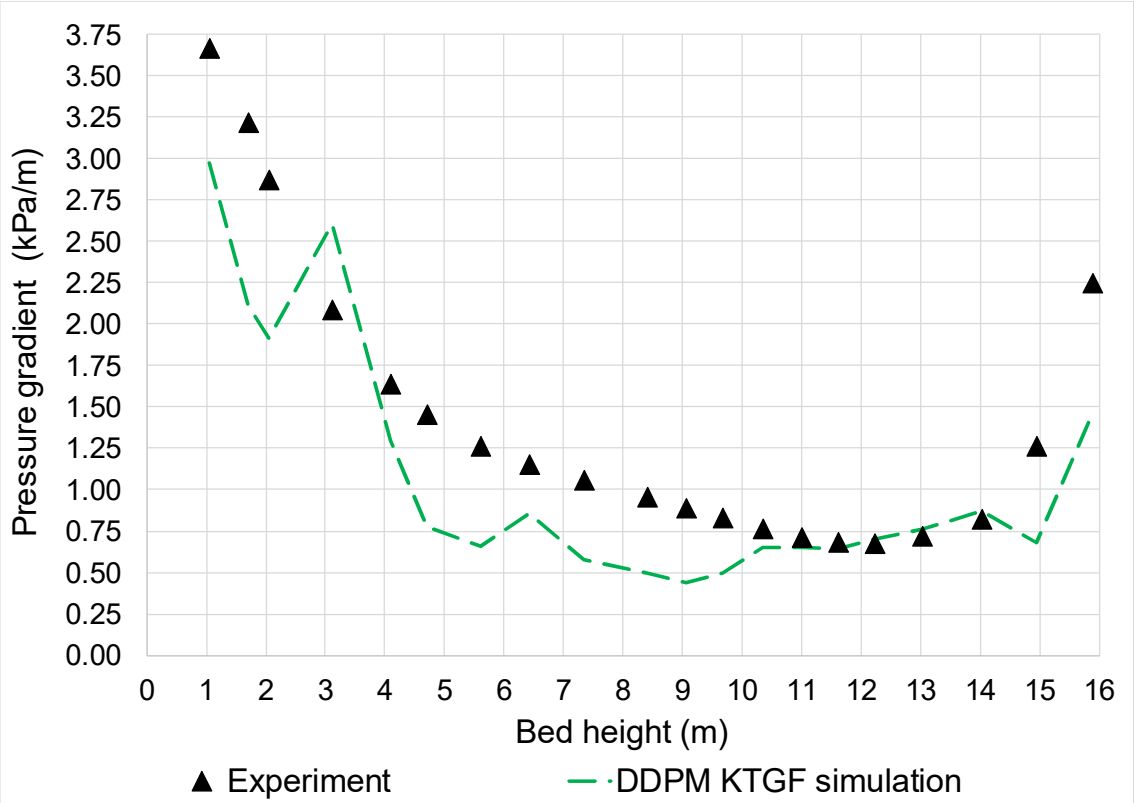

Figure 5-18: NETL III Task 3, case 5: Pressure gradient [83].

The pressure gradient prediction is not well captured for low superficial gas velocities. On the one hand, that is because of the simplified PSD. Instead of using a representation of all particle diameters, only the Sauter mean diameter was used for all particles. The investigations in chapter 5.1 showed that a more detailed resolution of the PSD can lead to better results. On the other hand, the boundary conditions to the adjacent CFB parts were set as constant values (outlet to cyclones and inlet at L-valve sparger). However, as presented in chapter 4.4.1, the characteristic values in fluidized beds are just statistically constant.

Vertical particle velocity

The following charts show the vertical particle velocity profile averaged over time. Measurements were done for three different bed heights (z = 6.23 m, z = 8.88 m and z = 13.33 m). The definitions of the azimuthal directions are explained in Figure 5-13. Noticeable is the trend of a left-shift of the velocity profile. Nearly all curves are shifted in East-direction. Therefore, the particle velocity is overpredicted for the region near the riser wall, which is opposite the standpipe. The velocities near the wall, on the standpipe side, are under-predicted. Li et al. [61,86,87] were not observing a shift of the velocity profile for case 3. However, for case 5 they also experienced a small displacement of the particle velocity profile. Their maximum particle velocity in the center of the bed was significantly over-predicted. A reason for the displacement of the velocity profile obtained in this work might be the simplification of CFB geometry. Instead of a full-loop model, just the riser itself was modeled. Therefore, the recirculation of the particles was only considered with a steady BC and a short inflow region. A more detailed modeling of the inlet and outlet configuration or a full model of the CFB might improve the predictions.

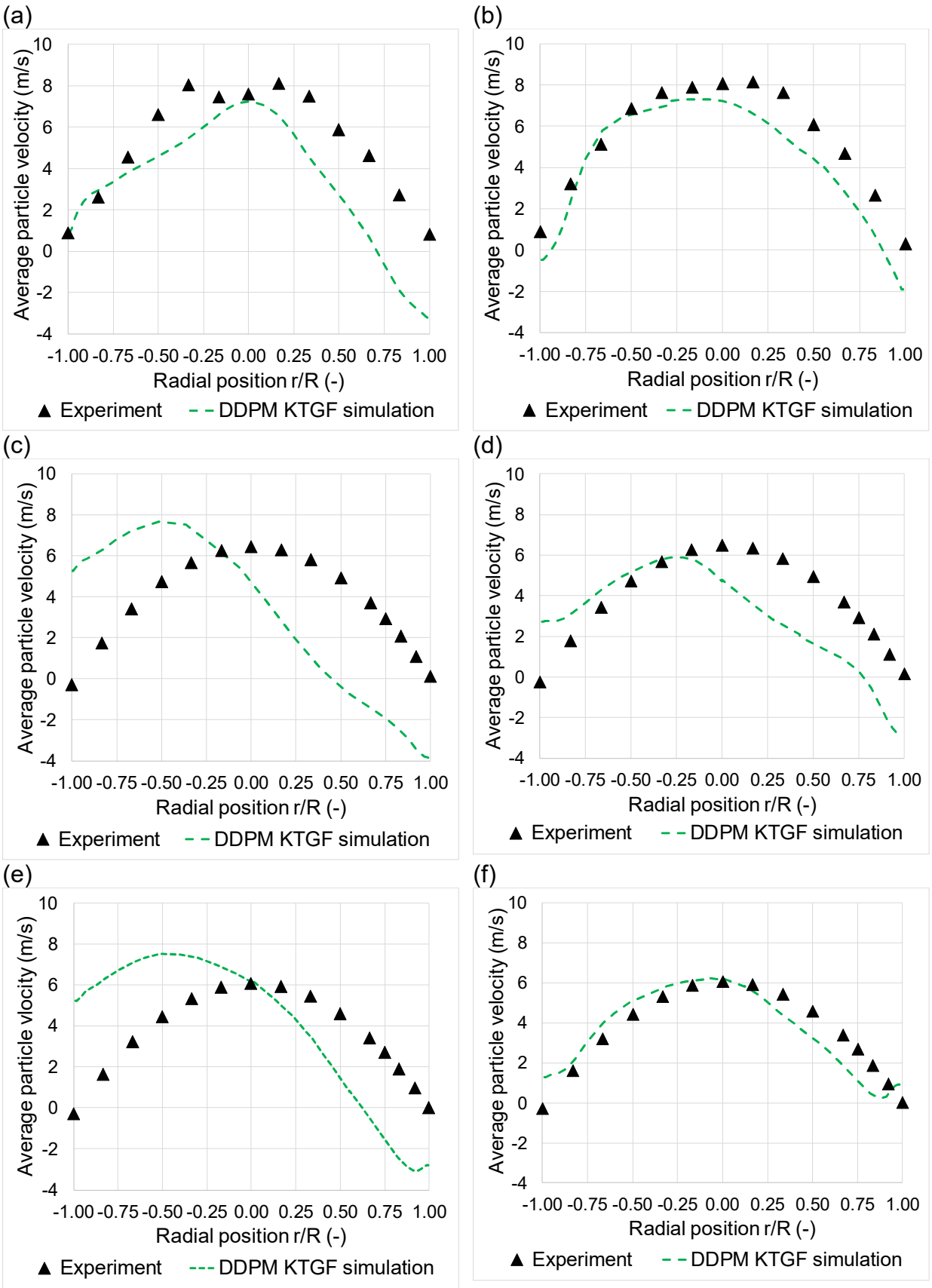

*Figure 5-19: NETL III Task 3, case 3: **Vertical particle velocity** profile [83].*
(a) height: 13.33 m, Azimuthal: E-W, (b) height: 13.33 m, Azimuthal: N-S,
(c) height: 8.88 m, Azimuthal: E-W, (d) height: 8.88 m, Azimuthal: N-S,
(e) height: 6.23 m, Azimuthal: SE-NW, (f) height: 6.23 m, Azimuthal: NE-SW.

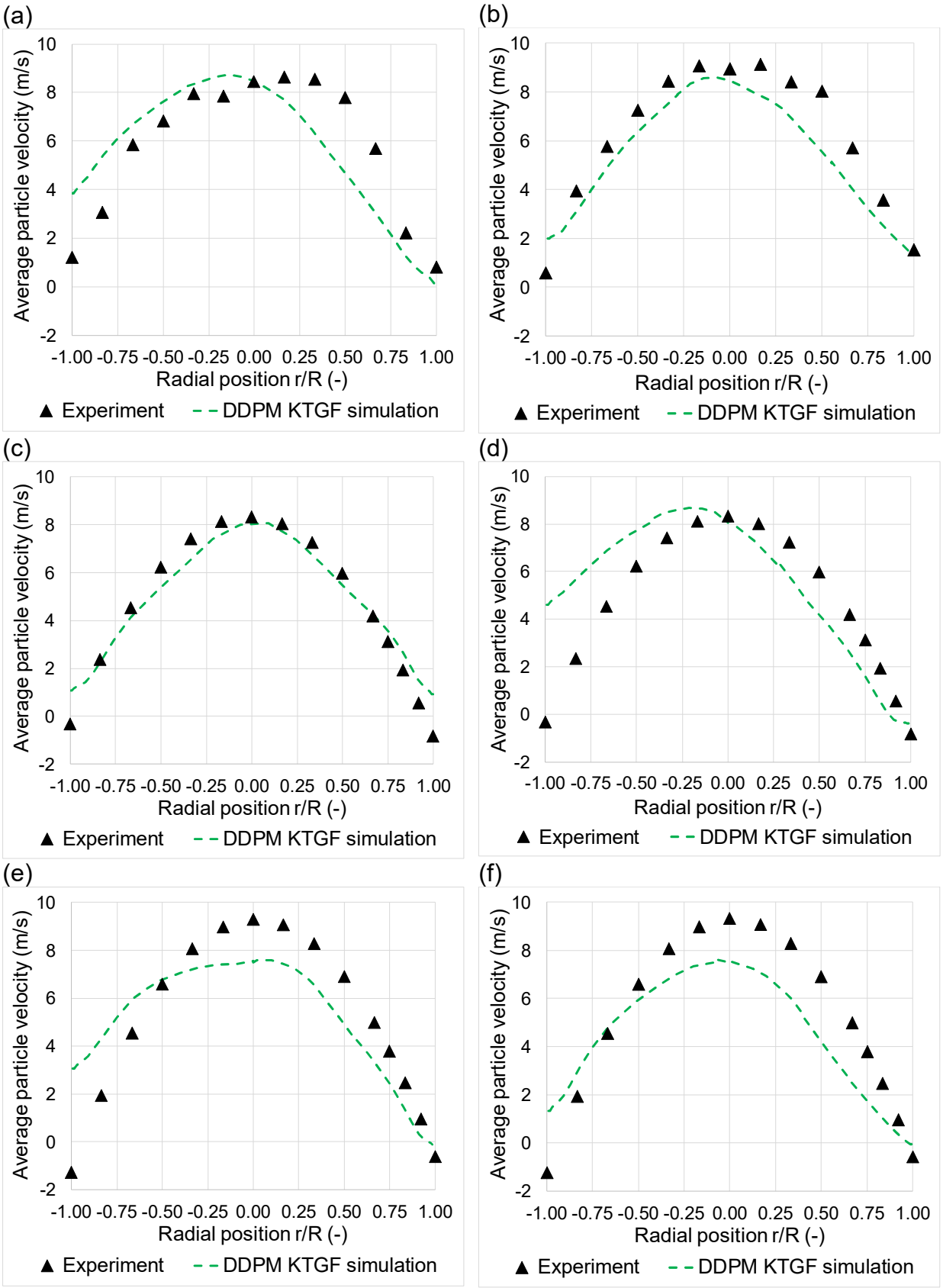

*Figure 5-20: NETL III Task 3, case 4: **Vertical particle velocity** profile [83].*
(a) height: 13.33 m, Azimuthal: E-W, (b) height: 13.33 m, Azimuthal: N-S,
(c) height: 8.88 m, Azimuthal: E-W, (d) height: 8.88 m, Azimuthal: N-S,
(e) height: 6.23 m, Azimuthal: SE-NW, (f) height: 6.23 m, Azimuthal: NE-SW.

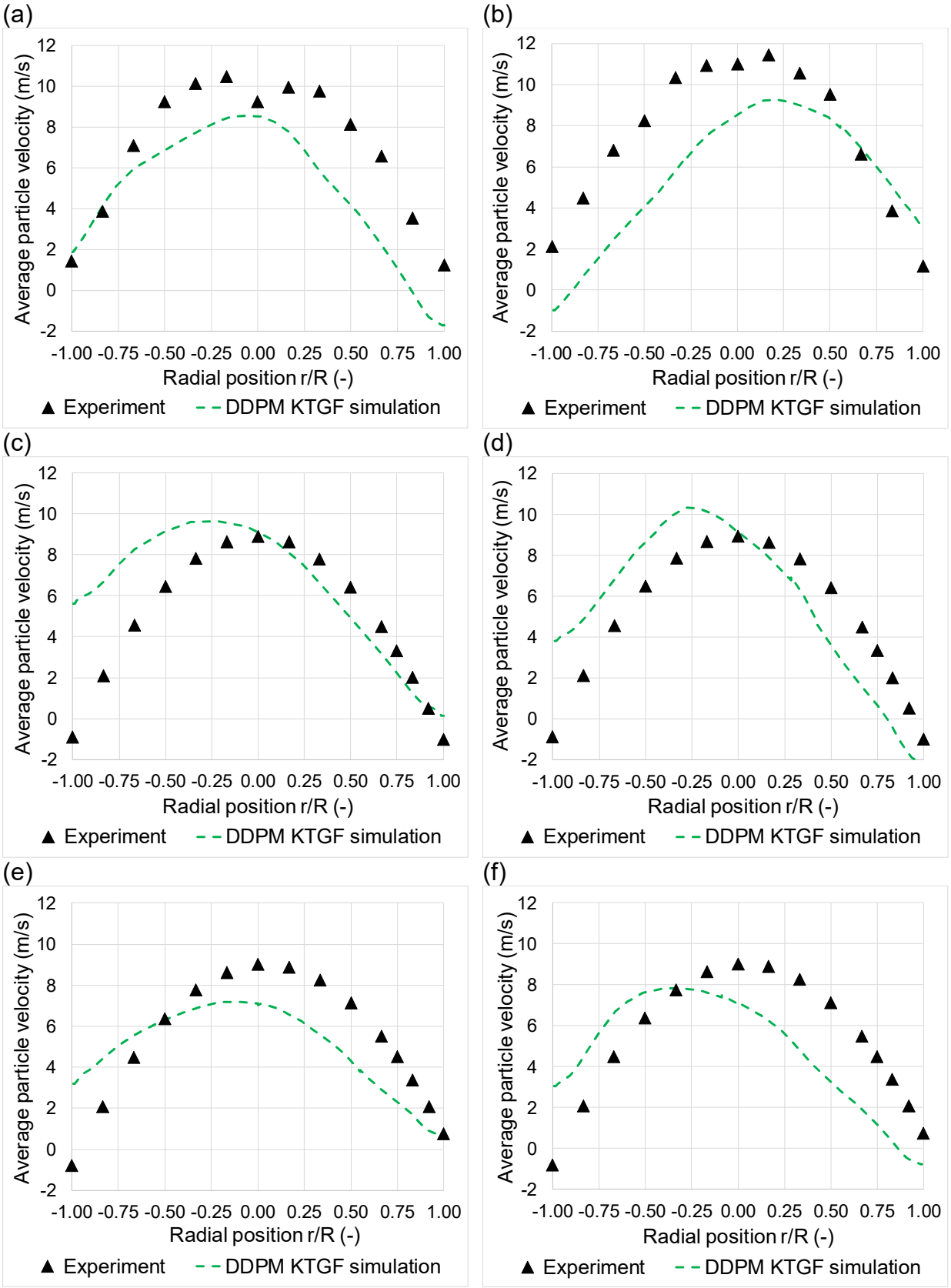

*Figure 5-21: NETL III Task 3, case 5: **Vertical particle velocity** profile [83].*
(a) height: 13.33 m, Azimuthal: E-W, (b) height: 13.33 m, Azimuthal: N-S,
(c) height: 8.88 m, Azimuthal: E-W, (d) height: 8.88 m, Azimuthal: N-S,
(e) height: 6.23 m, Azimuthal: SE-NW, (f) height: 6.23 m, Azimuthal: NE-SW.

As stated in chapter 4.2.2, the particle down-flow near the wall was not reproduced for the NETL I challenge (DDPM-KTGF). For NETL III Task 3 the particle flow at the near wall region is captured well for the most cases. A reason for that is the higher superficial gas velocity, which leads to a more dilute bed. As discussed in the previous chapters, the KTGF model works better for higher velocities. Additionally, two model modifications were done. On the one hand, a granular phase boundary condition at the wall (the ANSYS® Fluent built-in boundary condition by Johnson and Jackson [29] – see chapter 3.7) as recommended in chapter 4.5, was used. On the other hand, the use of inflation layers improved the capturing of the particle down-flow (applied as suggested by Ozarkar et al. [67]). According to Li et al. [61,86], the most important parameters for the CFB riser are the wall boundary conditions and the inflow boundary conditions. Especially careful choices of the specularity coefficient and a better resolution of the inlet and outlet configuration have the potential for further improvements.

5.3 Discussion NETL III

The calculation time is drastically increased, when simulating industrial-size fluidized beds in combination with a PSD. Calculations for the NETL I challenge lasted for several hours, whereas the NETL III challenges took a day or more. The high particle amount is the reason behind that. The DDPM-KTGF model is tracking the path of these particles. For lowering the time for the particle tracking, clusters of particles (parcels) are tracked instead of individual particles. In addition, it is a common strategy to model just parts of industrial size fluidized beds, in order to lower the total particle number.
Different approaches of the PSD models were tested. The simplest method is to assign a uniform particle diameter for all particles (Sauter mean diameter). ANSYS® Fluent also provides the possibility to define a Rosin-Rammler fit. Finally, a PSD model based on piecewise Sauter mean diameters was created (chapter 5.1.2). A disadvantage of the Rosin Rammler distribution is that it is smoothing non-regular PSD's (e.g., local peaks). As shown in Figure 5-5, the piecewise Sauter mean diameter PSD model is a better representation for local peaks, since a particle class can manually set into the peak. Therefore, the piecewise Sauter mean diameter yielded slightly better results (about 6% deviation to the experiments) than the Rosin Rammler distribution (about 7.5% deviation to the experiments) for the pressure drop. Simulations with a more detailed PSD (higher number of particle size classes) were yielding better pressure drop results (the average deviation was lowered from 7.3% to 4.15% for doubled number of particle size classes). However, the computational effort was increasing (about doubled calculation time). Simulations of NETL III Task 1 (chapter 5.1) showed that the DDPM-KTGF model was not able to reproduce the fluidization curve for the packed bed regime. However, above the minimum fluidization velocity, the pressure drop results fit well with the experimental data. Therefore, DDPM-KTGF should only be used for fluidization velocities well above U_{mf}. The more detailed PSD models were improving the results. However, the pressure drop was still over-predicted because the standard drag laws were yielding unphysical bed expansion behavior [68]. Additionally, an Euler Granular packed bed model, which is freezing the particle motion and therefore is not over-predicting the bed expansion, was tested. Hence, the proportional pressure drop increase in the fixed bed region was well reproduced.
For the NETL III challenges, a more detailed wall boundary condition for the granular phase was included (Johnson and Jackson [29]), in order to improve the particle velocity predictions near to the wall [84] (compared to the NETL I challenge). In addition, a finer mesh near the wall was created (by using inflation layers) for a better resolution of the particle flow next to the wall. These modifications were improving the particle flow prediction near the wall compared to the NETL I challenge. Also the prediction of the particle velocity profile was good.
However, the prediction of the bed expansion behavior (pressure drop) was not satisfactorily for all the investigated cases. In order to obtain better results with the DDPM-KTGF approach, alternative drag laws could be used or a more detailed PSD model. In literature, many alternative drag laws are suggested. For example, according to Ozarkar et al. [74], the drag law obtained by Milioli et al. [55] is better suitable for predicting the bed expansion in fluidized beds. Furthermore, the resolution of the PSD model can be increased in order to get a better representation of the PSD used in the experiments. Other reasons are the simplified inlet and outlet configurations. Therefore, a more careful choice of the boundaries (e.g., longer inlet and outlet pipes, finer mesh), or the use of a full-loop model could improve the results in these regions [61,68,86].

6 Conclusions and future work

In this thesis, the hydrodynamics of cold flow fluidized beds were investigated. Existing multiphase models and sub-models available in the commercial CFD code ANSYS® Fluent were validated and evaluated. For adjusting the model parameters (e.g., specularity coefficient, coefficient of restitution, injection settings) as well as for validating the models (pressure drop, particle velocity), experimental data provided by National Energy Technology Laboratory (NETL) was used. Simulations of the NETL challenge I and III were done to gain experience and to create guidelines for further projects on CFD modelling of fluidized beds. The research questions defined in chapter 1 are repeated and answered here:

Q1 Which multiphase models available in the commercial CFD code ANSYS® Fluent are suitable to simulate biomass fluidized beds?
Q2 How important are particle interactions and how can these interactions be modeled?
Q3 How can the influence of the particle size distributions (PSD) be included in the models?
Q4 Are the drag laws available in ANSYS® Fluent able to predict the fluidized bed behavior?
Q5 For which bed regimes, bed types and bed sizes are these models suitable?

Research questions **Q1** and **Q2**: Usually, in fluidized beds the interactions between particles cannot be neglected, because the particle volume fraction is too high (α_s > 0.1). In ANSYS® Fluent two basic modeling approaches for fluidized beds are available, which are considering particle interactions. First, one is the Euler Granular model. Occurring phases are considered as each other interpenetrating continua (Two-Fluid model). Therefore, the equations of motion as well as the continuity equation are defined for each phase separately. Interactions between particles (collisions) can be considered with the Kinetic Theory of Granular Flow (KTGF). The main idea of KTGF is to model the mechanical energy of the granular phase as velocity fluctuations around a mean particle velocity (averaging of particle collisions). The second possibility is the Dense Discrete Phase Model (DDPM), which is using an Euler-Lagrange approach. The primary phase (gas phase) is defined in an Eulerian framework (conservative equations for each cell). The particles are defined in an Eulerian framework and additionally are tracked in a Lagrangian framework (hybrid model) over several cells (Newton's 2nd law of motion). The particle velocity is obtained from the Lagrangian framework. Therefore, it is not necessary to calculate the conservative equations in the Eulerian framework for the solid phases. Interactions between particles are considered with KTGF or the Discrete Element Method (DEM). The DEM is a far more detailed approach, since it is resolving all individual particle collisions. Consequently, the DEM was superior to the other model combinations in predicting the particle velocities [23,32]. DDPM-DEM is also the numerically most demanding one. For complex flows, where the assumption of few different particle diameter sizes or a uniform particle diameter is adequate, the Euler Granular model is a competitive model. Calculations with Euler Granular-KTGF models took about 7.5h for NETL challenge I, which was about 1.4 times faster than the DDPM-KTGF approach (10.5h). For calculations of beds with a detailed particle size distribution (PSD), the DDPM constitutes an advantage. An additional particle diameter class is not requiring additional conservative equations. However, the DDPM-KTGF is sensitive to its parameters.

The best results were achieved with by the DDPM-DEM calculations. However, since the model is numerically too demanding, it is still rarely used for industrial-size fluidized beds. The DDPM-DEM calculation for a small-size FB needed already more than 2.5 times longer (26.5h) than the DDPM-KTGF approach. Therefore, the DDPM-KTGF model is the best compromise for industrial-size fluidized beds.

Research question **Q3**: The PSD has a significant influence on the simulation results. In this work, three PSD model approaches were tested (also see chapter 5.1.3). The most common assumption is an overall Sauter mean diameter. All particles are set to a uniform size. Another possibility to represent the PSD, is the Rosin Rammler fit. The Rosin Rammler fit is classifying the whole particle size distribution into equal diameter ranges. Because of its direct implementation into ANSYS® Fluent, the Rosin Rammler fit is fast and easy to set up. In addition, an approach with piecewise Sauter mean diameters for specific defined particle size classes was tested. The advantage is that the size classes are manually defined. Therefore, important size classes can be better taken into account [10]. A disadvantage of the Rosin Rammler distribution is that it is smoothing non-regular PSD's. The piecewise Sauter mean diameter PSD model is a better representation for local peaks. Therefore, the piecewise Sauter mean diameter yielded better results (about 6% deviation to the experiments) than the Rosin Rammler distribution (about 7.5% deviation to the experiments) for the pressure drop. Simulations with a more detailed PSD (10 instead of 5 size classes) were yielding better results for the pressure drop (the average deviation was lowered from 7.3% to 4.15%). However, the computational effort was increasing (about doubled calculation time). Summarized, the Rosin Rammler fit is an efficient approach for smooth and regular PSD. It is the best compromise between computation time and results. However, for irregular PSD's the piecewise Sauter mean diameter approach is the better choice. For industrial-size applications, the calculations should first be done with a uniform particle size, to keep the calculation time low. If needed (e.g., pressure drop deviation to experiments too high), a more detailed PSD model with several diameter size classes can be added afterwards.

Research question **Q4**: The drag laws derived by Wen-Yu [39], Gidaspow [25] and Syamlal O'Brien [26] have been tested. More details about the used drag laws are given in chapter 3.6. The overall best results were given by the drag law derived by Gidaspow (see chapter 4.5). The DEM calculation was best reproducing the bed behavior (including the bubble forming) – see chapter 4.4.3. However, the pressure drop was over-predicted for most cases. The main reason for this was the unphysical prediction of the bed expansion (especially for KTGF calculations in combination with a PSD – see chapter 5.3). Therefore, when using the KTGF model, it is important to validate the bed expansion. If necessary, a better particle interaction model (e.g., including of Johnson and Jackson boundary condition and alternative drag laws) and/or a more detailed resolution of the PSD improves the results. Other authors [36,57,68,88] were also reporting problems with the prediction of the bed expansion. For that reason, Ozarkar et al. [88] were testing alternative drag laws and were reporting excellent predictions of the bed expansion behavior with the drag law suggested by Milioli et al. [75].

Since the particle-gas flow behavior can be very different (dense or dilute flow, frictional or collisional dominated flow, particle type, PSD), no general recommendation can be given for research question **Q5**. For small-scale problems, where the particle amount is low, the DDPM-DEM approach is the best choice (chapter 4.4). DEM yields superior results due to the detailed resolving of all particle interactions. However, DEM is numerically very demanding, so DEM models are rarely used for large-scale applications or only with high-performance computing systems. DEM is mainly used in fundamental research, where it is also used as a benchmark model for the simpler approaches.

Industrial scale applications are best resolved with the DDPM-KTGF model, since PSD models are easy to include. Furthermore, the Lagrangian approach used in the DDPM provides many opportunities for future model extensions (e.g., single particle models for heat transfer and gasification). The Euler Granular model is inefficient for multiple diameters, because it needs an own set of conservative equation for each size class. Furthermore, reacting systems would require additional equations for the species transport for each particle size class. The DDPM model is the better choice for a detailed PSD (also see chapters 3.1, 3.3 and 5) – no additional conservative equations are needed. However, for FB's which operate with different particle volume fractions (e.g., CFB: dilute areas in riser and standpipe, dense areas at bed bottom and in the L-valve), the KTGF model is not easy to set up, because the relation between solids stress tensor and volume fraction is changing. Therefore, a KTGF model works well for a specific problem. However, it is not a very flexible approach (in the standard formulation). Furthermore, the KTGF approach had problems with the prediction of the particle flow next to the wall (chapter 4.2.2). However, an additional wall boundary condition for the solid phase (Johnson and Jackson [29], see chapter 3.7) is improving the prediction. The Johnson and Jackson approach is adding a heuristic friction by adding a boundary at which some particles collide and others slide [41]. In addition, the inclusion of inflation layers (for a better mesh resolution next to the wall) was significantly improving the particle flow prediction near the wall. Furthermore, DDPM-KTGF is failing for packed beds, the proportional increase of the pressure drop with increasing superficial gas velocity was not reproducible (see chapter 5.1). The KTGF model already predicted an expanded bed (more than 2.5%) for superficial gas velocities below U_{mf}, hence a constant pressure drop was predicted for the packed bed region. Therefore, DDPM-KTGF should only be used for fluidization velocities well above U_{mf} (which is usually the case for fluidized beds). In general, the results were improving with higher superficial gas velocities (more than two times the minimum fluidization velocity).

It was shown that the DDPM-DEM model was the best and most flexible approach (for models with parcel number equal to particle number). Results were already well fitting with the experiments after a rough estimation of its model parameters. However, the detailed resolution of the inter-particle interactions is still too costly for industrial applications (high particle number, non-spherical particles). The numerical less demanding DDPM-KTGF is highly sensitive to its model parameters. Crucial for the calculations are, in particular, the particle volume fraction, the resolution of the collisions and the boundary conditions at the walls. Therefore, validation of obtained KTGF results is mandatory. Nevertheless, DDPM-KTGF models with carefully selected settings were yielding competitive results for gas velocities higher than U_{mf}. The Euler Granular KTGF model is competitive when the assumption of few different particle size classes is sufficient for the calculation.

Based on the findings in this thesis, alternative drag models will be tested. Especially the promising drag law derived by Milioli et al. [75] will be investigated in more detail.

Notation

α	Volume fraction
γ	Damping coefficient
γ_{Θ_s}	Collisional dissipation of energy
γ°	Dimensionless shear rate
δ	Overlap
ε	Turbulent dissipation
η	Restitution coefficient
Θ	Granular temperature
λ_s	Bulk viscosity
μ	Viscosity
ϱ	Density
$\bar{\bar{\tau}}$	Solid stress tensor
τ_s	Relaxation time
ϕ_s	Sphericity
φ	Specularity coefficient
φ	Angle of internal friction
A	Area
Ar	Archimedes number
C_D	Drag coefficient
c	Drag function
d_{32}	Sauter mean diameter
d	Diameter
$\vec{e}_{ij}$	Unit direction vector
$\vec{F}$	Force
F_{drag}	Coefficient of proportionality
$\vec{f}$	Acceleration
g	Gravitational acceleration
$g_{0,ss}$	Radial distribution function
$\bar{\bar{I}}$	Unit tensor
K	Spring-dashpot coefficient
K_{sg}	Momentum exchange coefficient
k	Turbulent kinetic energy
m	Mass
p	Pressure
p_s	Solids pressure
Re	Reynolds number
S_{mom}	Source term for two-way coupling
t	Temperature
Δt	Time step size
U_{mf}	Minimum fluidization velocity
U_t	Terminal velocity
V	Volume
v	Velocity
${v_s}'$	Velocity fluctuations
Y_d	Reversed cumulative mass fraction

Abbreviations

BC	Boundary condition
BFB	Bubbling fluidized bed
BRISK2	Biofuel Research Infrastructure for Sharing Knowledge
calc.	Calculation
CFB	Circulating fluidized bed
CFD	Computational Fluid Dynamics
CFL	Courant-Friedrichs-Lewy condition
const.	constant
CPU	Central processing unit
D	Bed depth
DDPM	Dense Discrete Phase Model
DEM	Discrete Element Method
DOE	Department of Energy
DP	Difference pressure, pressure drop
DPM	Discrete Phase Model
DFB	Dual fluidized bed
E	East
EMMS	Energy minimization multi-scale
EDC	Eddy dissipation concept model
FB	Fluidized bed
FCC	Fluid catalytic cracking
GT	Granular temperature
GPU	Graphics processing unit
H	Bed height
HsPIV	High-speed Particle Image Velocimetry
IWT	Institute of Thermal Engineering
KTGF	Kinetic Theory of Granular Flow
LES	Large eddy simulation
MP-PIC	Multiphase particle-in-cell method
N	North
NETL	National Energy Technology Laboratory
PSD	Particle size distribution
PSRI	Particulate Solids Research Inc.
Q	Research question
RNG	Re-Normalization Group
S	South
SI	International System of Units
sim.	Simulation
SLPM	Standard liter per minute
SSCP	Small-scale problem
TFM	Two-Fluid Model
UDF	User-defined function
W	Bed width
W	West

List of Figures

List of Tables

References

[1] D. Kunii, O. Levenspiel, Fluidization Engineering, 2nd ed., Elsevier, Amsterdam, Heidelberg, Butterworth-Heinemann, 2012.
[2] Hofbauer Hermann, Wirbelschichttechnik: Unterlagen zur Vorlesung 159.220, 6th ed., Technische Universität Wien, 2013.
[3] Stephan Kraft, Investigation of particle mixing in dual fluidized bed gasification systems by means of cold flow modelling and computational methods. Dissertation, TU Vienna, 2017.
[4] M. Kaltschmitt, H. Hartmann, H. Hofbauer (Eds.), Energie aus Biomasse: Grundlagen, Techniken und Verfahren, 3rd ed., Springer Vieweg, Berlin, 2016.
[5] D. Geldart, Types of gas fluidization, Powder Technology 7 (1973) 285–292. https://doi.org/10.1016/0032-5910(73)80037-3.
[6] W.-c. Yang, Handbook of fluidization and fluid-particle systems, Marcel Dekker, New York, 2003.
[7] Malvern Instruments Limited, A basic guide to particle characterization, 2015. https://www.cif.iastate.edu/sites/default/files/uploads/Other_Inst/Particle%20Size/Particle%20Characterization%20Guide.pdf (accessed 2 December 2018).
[8] F. Kirnbauer, H. Hofbauer, Investigations on Bed Material Changes in a Dual Fluidized Bed Steam Gasification Plant in Güssing, Austria, Energy Fuels 25 (2011) 3793–3798. https://doi.org/10.1021/ef200746c.
[9] M. Sommerfeld, Berend van Wachem, Rene Oliemans (Eds.), Best practice guidelines for computational fluid dynamics of dispersed multiphase flows, 1st ed., ERCOFTAC, [S.l.], 2008.
[10] ANSYS Inc., ANSYS® Fluent Theory Guide, 18th ed., 2017.
[11] Martin Sommerfeld, Review of Numerical Methods for Multiphase Flow, 2014. http://www.prague-sum.com/download/2014/Sommerfeld_Lecture1.pdf (accessed 22 October 2018).
[12] ANSYS Inc., Multiphase Modeling using ANSYS Fluent, ANSYS Inc., 2015.
[13] ANSYS Inc., ANSYS® Fluent User's Guide, 18th ed., 2017.
[14] M. Ishii, T. Hibiki, Thermo-Fluid Dynamics of Two-Phase Flow, Springer New York, New York, NY, 2011.
[15] M.B. Boris Popoff, A Lagrangian Approach to Dense Particulate Flows, 6th International Conference on Multiphase Flow - ICMF (2007, Leipzig) 1–11.
[16] Timo Niemi, Particle Size Distribution in CFD Simulation of Gas-Particle Flows. Master Thesis, Espoo, 2012.
[17] ANSYS Inc., ANSYS® Fluent Tutorial Guide, 18th ed., 2017.
[18] S.Cloete, S. Johansen, M. Braun, B. Popoff, S. Amini, Evaluation of a Lagrangian Discrete Phase Modeling Approach for Resolving Cluster Formation in CFB Risers, 7th International Conference on Multiphase Flow - ICMF (2010, Tampa) 1–8.
[19] S.A. Schalk Cloete, The dense discrete phase model for simulation of bubbling fluidized beds: Validation and verification, ICMF-2016, 9th International Conference on Multiphase Flow (2016, Firenze).
[20] P. G. Saffman, The Lift on a Small Sphere in a Slow Shear Flow, J.Fluid Mech (1965) 385–400.
[21] D.A. Drew, R.T. Lahey, The virtual mass and lift force on a sphere in rotating and straining inviscid flow, International Journal of Multiphase Flow 13 (1987) 113–121. https://doi.org/10.1016/0301-9322(87)90011-5.

[22] H. Ounis, G. Ahmadi, J.B. McLaughlin, Brownian diffusion of submicrometer particles in the viscous sublayer, Journal of Colloid and Interface Science 143 (1991) 266–277. https://doi.org/10.1016/0021-9797(91)90458-K.
[23] G.D. Ding Jianmin, A Bubbling Fluidization Model Using Kinetic Theory of Granular Flow, AIChE Journal 36 (1990) 523–538.
[24] Sébastien Dartevelle, Numerical and granulometric approaches to geophysical granular flows. Dissertation, Michigan, 2003.
[25] Gidaspow Dimitri, Bezburuah Rukmini, Ding Jianmin, Hydrodynamics of Circulating Fluidized Beds: Kinetic Theory Approach, 7th international conference on fluidization (1992, Gold Coast).
[26] T.O.'B. Madhava Syamlal, Computer simulation of bubbles in fluidized beds, Fluidization and Fluid Particle Systems: Fundamentals and Applications AIChE Symposium Series 270 (1989) 22–31.
[27] S. Pannala, M. Syamlal, T.J. O'Brien (Eds.), Computational gas-solids flows and reacting systems: Theory, methods and practice. James W. Dufty; Aparna Baskaran, 1st ed., IGI Global, Hershey, PA, United States, 2011.
[28] C.K.K. Lun, S.B. Savage, D.J. Jeffrey, N. Chepurniy, Kinetic theories for granular flow: inelastic particles in Couette flow and slightly inelastic particles in a general flowfield, J. Fluid Mech. 140 (1984) 223. https://doi.org/10.1017/S0022112084000586.
[29] P.C. Johnson, R. Jackson, Frictional–collisional constitutive relations for granular materials, with application to plane shearing, Journal of Fluid Mechanics 176 (1987) 67–93. https://doi.org/10.1017/S0022112087000570.
[30] D.G. Schaeffer, Instability in the evolution equations describing incompressible granular flow, Journal of Differential Equations 66 (1987) 19–50. https://doi.org/10.1016/0022-0396(87)90038-6.
[31] M. Syamlal, A review of granular stress constitutive relations, EG and G Washington Analytical Services Center, Inc. 1-26.
[32] M. Syamlal, W. Rogers, T.J. O`Brien, MFIX documentation theory guide, 1993.
[33] P. A. Cundall, O. D. L. Strack, A Discrete Numerical Model for Granular Assemblies, Geotechnique 29 (1979) 47–65.
[34] Y. Tsuji, T. Kawaguchi, T. Tanaka, Discrete particle simulation of two-dimensional fluidized bed, Powder Technology 77 (1993) 79–87. https://doi.org/10.1016/0032-5910(93)85010-7.
[35] H.A. Navarro, de Souza Braun, Meire P., Determination of the normal spring stiffness coefficient in the linear spring–dashpot contact model of discrete element method, Powder Technology 246 (2013) 707–722. https://doi.org/10.1016/j.powtec.2013.05.049.
[36] N.V. Koralkar, M. Bose, Performance of drag models for simulation of fluidized beds with Geldart D particles, Advanced Powder Technology 27 (2016) 2377–2398. https://doi.org/10.1016/j.apt.2016.11.008.
[37] Dr. Chang-Yu Wu, Qi Zhang, Ying Li, Randy Switt, Sameer Matta, Newton's Resistance Law and Stokes's Law, 2018. https://aerosol.ees.ufl.edu/aerosol_trans/section03_c.html (accessed 28 November 2018).
[38] Sabri Ergun, Fluid flow through packed columns, Chemical Engineering Progress 48 (1952) 89–94.
[39] Wen, C.Y. and Yu, Y.H., Mechanics of Fluidization, The Chemical Engineering Progress Symposium Series 62 (1966) 100–111.
[40] J.M. DallaValle, Micromeritics: The Technology of Fine Particles, Pitman Pub. Corp, New York, 1943.

[41] T. Li, S. Benyahia, Revisiting Johnson and Jackson boundary conditions for granular flows, AIChE J. 58 (2012) 2058–2068. https://doi.org/10.1002/aic.12728.
[42] Y. Zhao, T. Ding, L. Zhu, Y. Zhong, A Specularity Coefficient Model and Its Application to Dense Particulate Flow Simulations, Ind. Eng. Chem. Res. 55 (2016) 1439–1448. https://doi.org/10.1021/acs.iecr.5b03792.
[43] H. Zhong, X. Lan, J. Gao, Y. Zheng, Z. Zhang, The difference between specularity coefficient of 1 and no-slip solid phase wall boundary conditions in CFD simulation of gas–solid fluidized beds, Powder Technology 286 (2015) 740–743. https://doi.org/10.1016/j.powtec.2015.08.055.
[44] R. Panday, L.J. Shadle, M. Shahnam, R. Cocco, A. Issangya, J.S. Spenik, J.C. Ludlow, B. Gopalan, F. Shaffer, M. Syamlal, C. Guenther, S.R. Karri, T. Knowlton, Challenge problem: 1. Model validation of circulating fluidized beds, Powder Technology 258 (2014) 370–391. https://doi.org/10.1016/j.powtec.2014.02.010.
[45] B. Gopalan, M. Shahnam, R. Panday, J. Tucker, F. Shaffer, L. Shadle, J. Mei, W. Rogers, C. Guenther, M. Syamlal, Measurements of pressure drop and particle velocity in a pseudo 2-D rectangular bed with Geldart Group D particles, Powder Technology 291 (2016) 299–310. https://doi.org/10.1016/j.powtec.2015.12.040.
[46] Balaji Gopalan, SSCP-I Brochure, 2013. https://mfix.netl.doe.gov/experimentation/challenge-problems/ (accessed 27 March 2018).
[47] Balaji Gopalan, Small Scale Problem Description, 2013. https://mfix.netl.doe.gov/experimentation/challenge-problems/ (accessed 27 March 2018).
[48] B. Gopalan, F. Shaffer, A new method for decomposition of high speed particle image velocimetry data, Powder Technology 220 (2012) 164–171. https://doi.org/10.1016/j.powtec.2011.09.001.
[49] B. Gopalan, F. Shaffer, Higher order statistical analysis of Eulerian particle velocity data in CFB risers as measured with high speed particle imaging, Powder Technology 242 (2013) 13–26. https://doi.org/10.1016/j.powtec.2013.01.046.
[50] J. Jung, D. Gidaspow, I.K. Gamwo, Measurement of Two Kinds of Granular Temperatures, Stresses, and Dispersion in Bubbling Beds, Ind. Eng. Chem. Res. 44 (2005) 1329–1341. https://doi.org/10.1021/ie0496838.
[51] J. Jung, D. Gidaspow, I.K. Gamwo, Bubble computation, granular temperatures, and Reynolds stresses, Chemical Engineering Communications 193 (2006) 946–975. https://doi.org/10.1080/00986440500351982.
[52] NETL, Frequently Asked Questions NETL SSCP I, 2013. https://mfix.netl.doe.gov/experimentation/challenge-problems/ (accessed 27 March 2018).
[53] S. Cloete, S.T. Johansen, S. Amini, Grid independence behaviour of fluidized bed reactor simulations using the Two Fluid Model: Effect of particle size, Powder Technology 269 (2015) 153–165. https://doi.org/10.1016/j.powtec.2014.08.055.
[54] R. Courant, K. Friedrichs, H. Lewy, ber die partiellen Differenzengleichungen der mathematischen Physik, Math. Ann. 100 (1928) 32–74. https://doi.org/10.1007/BF01448839.
[55] W. Sutherland, The viscosity of gases and molecular force, The London, Edinburgh, and Dublin Philosophical Magazine and Journal of Science 36 (1893) 507–531. https://doi.org/10.1080/14786449308620508.
[56] Antonio Soria Verdugo, Motion of objects immersed in a bubbling fluidized bed. Dissertation, Madrid, 2010.

[57] V. Agrawal, Y. Shinde, M.T. Shah, R.P. Utikar, V.K. Pareek, J.B. Joshi, Effect of drag models on CFD–DEM predictions of bubbling fluidized beds with Geldart D particles, Advanced Powder Technology 29 (2018) 2658–2669. https://doi.org/10.1016/j.apt.2018.07.014.
[58] M. Lungu, H. Wang, J. Wang, Y. Yang, F. Chen, Two-Fluid Model Simulations of the National Energy Technology Laboratory Bubbling Fluidized Bed Challenge Problem, Ind. Eng. Chem. Res. 55 (2016) 5063–5077. https://doi.org/10.1021/acs.iecr.5b04511.
[59] H.A. Elghannay, D.K. Tafti, DEM Predictions of NETL Small Scale Challenge Problem, in: Proceedings of the ASME Fluids Engineering Division summer meeting 2014, Chicago, Illinois, USA, American Society of Mechanical Engineers, New York, N.Y., 2014, V01CT23A001.
[60] O.O. Ayeni, C.L. Wu, K. Nandakumar, J.B. Joshi, Development and validation of a new drag law using mechanical energy balance approach for DEM–CFD simulation of gas–solid fluidized bed, Chemical Engineering Journal 302 (2016) 395–405. https://doi.org/10.1016/j.cej.2016.05.056.
[61] T. Li, J.-F. Dietiker, M. Shahnam, MFIX simulation of NETL/PSRI challenge problem of circulating fluidized bed, Chemical Engineering Science 84 (2012) 746–760. https://doi.org/10.1016/j.ces.2012.09.024.
[62] B. Basara, S. Jakirlic, A new hybrid turbulence modelling strategy for industrial CFD, Int. J. Numer. Meth. Fluids 42 (2003) 89–116. https://doi.org/10.1002/fld.492.
[63] J. Fröhlich, D. von Terzi, Hybrid LES/RANS methods for the simulation of turbulent flows, Progress in Aerospace Sciences 44 (2008) 349–377. https://doi.org/10.1016/j.paerosci.2008.05.001.
[64] A. Sentürk, Pipe Flow. http://web.iku.edu.tr/~asenturk/Pipe%20I.pdf (accessed 7 December 2018).
[65] Mohit P. Tandon, Aditya U. Karnik, Simulation of rectangular fluidized bed with geldart D particles, International Conference on CFD in Oil (2014, Trondheim).
[66] S. Cloete, S.T. Johansen, S. Amini, Performance evaluation of a complete Lagrangian KTGF approach for dilute granular flow modelling, Powder Technology 226 (2012) 43–52. https://doi.org/10.1016/j.powtec.2012.04.010.
[67] Shailesh Ozarkar, Tingwen Li, Mehrdad Shahnam, Sankaran Sundaresan, Effects of grid topologies and resolution of boundary layer on gas-particle flow predictions in circulating fluidized bed riser, AIChE Annual Meeting (2014).
[68] S.S. Ozarkar, X. Yan, S. Wang, C.C. Milioli, F.E. Milioli, S. Sundaresan, Validation of filtered two-fluid models for gas–particle flows against experimental data from bubbling fluidized bed, Powder Technology 284 (2015) 159–169. https://doi.org/10.1016/j.powtec.2015.06.028.
[69] Y. Igci, S. Sundaresan, Constitutive Models for Filtered Two-Fluid Models of Fluidized Gas–Particle Flows, Ind. Eng. Chem. Res. 50 (2011) 13190–13201. https://doi.org/10.1021/ie200190q.
[70] R.J. Hill, D.L. Koch, A.J.C. LADD, Moderate-Reynolds-number flows in ordered and random arrays of spheres, J. Fluid Mech. 448 (2001). https://doi.org/10.1017/S0022112001005936.
[71] R.J. Hill, D.L. Koch, A.J.C. LADD, The first effects of fluid inertia on flows in ordered and random arrays of spheres, J. Fluid Mech. 448 (2001) 213–241. https://doi.org/10.1017/S0022112001005948.
[72] R. Beetstra, M.A. van der Hoef, J.A.M. Kuipers, Drag force of intermediate Reynolds number flow past mono- and bidisperse arrays of spheres, AIChE J. 53 (2007) 489–501. https://doi.org/10.1002/aic.11065.

[73] L.W. Rong, K.J. Dong, A.B. Yu, Lattice-Boltzmann simulation of fluid flow through packed beds of spheres: Effect of particle size distribution, Chemical Engineering Science 116 (2014) 508–523. https://doi.org/10.1016/j.ces.2014.05.025.
[74] H. Arastoopour, P. Pakdel, M. Adewumi, Hydrodynamic analysis of dilute gas—solids flow in a vertical pipe, Powder Technology 62 (1990) 163–170. https://doi.org/10.1016/0032-5910(90)80080-I.
[75] C.C. Milioli, F.E. Milioli, W. Holloway, K. Agrawal, S. Sundaresan, Filtered two-fluid models of fluidized gas-particle flows: New constitutive relations, AIChE J. 59 (2013) 3265–3275. https://doi.org/10.1002/aic.14130.
[76] NVIDIA Corporation, Accelerating ANSYS Fluent 15.0 using NVIDIA GPUS, 2014 (accessed 28 September 2018).
[77] V. Sellappan, Accelerating ANSYS Fluent Simulations with NVIDIA GPUs, ANSYS Advantage IX (2015) 51–53.
[78] Larry Shadle, Mehrdad Shahnam, Ray Cocco, Allan Issangya, Chris Guenther, Madhava Syamlal, James Spenik, J. Chris Ludlow, Frank Shaffer, Rupen Panday, Balaji Gopalan, and Rajiv Dastane, Challenge Problem III: CFB X Workshop, 2011. https://mfix.netl.doe.gov/challenge-problem-iii-2010/ (accessed 9 October 2018).
[79] Rupen Panday, Powder Tech Note, 2010. https://mfix.netl.doe.gov/challenge-problem-iii-2010/ (accessed 9 October 2018).
[80] R.C. Larry Shadle, PSRI NETL Challenge Problem Brochure, 2010. https://mfix.netl.doe.gov/challenge-problem-iii-2010/ (accessed 9 October 2018).
[81] Rupen Panday, Questions and Answers, 2010. https://mfix.netl.doe.gov/challenge-problem-iii-2010/ (accessed 9 October 2018).
[82] Rupen Panday, BFB Challenge Problem, 2010. https://mfix.netl.doe.gov/challenge-problem-iii-2010/ (accessed 9 October 2018).
[83] Rupen Panday, CFB Experimental Data, 2010. https://mfix.netl.doe.gov/challenge-problem-iii-2010/ (accessed 9 October 2018).
[84] Jungkee Jang and Hamid Arastoopour, CFD Simulation of Different-Scaled Bubbling Fluidized Beds, The 14th International Conference on Fluidization (2013, Leeuwenhorst).
[85] R. Panday, L.J. Shadle, M. Shahnam, R. Cocco, A. Issangya, J.S. Spenik, J.C. Ludlow, B. Gopalan, F. Shaffer, M. Syamlal, C. Guenther, S.R. Karri, T. Knowlton, Challenge problem: 1. Model validation of circulating fluidized beds, Powder Technology 258 (2014) 370–391. https://doi.org/10.1016/j.powtec.2014.02.010.
[86] T. Li, A. Gel, S. Pannala, M. Shahnam, M. Syamlal, CFD simulations of circulating fluidized bed risers, part I: Grid study, Powder Technology 254 (2014) 170–180. https://doi.org/10.1016/j.powtec.2014.01.021.
[87] T. Li, S. Pannala, M. Shahnam, CFD simulations of circulating fluidized bed risers, part II, evaluation of differences between 2D and 3D simulations, Powder Technology 254 (2014) 115–124. https://doi.org/10.1016/j.powtec.2014.01.022.
[88] S.S. Ozarkar, X. Yan, S. Wang, C.C. Milioli, F.E. Milioli, S. Sundaresan, Validation of filtered two-fluid models for gas-particle flows against experimental data from bubbling fluidized bed, 2016, p. 20.